

# ***PFLOTRAN Development FY2022***

## **Spent Fuel and Waste Disposition**

***Prepared for  
U.S. Department of Energy  
Spent Fuel & Waste Science and Technology***

***M. Nole, G.D. Beskardes, D. Fukuyama,  
R.C. Leone, P. Mariner, H.D. Park, M. Paul,  
A. Salazar, G.E. Hammond\*, P.C. Lichtner\*\****

***Sandia National Laboratories  
\*Pacific Northwest National Laboratory***

***\*\*OFM Research***

***August 01, 2022  
M3SF-22SN010304112  
SAND2022-10526 R***



#### **DISCLAIMER**

This information was prepared as an account of work sponsored by an agency of the U.S. Government. Neither the U.S. Government nor any agency thereof, nor any of their employees, makes any warranty, expressed or implied, or assumes any legal liability or responsibility for the accuracy, completeness, or usefulness, of any information, apparatus, product, or process disclosed, or represents that its use would not infringe privately owned rights. References herein to any specific commercial product, process, or service by trade name, trade mark, manufacturer, or otherwise, does not necessarily constitute or imply its endorsement, recommendation, or favoring by the U.S. Government or any agency thereof. The views and opinions of authors expressed herein do not necessarily state or reflect those of the U.S. Government or any agency thereof.

#### **DISCLAIMER**

This is a technical report that does not take into account contractual limitations or obligations under the Standard Contract for Disposal of Spent Nuclear Fuel and/or High-Level Radioactive Waste (Standard Contract) (10 CFR Part 961). For example, under the provisions of the Standard Contract, spent nuclear fuel in multi-assembly canisters is not an acceptable waste form, absent a mutually agreed to contract amendment.

To the extent discussions or recommendations in this report conflict with the provisions of the Standard Contract, the Standard Contract governs the obligations of the parties, and this report in no manner supersedes, overrides, or amends the Standard Contract.

This report reflects technical work which could support future decision making by DOE. No inferences should be drawn from this report regarding future actions by DOE, which are limited both by the terms of the Standard Contract and Congressional appropriations for the Department to fulfill its obligations under the Nuclear Waste Policy Act including licensing and construction of a spent nuclear fuel repository.

Sandia National Laboratories is a multi-mission laboratory managed and operated by National Technology & Engineering Solutions of Sandia, LLC., a wholly owned subsidiary of Honeywell International, Inc., for the U.S. Department of Energy's National Nuclear Security Administration under contract DE-NA0003525.



**U.S. DEPARTMENT OF  
ENERGY**



**Sandia National Laboratories**

APPENDIX E  
NFCSC DOCUMENT COVER SHEET<sup>1</sup>

Name/Title of  
Deliverable/Milestone/Revision No. PFLOTRAN Development FY2022 / M3SF-22SN010304112  
Work Package Title and Number GDSA PFLOTRAN Development – SNL / SF-22SN01030411  
Work Package WBS Number. 1.08.01.03.04

Responsible Work Package Manager Michael Nole (Name/Signature)  
Date Submitted 08/01/2022

Quality Rigor Level for Deliverable/Milestone <sup>2</sup>	<input type="checkbox"/> QRL-1	<input type="checkbox"/> QRL-2	<input checked="" type="checkbox"/> QRL-3	<input type="checkbox"/> QRL-4
	<input type="checkbox"/> Nuclear Data			Lab QA Program <sup>3</sup>


This deliverable was prepared in accordance with Sandia National Laboratories  
(Participant/National Laboratory Name)

QA program which meets the requirements of  
 DOE Order 414.1     NQA-1     Other

**This Deliverable was subjected to:**

<input checked="" type="checkbox"/> Technical Review	<input type="checkbox"/> Peer Review
<b>Technical Review (TR)</b>	<b>Peer Review (PR)</b>
<b>Review Documentation Provided</b>	<b>Review Documentation Provided</b>
<input type="checkbox"/> Signed TR Report or,	<input type="checkbox"/> Signed PR Report or,
<input type="checkbox"/> Signed TR Concurrence Sheet or,	<input type="checkbox"/> Signed PR Concurrence Sheet
or,	
<input checked="" type="checkbox"/> Signature of TR Reviewer(s) below	<input type="checkbox"/> Signature of PR Reviewer(s)
below	

**Name and Signature of Reviewers**  
Tara LaForce  
\_\_\_\_\_  
\_\_\_\_\_

  
\_\_\_\_\_  
\_\_\_\_\_

**NOTE 1:** Appendix E should be filled out and submitted with the deliverable. Or, if the PICS:NE system permits, completely enter all applicable information in the PICS:NE Deliverable Form. The requirement is to ensure that all applicable information is entered either in the PICS:NE system or by using the NFCSC Document Cover Sheet.

- In some cases there may be a milestone where an item is being fabricated, maintenance is being performed on a facility, or a document is being issued through a formal document control process where it specifically calls out a formal review of the document. In these cases, documentation (e.g., inspection report, maintenance request, work planning package documentation or the documented review of the issued document through the document control process) of the completion of the activity, along with the Document Cover Sheet, is sufficient to demonstrate achieving the milestone.

**NOTE 2:** If QRL 1, 2, or 3 is not assigned, then the QRL 4 box must be checked, and the work is understood to be performed using laboratory QA requirements. This includes any deliverable developed in conformance with the respective National Laboratory / Participant, DOE or NNSA-approved QA Program.

**NOTE 3:** If the lab has an NQA-1 program and the work to be conducted requires an NQA-1 program, then the QRL-1 box must be checked in the work Package and on the Appendix E cover sheet and the work must be performed in accordance with the Lab’s NQA-1 program. The QRL-4 box should not be checked.

## ACKNOWLEDGEMENTS

This report incorporates contributions in Section 2 from the following co-authors:

Didem Beskardes: Section 2.2.4 (Hi-FEM)

David Fukuyama: Section 2.2.8 (Salt EOS), Section 2.2.9 (Solute Mass Balance)

Glenn Hammond: Section 2.1.2 (GDSA QA), Section 2.2.1 (Material Transform), Section 2.2.3 (Multicontinuum), Section 2.2.6 (Multicontinuum Gas Transport)

Rosie Leone: Section 2.1.2 (GDSA QA), Section 2.2.3 (Multicontinuum), Section 2.2.6 (Multicontinuum Gas Transport)

Peter Lichtner: Section 2.2.3 (Multicontinuum), Section 2.2.5 (Two-Phase Reactive Transport), Section 2.2.6 (Multicontinuum Gas Transport)

Paul Mariner: Section 2.2.7 (BECC Model)

Heeho Park: Section 2.2.7 (BECC Model), Section 2.3.1 (Applications of NTRDC), Section 2.4.3 (ANL Integration)

Matthew Paul: Section 2.3.2 (Characteristic Curves from Datasets)

Alex Salazar: Section 2.2.1 (Material Transform), Section 2.2.2 (3D Lookup Table)

The content described in Section 2.2.6 (Multicontinuum Gas Transport) was jointly funded by this work package and the SNL LYNM FY 2022 Containment Geochemistry task. Concept refinement and benchmark development were performed as part of this work package, and code implementation was funded by LYNM.

The authors thank Tara LaForce of Sandia National Laboratories (SNL) for her thoughtful technical review and staff from U.S. Department of Energy Office of Nuclear Energy (DOE-NE), Prasad Nair (DOE NE-81), for discussions, oversight, and guidance on topics addressed in this report. The authors thank Kris Kuhlman (SNL) for his contribution of a capillary pressure dataset for software testing outlined in this report, Jennifer Frederick (SNL) for the PFLOTRAN QA Toolbox tests used in development of the GDSA QA Test Framework, and Scott Painter (ORNL) for providing the unsaturated zone simulation inputs for testing new capillary pressure smoothing functions. The authors also thank the PETSc development team (Barry Smith, Satish Balay, Matthew Knepley, Richard Mills, Alp Dener, and Jed Brown) for assisting with the merge of the new NTRDC capability into PETSc.



## EXECUTIVE SUMMARY

The Spent Fuel & Waste Science and Technology (SFWST) Campaign of the U.S. Department of Energy (DOE) Office of Nuclear Energy (NE), Office of Spent Fuel & Waste Disposition (SFWD) is conducting research and development (R&D) on geologic disposal of spent nuclear fuel (SNF) and high-level nuclear waste (HLW). A high priority for SFWST disposal R&D is to develop a disposal system modeling and analysis capability for evaluating disposal system performance for nuclear waste in geologic media.

This report describes fiscal year (FY) 2022 accomplishments by the PFLOTRAN Development group of the SFWST Campaign. The mission of this group is to develop a geologic disposal system modeling capability for nuclear waste that can be used to probabilistically assess the performance of generic disposal concepts. In FY 2022, the PFLOTRAN development team made several advancements to our software infrastructure, code performance, and process modeling capabilities. These advancements included:

- Design of a new GDSA-specific QA testing framework
- Coordination with PETSc developers to deliver state-of-the-art new nonlinear solver capabilities (NTRDC), the performance of which we demonstrate on large multiphase problems
- Advances in multi-continuum flow and transport simulation capabilities including compatibility with the UFD Decay process model and gas transport
- Exploration of novel numerical techniques for modeling flow in fractured domains (HI-FEM)
- Introduction of a new module for applying reduced order models for material transformations
- New equations of state for brine systems
- A fully coupled single-solute option (e.g., salt) for multiphase flow simulations
- Advancements in gas phase representation in the transport equations
- An efficient dataset interpolation formulation for reading characteristic curves
- Conceptualization of a new buffer erosion and canister corrosion process model
- Numerous inter-laboratory collaborations
- An international beginner virtual short course

This report fulfills the GDSA PFLOTRAN Development Work Package Level 3 Milestone – *PFLOTRAN Development, FY2022, M3SF-22SN010304112*.

# CONTENTS

	<b>Page</b>
Acknowledgements.....	iv
Executive Summary.....	v
Nomenclature.....	xii
1. Introduction.....	1
1.1 PFLOTRAN.....	1
2. PFLOTRAN Development.....	4
2.1 Software Infrastructure.....	4
2.1.1 Jira.....	4
2.1.2 GDSA QA Test Framework.....	7
2.2 Process Modeling.....	24
2.2.1 Material Transform Process Model.....	24
2.2.2 3D Lookup Table Interpolation.....	35
2.2.3 Multi-continuum.....	40
2.2.4 Hi-FEM.....	49
2.2.5 Mass and Molar Representations of Two-Phase Reactive Transport Equations Including Aqueous, Gas and Mineral Reactions.....	54
2.2.6 Gas Transport Integration in Multicontinuum Transport.....	69
2.2.7 Buffer Erosion and Canister Corrosion.....	77
2.2.8 Salinity-Dependent Equations of State.....	81
2.2.9 Fully-Coupled Solute Mass Balance.....	87
2.3 Performance Improvements.....	94
2.3.1 Applications of New NTRDC Solver.....	94
2.3.2 Characteristic Curves from Datasets.....	104
2.4 Integration and Outreach.....	109
2.4.1 ORNL Collaboration.....	109
2.4.2 LBNL Collaboration.....	111
2.4.3 ANL Integration.....	112
2.4.4 International User Base.....	113
2.4.5 Short Course.....	114
2.4.6 Publications.....	115
3. References.....	116
4. Appendix A: PNNL PFLOTRAN Development Support.....	119
4.1 Introduction.....	119
4.2 Software Releases.....	120
4.3 Enhancements to GDSA Process Models.....	121
4.4 PFLOTRAN Bug Fixes.....	122
4.5 Updates to PFLOTRAN Software Infrastructure.....	123

## FIGURES

	<b>Page</b>
Figure 1.1-1 GDSA Framework schematic (Mariner et al., 2021) .....	2
Figure 1.1-2 Generic geologic disposal system conceptual model .....	3
Figure 2.1-1 Sprint tasks by category being addressed by the PFLOTRAN Development team from May 2020 to June 2022.....	4
Figure 2.1-2 Snapshot of the distribution of GDSA PFLOTRAN Development issues by issue type .....	5
Figure 2.1-3 Issues created (red) and issues resolved (green) over the period from June 2021 through June 2022 .....	6
Figure 2.1-4 Screenshot of list of requirements output by the QA-toolbox in HTML format.....	10
Figure 2.1-5 Screenshot of mapping requirements to the GDSA QA tests.....	11
Figure 2.1-6 Screenshot of results summary where each scenario corresponds to different grid sizes. Scenario one uses cell spacing of 10 m and scenario two uses cell spacing of 2 m.....	13
Figure 2.1-7 Screenshot of HTML output of the detailed results at one observation point for the Kolditz et al., 2015 Section 2.2.7 test.....	14
Figure 2.1-8 Screenshot of HTML output of the detailed results at a time slice for the Kolditz et al., 2015 Section 2.2.9 test with default no-flow boundaries. ....	16
Figure 2.1-9 Screenshot of HTML output of the detailed results at a time slice for the Kolditz et al., 2015 Section 2.2.8 test ran in serial, parallel, and a restart file at 0.04 days. ....	17
Figure 2.1-10 Results summary of the TOUGH3 vs PFLOTRAN variably saturated flow test.....	19
Figure 2.1-11 Detailed results of the TOUGH3 vs PFLOTRAN variably saturated flow test. ....	20
Figure 2.1-12 TOUGH3 vs PFLOTRAN variably saturated flow test with heterogenous permeability and porosity. ....	22
Figure 2.1-13 Volumetric source sink QA test looking at mass balance output. Mass is negative because it is flowing out of the domain.....	23
Figure 2.2-1 An example schematic showing process model coupling of the Material Transform module with multiphase flow, reactive transport, and UFD Decay. ....	24
Figure 2.2-2: View of 1-D verification problem domain with coloring for new smectite fraction output variable active in one grid cell with the material transform process model active. ....	32
Figure 2.2-3: PFLOTRAN smectite fraction as a function of time ( $\log_{10}$ scale) for both S-I models compared to analytical solutions. ....	33
Figure 2.2-4: Shift in permeability as a function of time ( $\log_{10}$ scale) from both S-I models compared to analytical solutions. ....	34
Figure 2.2-5: Shift in cesium $K_d$ as a function of time ( $\log_{10}$ scale) from both S-I models compared to analytical solutions. ....	34

Figure 2.2-6: Radionuclide mass fractions for MPC-32-162 with a criticality event at $P = 4 \text{ kW}$ , $t_0 = 500 \text{ y}$ .....	36
Figure 2.2-7 Slab geometry from Iraola et al., 2019.....	41
Figure 2.2-8 Nested cubes geometry, taken from Lichtner and Karra, 2014.....	42
Figure 2.2-9 Concentration in the fracture with a decaying isotope (dotted line) versus non decaying tracer (solid line).....	46
Figure 2.2-10 Concentration in the matrix with a decaying isotope (dotted line) versus non decaying tracer (single line).....	46
Figure 2.2-11 Four-fracture pressure solution for ECPM used as steady state solution for the transport problem.....	47
Figure 2.2-12 Mean concentration of isotopes in the entire 4-fracture system.....	48
Figure 2.2-13 Moles of each isotope passing through 4-fracture outflow ( $x=500 \text{ m}$ ). .....	48
Figure 2.2-14 (a) Illustration of lower dimensional model features in a 3D conforming tetrahedral finite element mesh (b) Hierarchical material representations at a tetrahedron (volume $e$ , facet $e$ , edge $e$ ). $\mathbf{K}_e$ is the hydraulic conductivity, $\mathbf{f}_e$ is the conductance and $\mathbf{t}_e$ is the conductivity-area product. $\mathbf{e}_1$ , $\mathbf{e}_2$ and $\mathbf{e}_3$ denote the principal axes of a reference frame.....	50
Figure 2.2-15 Cross section of the tetrahedral mesh of the four-fracture model. ....	51
Figure 2.2-16 Pressure distribution of the four-fracture model obtained from <i>Hi</i> -FEM simulation.....	52
Figure 2.2-17 The nodal velocity field components $q_x$ , $q_y$ and $q_z$ of the four-fracture model. ....	53
Figure 2.2-18 Analytical solution showing gas transport via diffusion in secondary continuum only, keeping primary continuum concentration constant.....	70
Figure 2.2-19 Modified Tang et al., 1981 (solid) comparison with PFLOTTRAN (dotted) in the fracture at 100 and 5000 days.....	73
Figure 2.2-20 Modified Tang et al., 1981 (solid) comparison with PFLOTTRAN (dotted) in the matrix, 1 m down the fracture at 100 and 5000 days.....	74
Figure 2.2-21 Domain set up for unstructured explicit grid. Primary represents fracture and secondary represents matrix. ....	75
Figure 2.2-22 Comparison of aqueous concentration between the dual continuum model (orange dotted) and explicit unstructured grid (blue solid) at the fracture/primary cell denoted by the black star in Figure 2.2-21. ....	76
Figure 2.2-23 Comparison of aqueous concentration between the dual continuum model (orange dotted) and explicit unstructured grid (blue solid) at the matrix/secondary cell denoted by the yellow star Figure 2.2-21. ....	76
Figure 2.2-24 Conceptual model of buffer erosion due to a flowing fracture (Fig 6-108, Posiva 2013).....	78
Figure 2.2-25 Solubility of salt in water as a function of temperature.....	81
Figure 2.2-26 Density of brines as a function of mass fraction and temperature (Left: Sparrow, Right: Batzle and Wang). The dashed line indicates the density of a brine with a salt concentration at solubility.....	82

Figure 2.2-27 Vapor pressure as a function of salt concentration (Left: Sparrow, Right: Haas). Vapor pressure of brines decreases with increased mass fraction. The vapor pressure lowering with increased salt concentration raises the boiling point of water. The dashed line indicates vapor pressure at solubility. ....	83
Figure 2.2-28 Specific enthalpy as a function of salt concentration. ....	86
Figure 2.2-29 Schematic of the Elder problem. The system has a length to height ratio of 4:1, constant concentration boundaries on the bottom and top, constant pressure boundaries at the top corners, and no-flux boundaries on all sides. ....	89
Figure 2.2-30 Comparison of density-driven flow between a fully implicit solute implementation and a sequentially coupled flow and transport implementation. Concentration contours of 60% (yellow) and 20% (blue) of the maximum concentration (0.28 mass frac.) are displayed, along with a comparison to the concentration contours from the Voss and Souza (Voss & Souza, 1987) implementation (black). ....	90
Figure 2.2-31 Porosity evolution in the Olivella et al. (2011) benchmark problem. ....	92
Figure 2.2-32 Liquid and gas flow opposite to each other. Gas flows in the positive x direction (hot to cold), and liquid flows in the negative x direction (cold to hot). ....	93
Figure 2.3-4 Cropped view of the symmetrical half of the unsaturated zone nuclear waste repository simulation domain where higher temperatures are seen in the waste disposal drifts (pink lines) ....	95
Figure 2.3-5 Top view of the field-scale generic waste repository zoomed into the waste area. The lighter orange is the excavated drifts backfilled with engineered barrier after the closure. The darker orange is the damaged rock zone around the excavation. The heat source grid cells are the 5 m long waste packages in dark red. The light blue is the host rock, and the full-scale domain is shown in Figure 2.3-4. ....	96
Figure 2.3-6 Different power source profile by different waste package. Each waste package contains the indicated number of pressurized water reactor (PWR) fuel assemblies. They are a simple time-varying source term in the simulation ....	97
Figure 2.3-7 Wall clock time, Newton and linear solver iteration counts, and time step cut counts for the fully-refined model run with the three (12, 24, 37) power levels on 144 cores using NTR-HII ....	98
Figure 2.3-8 Time history of nonlinear iterations after time step cuts, linear iterations and time step size for the fully-refined model run with NTR. The left figures show the time history of time step cuts and the number of nonlinear iterations needed to complete the time step. The right figures show the number of linear iterations and the time step size. ....	99
Figure 2.3-9 Different discretization: refinement level-2 (2.11M grid cells, left), level-1 (285K grid cells, middle), and level-0 (41K grid cells, right). ....	100
Figure 2.3-10 Initial condition of the simulation in temperature (left), liquid saturation (middle), and liquid pressure (right). ....	101
Figure 2.3-11 Temperature distribution at the waste package depth of 255 m below the surface at 100 years after the simulation began at level-2 refinement, level-1, and level-0 from left to right ....	101
Figure 2.3-12 Liquid saturation for different discretization at 100-year simulation time. ....	102

---

Figure 2.3-1 Capillary pressure data from Heath et al. (2021) along with a Van Genuchten analytical curve fit and a lookup table (output using the TEST option) using linear interpolation between data points. ....	105
Figure 2.3-2 Relative permeability data from Heath et al. (2021) along with a Van Genuchten-Mualem analytical curve fit with parameters from the capillary pressure fit, re-fit parameters, and a lookup table (output using the TEST option) using linear interpolation between data points. ....	106
Figure 2.3-3 Absolute value of the derivative of capillary pressure with respect to liquid saturation for the analytical Van Genuchten curve fit and the lookup table using linear interpolation between data points. ....	107
Figure 2.4-1 Cut-out of the computational domain described in Price et al., 2020 .....	109
Figure 2.4-2 Total global hits from individual users to the PFLOTTRAN website, from May 01, 2021 to April 30, 2022.....	113

## TABLES

	Page
Table 2.1-1 Requirements for RICHARDS mode in PFLOTRAN with associated QA tests for each requirement. ....	8
Table 2.2-1 Definition of the material transform process model (“smectite-to-illite”) and a material (“bentonite”) with the PM active and isotropic permeability that will be modified.....	26
Table 2.2-2 The UFD Decay process model block showing $K_d$ values of “bentonite” that can be modified by the material transform model. ....	27
Table 2.2-3 The material transform process model block with material transformation “mtf_bentonite” that uses S-I model to modify permeability and $K_d$ of Cs and Sr. ....	27
Table 2.2-4 The four functional forms available to modify permeability. these can also be used to modify $K_d$ values. ....	31
Table 2.2-5 Parameters used for the two S-I models in the verification test .....	33
Table 2.2-6 Maximum and median relative differences (in percent) in the parameters of interest between the PFLOTRAN output and the analytical solution. ....	33
Table 2.2-7 The waste form process model showing two active radionuclides for use in the 3-D LUT. ....	37
Table 2.2-8 Portions of the criticality inventory lookup table “crit_inv.txt” showing two active radionuclides and an additional radionuclide not employed in the simulation.....	38
Table 2.2-9 Multiple continuum input card with descriptions of parameters and applicable multiple continuum geometry parameters that each input can be applied to. Values listed are examples and not physically representative.....	43
Table 2.2-10 UFD Decay test problem values.....	45
Table 2.2-11 Parameter values used in the Hi-FEM simulation for the four-fracture problem.....	52
Table 2.2-12 Parameters for modified Tang et al., 1981 benchmark solution.....	72
Table 2.2-13 Parameters used for unstructured explicit grid comparison.....	75
Table 2.2-14 Constants for vapor pressure calculation by Haas.....	85
Table 2.2-15 Phase states and corresponding primary variables for an insoluble rock matrix.....	88
Table 2.2-16 Phase states and corresponding primary variables for a soluble rock matrix.....	88
Table 2.3-2 Weak scaling test parameters .....	103
Table 2.3-3 Weak scaling test results.....	103
Table 2.3-1 Van Genuchten parameters for the a) capillary pressure function and b) re-fit for the relative permeability function.....	106
Table 2.4-1 Linear and nonlinear solver iterations and wall clock time for bounding power and infiltration rate simulations for a criticality consequence analysis study that previously was unachievable without characteristic curve extensions.....	110

## NOMENCLATURE

ANL	Argonne National Laboratory
DCDM	Dual Continuum Disconnected Matrix
DFN	Discrete Fracture Network
DOE	U.S. Department of Energy
DPC	Dual-Purpose Canister
EBS	Engineered Barrier System
ECPM	Equivalent Continuous Porous Medium
GDSA	Geologic Disposal Safety Assessment
HLW	High-level Nuclear Waste
LBNL	Lawrence Berkeley National Laboratory
NE	DOE Office of Nuclear Energy
ORNL	Oak Ridge National Laboratory
PNNL	Pacific Northwest National Laboratory
QA	Quality Assurance
R&D	Research & Development
SFWD	Spent Fuel & Waste Disposition
SFWST	Spent Fuel & Waste Science and Technology
S-I	Smectite-to-Illite
SNF	Spent Nuclear Fuel
SNL	Sandia National Laboratories
TH	Thermal-Hydrological
V&V	Verification & Validation
WF	Waste Form



(This page left intentionally blank.)

## 1. INTRODUCTION

The Spent Fuel & Waste Science and Technology (SFWST) Campaign of the U.S. Department of Energy (DOE) Office of Nuclear Energy (NE), Office of Spent Fuel & Waste Disposition (SFWD) is conducting research and development (R&D) on geologic disposal of spent nuclear fuel (SNF) and high-level nuclear waste (HLW). A high priority for SFWST disposal R&D is disposal system modeling (DOE 2012, Table 6; Sevougian et al., 2019; Sassani et al., 2021). The SFWST GDSA PFLOTRAN Development work package is charged with developing subsurface simulation software for use in system performance assessment of nuclear waste disposal in geologic media. This report fulfills the requirements of the GDSA PFLOTRAN Development work package (SF- 22SN01030411) Level 3 Milestone – PFLOTRAN Development FY2022, M3SF- 22SN010304112.

### 1.1 PFLOTRAN

PFLOTRAN (Hammond et al., 2014; Lichtner and Hammond, 2012) is an open source, massively parallel multiphase flow and reactive transport simulator designed to leverage high-performance computing infrastructure for subsurface earth systems applications. PFLOTRAN has been employed on petascale leadership-class DOE computing resources (e.g., Jaguar [at Oak Ridge National Laboratory (ORNL)]) and to simulate THC processes at the Nevada Test Site (Mills et al., 2007), multiphase CO<sub>2</sub>-H<sub>2</sub>O injection for carbon sequestration (Lu and Lichtner, 2007), CO<sub>2</sub> leakage within shallow aquifers (Navarre-Sitchler et al., 2013), uranium fate and transport at the Hanford 300 Area (Hammond and Lichtner, 2010; Chen et al., 2013), surface-subsurface flow coupling (Wu et al., 2021), geothermal systems (Alt-Epping et al., 2021), and multiphase liquid-gas-gas hydrate systems (White et al., 2020). PFLOTRAN recently underwent qualification for use as a multiphase flow performance assessment code at the Waste Isolation Pilot Plant (WIPP), and it is currently undergoing qualification for WIPP's nuclear waste transport performance assessment calculations.

PFLOTRAN solves coupled systems of nonlinear partial differential equations describing non-isothermal multiphase flow and reactive transport in porous media. Parallelization is achieved through domain decomposition using the Portable Extensible Toolkit for Scientific Computation (PETSc) (Balay et al., 2013). PETSc provides a flexible interface to data structures and solvers that facilitates the use of parallel computing. PFLOTRAN is written in modern Fortran and leverages state of the art Fortran programming (Fortran classes, pointers to procedures, etc.) to support its ground-up object-oriented design. The modular design of the code allows developers to integrate a custom set of process models and time integrators for simulating different surface and subsurface multi-physics processes. PFLOTRAN employs a single, unified framework for simulating multi-physics processes on both structured and unstructured grid meshes (i.e., there is no duplication of the code that calculates multi-physics process model functions in support of structured or unstructured meshes). The code requires a small, select set of third-party libraries (e.g., MPI, PETSc, BLAS/LAPACK, HDF5, METIS/PARMETIS). Both the unified structured/unstructured framework and the limited number of third-party libraries greatly facilitate usability for the end user.

PFLOTRAN serves as the multi-physics simulation engine of the GDSA Framework (Figure 1.1-1). As such, PFLOTRAN has been developed to model various components of the radionuclide source term such as waste form inventory and waste form degradation, radioactive isotope decay and ingrowth, and radionuclide release. These are coupled to the flow and transport solvers which then can model several processes including multiphase non-isothermal advection, diffusion, and dispersion through porous media in either a single- or multi-continuum formulation while considering chemical reactions and isotope decay/ingrowth in the pore system. The flow and transport models ultimately feed a biosphere model which can be used to estimate dose. This report details the various components of the source term, flow and transport models, and updated numerical techniques that have been enhanced this year. The new

functionality described here is currently available in the master branch of the PFLOTRAN git repository available at [www.bitbucket.org/pflotran/pflotran](http://www.bitbucket.org/pflotran/pflotran) and is documented at [doc-dev.pflotran.org](http://doc-dev.pflotran.org) unless otherwise stated.

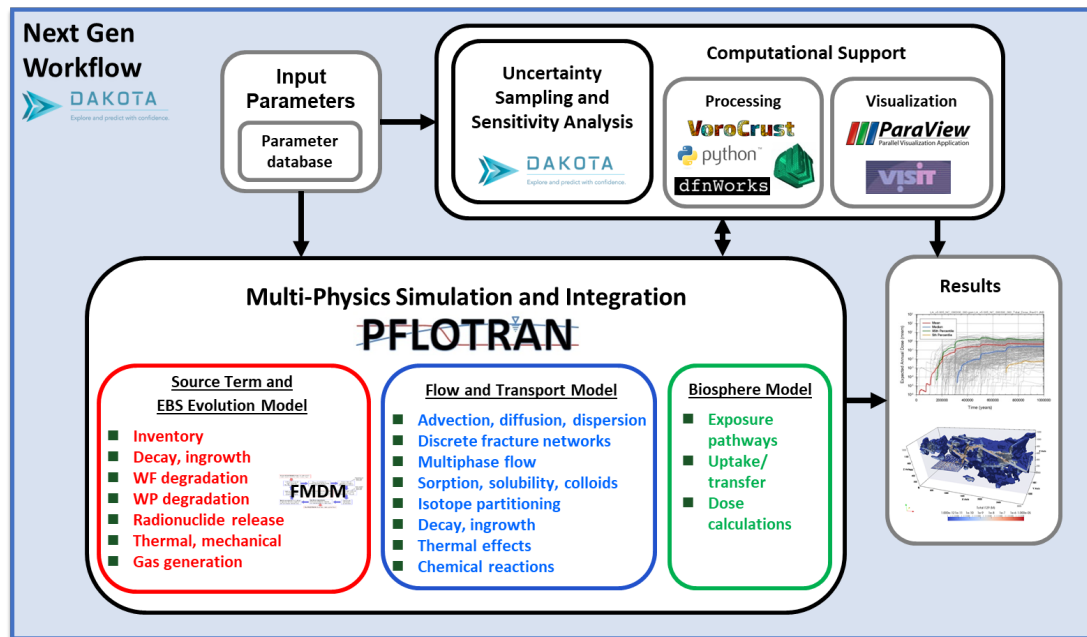


Figure 1.1-1 GDSA Framework schematic (Mariner et al., 2021)

As the multi-physics simulation engine of the GDSA Framework (Figure 1.1-1), PFLOTRAN integrates all components of the generic disposal system conceptual model (Figure 1.1-2) through either fully coupled simulation (e.g., multiphase fluid flow and thermal effects due to waste package heating), sequential coupling (e.g., flow and transport of radionuclides which can include decay, sorption, partitioning, and ingrowth), reduced order modeling (e.g., reduced-order geomechanics as described in Chang et al. [2021]), or post-processing (e.g., biosphere processes).

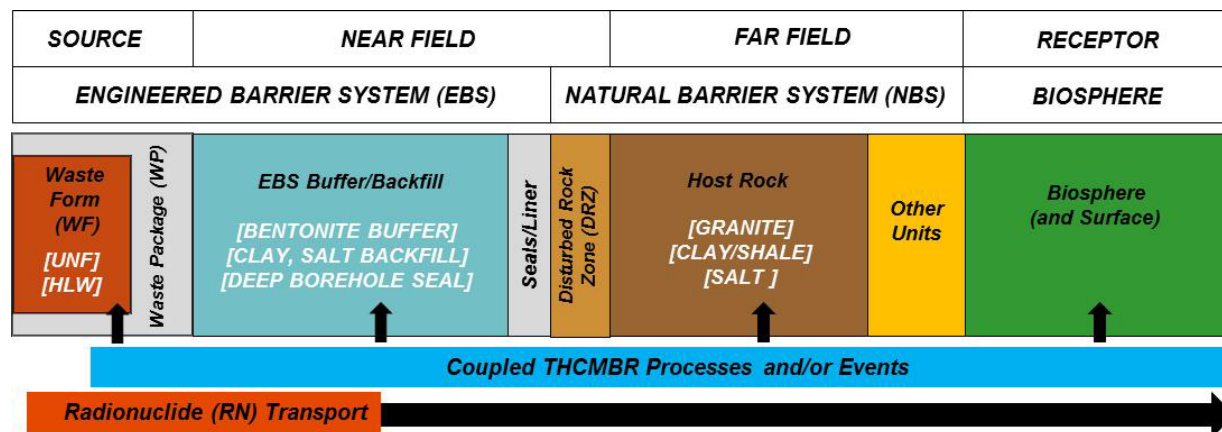


Figure 1.1-2 Generic geologic disposal system conceptual model

Users can select unique combinations of process models and flow or transport coupling to tailor their models to their needs for a given repository concept of interest. To date, GDSA has been involved with the use and development of fluid flow modes including Richards mode (single-phase, variably saturated flow), Thermo-Hydraulic (TH) mode (single-phase flow coupled to heat transport), and GENERAL mode (two-phase miscible flow coupled to heat transport, with a new option being developed in FY22 to also couple a solute mass balance for, e.g., brine systems). Additionally, GDSA makes use of chemistry libraries developed for Global Implicit Reactive Transport (GIRT) mode which can be used in coordination with multi-continuum (dual porosity) fracture-matrix transport, and the PFLOTRAN team is currently developing Nuclear Waste Transport (NWT) mode for modeling chemical transport in multiphase systems that experience full dry out. The Waste Form Process Model is implemented as a source term to consider waste canister degradation and waste form dissolution to release radionuclides into pore fluids in coordination with the Used Fuel Disposition (UFD) decay, sorption, partitioning, and ingrowth process model. Users can also specify specific fuel matrix degradation (FMD) process models. Additionally, users have the option of including reduced order models for approximating processes like bentonite buffer swelling and high-temperature effects on material properties such as smectite illitization.

PFLOTRAN’s default linear solver is the BiCGSTAB solver (Saad et al., 1993) with ILU(0) preconditioning (in parallel, block Jacobia with ILU[0] in each block). The default solvers can be deficient for large-scale repository simulations, so alternative linear solver algorithms have been developed and implemented which include algorithms like Hammersley-Ponting (Ponting et al., 2008) and Bui (Bui et al., 2017), which apply a two-stage combinative constrained pressure residual (CPR) AMG preconditioner. The Flexible Generalized Minimal Residual method, or FGMRES, is preferred over traditional GMRES or BiCGSTAB because it can accommodate changing preconditioners, like CPR (Nole et al., 2021; Park et al., 2021). In addition to advanced linear solver options, PFLOTRAN has recently released a new nonlinear solver (the Newton Trust Region Dogleg Cauchy, or NTRDC, method) that exploits a trust region approach to the nonlinear solution search and can accommodate primary variable switching inherent to multiphase miscible flow in GENERAL mode (Park et al., 2021).

## 2. PFLOTRAN DEVELOPMENT

### 2.1 Software Infrastructure

Development of the GDSA QA Test Framework and the use of issue management software, Jira, are intended to increase confidence in PFLOTRAN code developments for the GDSA program. The GDSA QA Test Framework is being designed to provide an extendable and modular approach to verifying that developments in PFLOTRAN are consistent with expectations from GDSA process modelers. In addition, the Jira issue tracker and task management software has facilitated more streamlined bug reporting and requests for new process models. Taken together, these software infrastructure improvements are allowing the PFLOTRAN team to integrate more tightly with GDSA process modelers and engender confidence that new code additions are meeting modelers’ needs.

#### 2.1.1 Jira

This year, the PFLOTRAN development team continued to refine our use of Agile software development practices using the Jira issue tracker and project management software, which seamlessly integrates software bug reporting and requests for code enhancements or new process modeling capabilities from GDSA collaborators with PFLOTRAN’s Bitbucket code repository. Using Jira, the PFLOTRAN development team re-prioritizes issues on two-week cycles to maintain tight coordination with process modelers and transparency in addressing user issues like bugs or requests for new or improved process models.

Beginning late in FY2020, the PFLOTRAN development team has been working in 2-week development sprints where issues are re-prioritized at the end of each sprint considering any new issues that have been flagged by developers or requested by users. From May 2020 to June 2022, we have nearly tripled the total number of issues that have been pursued by the development team (Figure 2.1-1). The team has also seen commensurate increase in the number of issues flagged as “Done” over that time period, indicating a steady increase in the breadth of development activities that the team is accomplishing.

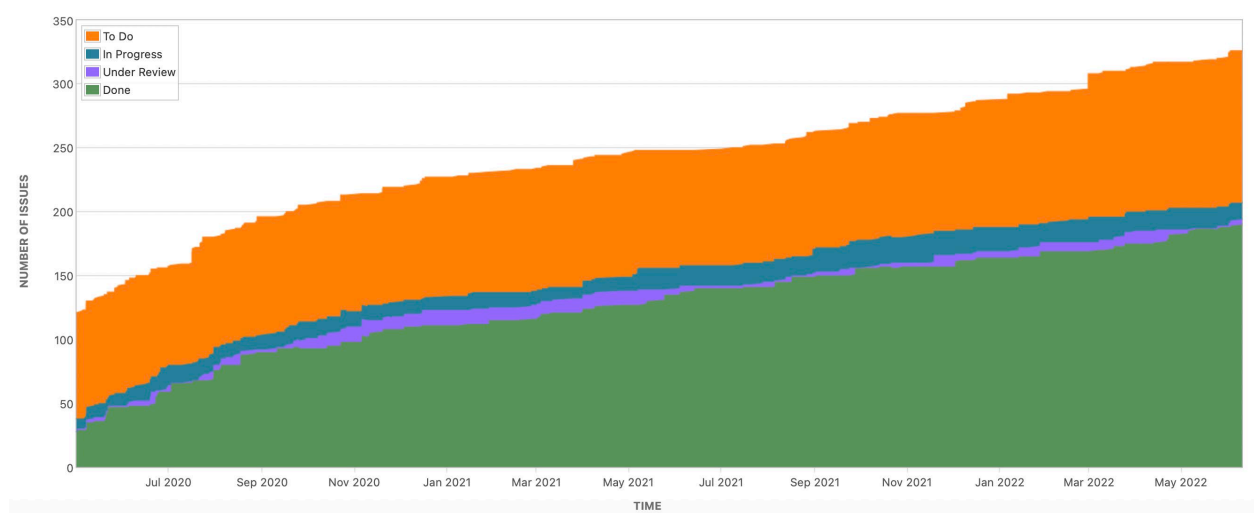
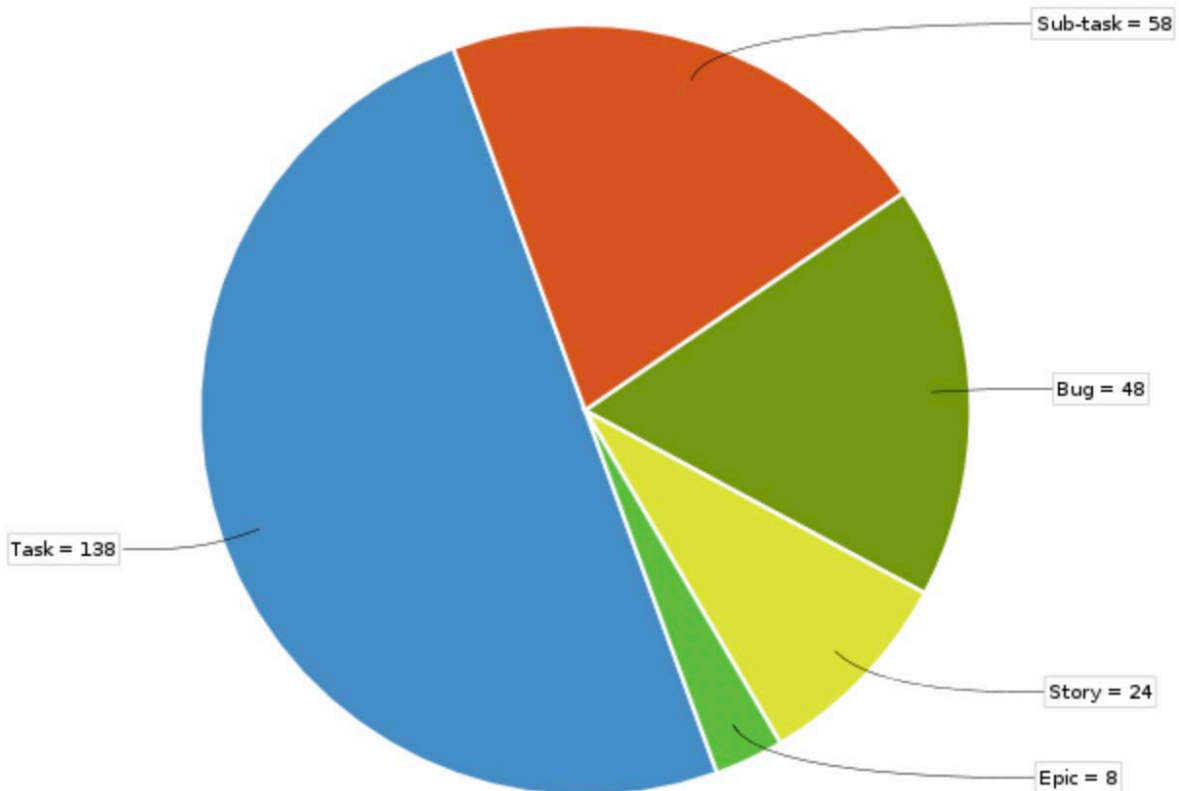


Figure 2.1-1 Sprint tasks by category being addressed by the PFLOTRAN Development team from May 2020 to June 2022

Most issues being pursued by the development team fall under the “task” and “subtask” category, which typically encompass adding new features like an equation of state to existing process models to the

code or making certain algorithms more streamlined or efficient (see Nole et al [2021] for a description of issue categories as they pertain to GDSA PFLOTRAN development activities). Stories are arrangements of tasks that constitute a set of interacting functions for a new or existing isolated process model. Epics are significant code enhancements, such as a new flow or transport mode. Roughly 80% of our development issues relate to these forms of code enhancements, while roughly 20% of the issues are bug reports (Figure 2.1-2).



**Figure 2.1-2 Snapshot of the distribution of GDSA PFLOTRAN Development issues by issue type**

Over the course of FY2022, the PFLOTRAN development team has resolved nearly 40 issues relating to GDSA (Figure 2.1-3). The work described in this report is included in this issue count. Ideally, the development team would be resolving a given set of issues within each 2-week sprint, so the current pace of issue resolution suggests that tasks have not been sufficiently sub-divided into small enough tasks that can effectively be completed in the 2-week timeframe. This is tricky to get right since the nature of code development for research and development is inherently open-ended and uncertain. However, the team is striving to refine our task description more effectively into smaller sub-tasks because we believe it will allow us to be more transparent and more responsive to task re-prioritization at the end of each sprint.

This chart shows the number of issues **created** vs. the number of issues **resolved** in the last 365 days.

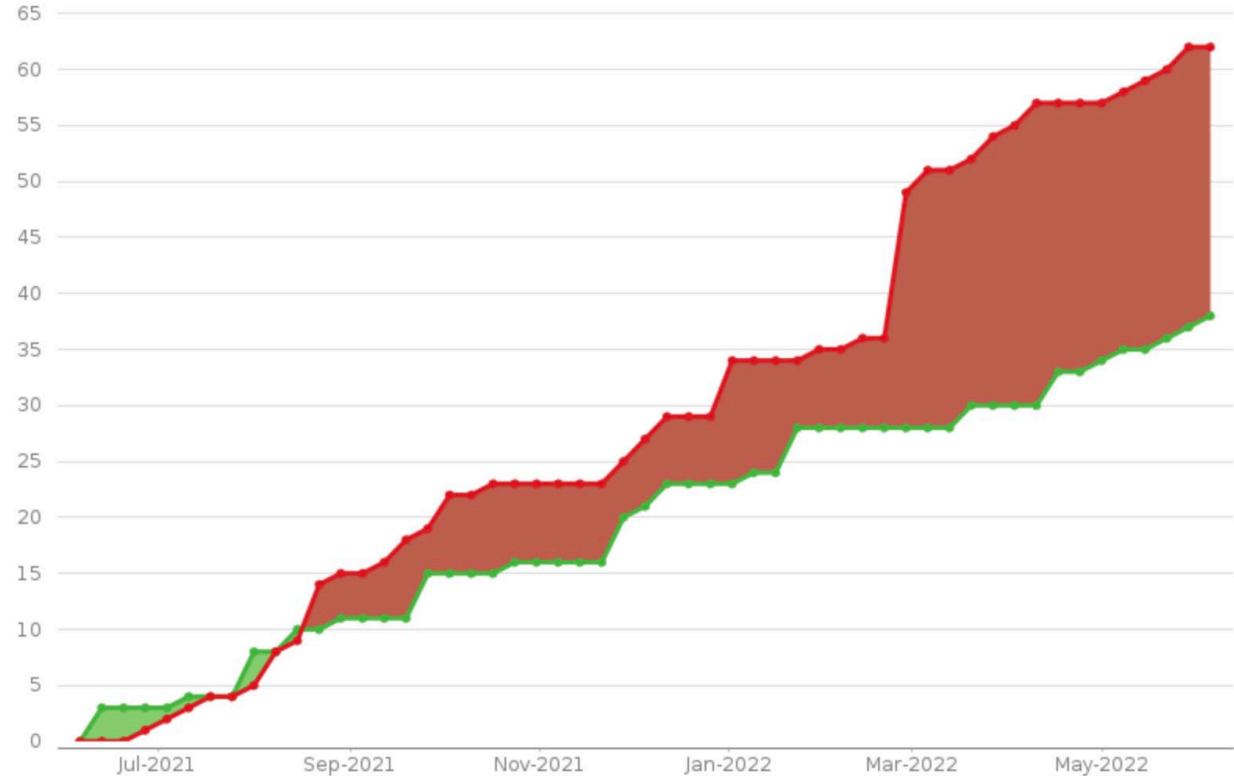


Figure 2.1-3 Issues created (red) and issues resolved (green) over the period from June 2021 through June 2022

### **2.1.2 GDSA QA Test Framework**

Quality Assurance (QA) is important to establish confidence in PFLOTRAN calculations and technical requirements. In code development, QA includes performing verification and validation (V&V) studies to compare simulation outputs with other simulators, analytical solutions, or experimental data. In complex scenarios, analytical solutions may be too simple for comparison and other simulators must be used to validate results. Therefore, it is important for a V&V framework to be flexible to allow comparison with multiple simulators to ensure validation across the entire code.

This fiscal year, a GDSA specific QA was developed expanding on the existing test suite (Frederick, 2018) and utilizing QA-toolbox software described in Mariner et al. (2020). A first draft of a list of requirements for RICHARDS mode in PFLOTRAN was developed to satisfy the functionality needed for GDSA (Table 2.1-1). Existing tests were used and expanded to satisfy the requirements and several new tests were created including a comparison with the TOUGH3 simulator. All tests utilized were run using the Richards flow mode and tests could satisfy multiple requirements.



**Table 2.1-1 Requirements for RICHARDS mode in PFLOTTRAN with associated QA tests for each requirement.**

<b>Requirement</b>	<b>QA Tests</b>
R1: PFLOTTRAN shall simulate single-phase fluid flow based on Darcy's law	All tests
R2: PFLOTTRAN shall simulate variably saturated fluid flow	TOUGH3 vs PFLOTTRAN
R3: PFLOTTRAN shall simulate fluid flow in a heterogeneous porous medium	TOUGH3 vs PFLOTTRAN
R4: PFLOTTRAN shall support Dirichlet boundary conditions over a boundary region of a domain	Kolditz et al., 2015 Section 2.2.6, Kolditz et al., 2015 Section 2.2.7, Kolditz et al., 2015 Section 2.2.10, TOUGH3 vs PFLOTTRAN
R5: PFLOTTRAN shall support Neumann boundary conditions over a boundary region of a domain	Kolditz et al., 2015 Section 2.2.8, Kolditz et al., 2015 Section 2.2.9, Kolditz et al., 2015 Section 2.2.10
R6: PFLOTTRAN shall support zero flux boundary conditions over a boundary region of a domain (i.e., default "no flow" boundary condition)	Kolditz et al., 2015 Section 2.2.9
R7: PFLOTTRAN shall support hydrostatic Dirichlet boundary conditions over a boundary region of a domain	Kolditz et al., 2015 Section 2.2.6
R8: PFLOTTRAN shall support sources/sinks using a mass rate expression	TOUGH3 vs PFLOTTRAN
R9: PFLOTTRAN shall support sources/sinks using a volumetric rate expression	Volumetric source/sink test
R10: PFLOTTRAN shall support the ability to specify the initial state of primary dependent variables in the domain (initial condition)	Kolditz et al., 2015 Section 2.2.9, Kolditz et al., 2015 Section 2.2.10, TOUGH3 vs PFLOTTRAN
R11: PFLOTTRAN shall calculate liquid saturation using the van Genuchten pressure-saturation relationship	TOUGH3 vs PFLOTTRAN
R12: PFLOTTRAN shall calculate liquid relative permeability using the van Genuchten-Mualem relationship	TOUGH3 vs PFLOTTRAN
R 13: PFLOTTRAN shall support heterogeneous porosity (material property)	TOUGH3 vs PFLOTTRAN
R14: PFLOTTRAN shall support heterogeneous intrinsic permeability (material property)	TOUGH3 vs PFLOTTRAN
R15: PFLOTTRAN shall support Cartesian grids (structured)	All tests
R16: PFLOTTRAN shall support unstructured grids defined by elements and vertices (implicit unstructured)	Kolditz et al., 2015 Section 2.2.7
R17: PFLOTTRAN shall support unstructured grids defined by cells [coordinates and volumes] and connectivity [distances and areas] (explicit unstructured)	Kolditz et al., 2015 Section 2.2.7
R18: PFLOTTRAN shall support the checkpoint/restart (i.e., the ability to save and restart a simulation at any point in time)	Kolditz et al., 2015 Section 2.2.8
R19: PFLOTTRAN shall output state variables for all grid cells at a specified time (snapshot file)	Kolditz et al., 2015 Section 2.2.6, Kolditz et al., 2015 Section 2.2.8, Kolditz et al., 2015 Section 2.2.9, Kolditz et al., 2015 Section 2.2.10, TOUGH3 vs PFLOTTRAN
R20: PFLOTTRAN shall output state variables at a specified location for over time (observation file)	Kolditz et al., 2015 Section 2.2.7, Kolditz et al., 2015 Section 2.2.10
R21: PFLOTTRAN shall output state variable instantaneous and cumulative fluxes at cell faces over time (mass balance file)	Volumetric source/sink
R22: PFLOTTRAN shall support serial and parallel execution	Kolditz et al., 2015 Section 2.2.8

The QA-toolbox was developed to perform code V&V for PFLOTRAN. The toolbox is a modular, Python-based V&V testing framework for vetting GDSA tests. The toolbox is therefore flexible to accommodate addition of new tests, and it is written in a common programming language with established data visualization and analysis libraries. The testing framework installs multiple simulators and suites of test problems to compare PFLOTRAN solutions against existing simulators, analytical solutions, and/or datasets. The toolbox is designed to be completely automated and user friendly when adding new tests or simulators to compare against. The testing framework uses Python wrappers to read simulator output, plot solutions, and return error metrics. The QA-toolbox is described in more detail in Mariner et al. (2020).

QA documentation is automatically created using the input parameters specified by the user and the accompanying results calculated from the QA-toolbox. This includes a results summary, problem description, detailed results, and links to download the input decks that were used to run the simulations. The results summary includes output values, simulation times, and locations of the maximum and average errors within the model domain with links to more detailed results at these locations. Detailed results include a table of the average and maximum errors, their associated locations or times, and plots of the solution and error at each point in time or space that the user specifies. Once complete, the V&V testing framework automatically documents results in reStructuredText and generates HTML files using Sphinx (<http://www.sphinx-doc.org/>).

Several advancements were made to the QA-toolbox. The QA-toolbox now takes in a list of requirements provided by the user. Each requirement is assigned to a keyword which is then matched to the tests provided by the user. When creating a test, the user specifies attributes of the test which are mapped to the requirement. The list of requirements is now the main page provided by the HTML files (Figure 2.1-4), and clicking on each requirement shows the tests belonging to each requirement (Figure 2.1-5). Requirements can have multiple tests and tests can satisfy multiple requirements. Other advancements made include comparison of mass balance files outputted by PFLOTRAN, the ability to run tests in parallel, comparisons of multiple tests with one analytical solution, and appearance upgrades for the figures (for example, adding in different line styles to 1D plots).

The screenshot displays a web page for 'GDSA QA Documentation'. The page has a green header with 'GDSA QA documentation »' on the left and 'next | index' on the right. A left sidebar contains a 'Table Of Contents' with 'GDSA QA Documentation' and sub-items 'INTRODUCTION AN SCOPE' and 'REQUIREMENTS'. Below this is a 'Next topic' section for 'Functional Requirements' and a 'Quick search' box with a 'Go' button. The main content area has a blue header 'GDSA QA Documentation', followed by a blue section 'INTRODUCTION AN SCOPE' with the text 'User inputs into text file an intro for the QA'. Below that is another blue section 'REQUIREMENTS' containing a bulleted list of 22 requirements (R 1 to R 22) for the pflotran software. The footer of the page is green with 'GDSA-QA documentation »' on the left and 'next | index' on the right, and a small copyright notice: '© Copyright 2020, Rosie Leone. Created using Sphinx 1.6.7.'

GDSA QA documentation » next | index

Table Of Contents

- GDSA QA Documentation
  - INTRODUCTION AN SCOPE
  - REQUIREMENTS

Next topic

Functional Requirements

Quick search

## GDSA QA Documentation

### INTRODUCTION AN SCOPE

User inputs into text file an intro for the QA

### REQUIREMENTS

- Functional Requirements
  - R 1 pflotran shall support hydrostatic dirichlet boundary conditions over a boundary region of a domain
  - R 2 pflotran shall simulate single-phase fluid flow based on darcy's law
  - R 3 pflotran shall support dirichlet boundary conditions over a boundary region of a domain
  - R 4 pflotran shall support cartesian grids (structured)
  - R 5 pflotran shall output state variables at a specified location for over time (observation file)
  - R 6 pflotran shall support unstructured grids defined by elements and vertices (implicit unstructured)
  - R 7 pflotran shall support unstructured grids defined by cells [coordinates and volumes] and connectivity [distances and areas] (explicit unstructured)
  - R 8 pflotran shall support neumann boundary conditions over a boundary region of a domain
  - R 9 pflotran shall output state variables for all grid cells at a specified time (snapshot file)
  - R 10 pflotran shall support serial and parallel execution
  - R 11 pflotran shall support the checkpoint/restart (i.e., the ability to save and restart a simulation at any point in time)
  - R 12 pflotran shall support zero flux boundary conditions over a boundary region of a domain
  - R 13 pflotran shall support the ability to specify the initial state of primary dependent variables in the domain (initial condition)
  - R 14 pflotran shall simulate variably saturated fluid flow
  - R 15 pflotran shall support sources/sinks using a mass rate expression
  - R 16 pflotran shall calculate liquid saturation using the van genuchten pressure-saturation relationship
  - R 17 pflotran shall calculate liquid relative permeability using the van genuchten-mualem relationship
  - R 18 pflotran shall simulate fluid flow in a heterogeneous porous medium
  - R 19 pflotran shall support sources/sinks using a volumetric rate expression
  - R 20 pflotran shall output state variable instantaneous and cumulative fluxes at cell faces over time (mass balance file)
  - R 21 pflotran shall support heterogeneous porosity (material property)
  - R 22 pflotran shall support heterogeneous intrinsic permeability (material property)

GDSA-QA documentation » next | index

© Copyright 2020, Rosie Leone. Created using Sphinx 1.6.7.

Figure 2.1-4 Screenshot of list of requirements output by the QA-toolbox in HTML format

Table Of Contents	Functional Requirements
<p>Functional Requirements</p> <ul style="list-style-type: none"> <li>R 1 pflotran shall support hydrostatic dirichlet boundary conditions over a boundary region of a domain</li> <li>R 2 pflotran shall support dirichlet boundary conditions over a boundary region of a domain</li> <li>R 3 pflotran shall support cartesian grids (structured)</li> <li>R 4 pflotran shall simulate single-phase fluid flow based on darcy's law</li> <li>R 5 pflotran shall output state variables for all grid cells at a specified time (snapshot file)</li> <li>R 6 pflotran shall output state variables at a specified location for over time (observation file)</li> <li>R 7 pflotran shall support unstructured grids defined by elements and vertices (implicit unstructured)</li> <li>R 8 pflotran shall support unstructured grids defined by cells [coordinates and volumes] and connectivity [distances and areas] (explicit unstructured)</li> <li>R 9 pflotran shall support neumann boundary conditions over a boundary region of a domain</li> <li>R 10 pflotran shall support serial and parallel execution</li> <li>R 11 pflotran shall support the checkpoint/restart (i.e., the ability to save and restart a simulation at any point in time)</li> <li>R 12 pflotran shall support zero flux boundary conditions over a boundary region of a domain</li> <li>R 13 pflotran shall support the ability to specify the initial state of primary dependent variables in the domain (initial condition)</li> <li>R 14 pflotran shall simulate variably saturated fluid flow</li> <li>R 15 pflotran shall support sources/sinks using a mass rate expression</li> <li>R 18 pflotran shall calculate liquid saturation using the van genuchten pressure-saturation relationship</li> <li>R 17 pflotran shall calculate liquid relative permeability using the van genuchten-mualem relationship</li> <li>R 18 pflotran shall simulate fluid flow in a heterogeneous porous medium</li> <li>R 19 pflotran shall support sources/sinks using a volumetric rate expression</li> <li>R 20 pflotran shall output state variable instantaneous and cumulative fluxes at cell faces over time (mass balance file)</li> <li>R 21 pflotran shall support heterogeneous porosity (material property)</li> <li>R 22 pflotran shall support heterogeneous intrinsic permeability (material property)</li> </ul>	<p><b>R 1 pflotran shall support hydrostatic dirichlet boundary conditions over a boundary region of a domain</b></p> <ul style="list-style-type: none"> <li>1D Hydrostatic</li> </ul> <p><b>R 2 pflotran shall support dirichlet boundary conditions over a boundary region of a domain</b></p> <ul style="list-style-type: none"> <li>1D Hydrostatic</li> <li>1D Transient Flow BC 1</li> <li>2D Transient Flow BC 1 and 2</li> <li>Variably Saturated Flow</li> <li>Heterogenous Material Properties</li> </ul> <p><b>R 3 pflotran shall support cartesian grids (structured)</b></p> <ul style="list-style-type: none"> <li>1D Hydrostatic</li> <li>1D Transient Flow BC 1</li> <li>1D Transient Flow BC 2</li> <li>1D Transient Flow BC 1 and 2</li> <li>2D Transient Flow BC 1 and 2</li> <li>Variably Saturated Flow</li> <li>Volumetric Source Sink</li> <li>Heterogenous Material Properties</li> </ul> <p><b>R 4 pflotran shall simulate single-phase fluid flow based on darcy's law</b></p> <ul style="list-style-type: none"> <li>1D Hydrostatic</li> <li>1D Transient Flow BC 1</li> <li>1D Transient Flow BC 2</li> <li>1D Transient Flow BC 1 and 2</li> <li>2D Transient Flow BC 1 and 2</li> <li>Variably Saturated Flow</li> <li>Volumetric Source Sink</li> <li>Heterogenous Material Properties</li> </ul> <p><b>R 5 pflotran shall output state variables for all grid cells at a specified time (snapshot file)</b></p> <ul style="list-style-type: none"> <li>1D Hydrostatic</li> <li>1D Transient Flow BC 2</li> <li>1D Transient Flow BC 1 and 2</li> <li>2D Transient Flow BC 1 and 2</li> <li>Variably Saturated Flow</li> </ul>

Figure 2.1-5 Screenshot of mapping requirements to the GDSA QA tests

### 2.1.2.1 Kolditz et al., 2015 Analytical QA Tests

The analytical tests from Kolditz et al., 2015 were expanded on from the existing test suite (Frederick, 2018). The analytical tests include steady state and transient flow problems in 1D, 2D, and 3D. (In Figure 2.1-5 only the transient solutions and steady state hydrostatic solution are shown). The four transient tests include boundary conditions of the first and second kind.

#### Test Case 1: 2D Transient Flow, Boundary Conditions of the First and Second Type

The analytical solution based on Kolditz et al., 2015 Section 2.2.10, is a 2D transient flow solution using boundary conditions of the first and second type. The domain is a 100x100x1 meter rectangular plane. The solution was calculated using two different grid cell sizes (2 m and 10 m) to display the capability of the QA-toolbox to test multiple grids based on user defined parameters (Figure 2.1-6). In this problem the pressure is initially distributed according to  $p(x,y,t=0) = f(x)f(y) + p_{offset}$ , where  $f(x)$  is defined as:

$$\begin{aligned}
 f(x) &= 0 & 0 \leq x \leq \frac{L}{10} \\
 f(x) &= \frac{10x}{3L} - \frac{1}{3} & \frac{L}{10} \leq x \leq \frac{4L}{10} \\
 f(x) &= 1 & \frac{4L}{10} \leq x \leq \frac{6L}{10} \\
 f(x) &= 3 - \frac{10x}{3L} & \frac{6L}{10} \leq x \leq \frac{9L}{10}
 \end{aligned}
 \tag{Equation 2.1-1}$$

$$f(x) = 0 \quad \frac{9L}{10} \leq x \leq L$$

and  $f(y)$  is defined as:

$$\begin{aligned} f(y) &= 0 & 0 \leq y \leq \frac{L}{10} & \text{Equation 2.1-2} \\ f(y) &= \frac{10y}{3L} - \frac{1}{3} & \frac{L}{10} \leq y \leq \frac{4L}{10} \\ f(y) &= 1 & \frac{4L}{10} \leq y \leq \frac{6L}{10} \\ f(y) &= 3 - \frac{10y}{3L} & \frac{6L}{10} \leq y \leq \frac{9L}{10} \\ f(y) &= 0 & \frac{9L}{10} \leq y \leq L \end{aligned}$$

At north and south boundaries, a no fluid flux condition is applied:

$$q(x, 0, t) = 0 \quad \text{Equation 2.1-3}$$

$$q(x, L, t) = 0 \quad \text{Equation 2.1-4}$$

At the east and west boundaries, a pressure boundary condition is applied:

$$p(0, y, t) = 0 \quad \text{Equation 2.1-5}$$

$$p(L, y, t) = 0 \quad \text{Equation 2.1-6}$$

where  $L = 100$  m and  $p_{offset} = 0.101235$  MPa. The transient pressure distribution is governed by:

$$\varphi K \frac{\partial p}{\partial t} = \frac{k}{\mu} \left( \frac{\partial^2 p}{\partial x^2} + \frac{\partial^2 p}{\partial y^2} \right) \quad \text{Equation 2.1-7}$$

where  $\varphi$  is porosity,  $K$  is fluid compressibility ( $\text{Pa}^{-1}$ ), and  $k$  is permeability ( $\text{m}^2$ ). With the initial pressure given, the analytical solution is:

$$p(x, y, t) = p_1(x, t)p_2(y, t) + p_{offset} \quad \text{Equation 2.1-8}$$

$$p_1(x, t) = \sum_{n=1}^{\infty} \exp\left(-\chi n^2 \pi^2 \frac{t}{L^2}\right) \left(\frac{80}{3(n\pi)^2}\right) \sin \frac{n\pi x}{L} \sin \frac{n\pi}{2} \sin \frac{n\pi}{4} \sin \frac{3n\pi}{20} \quad \text{Equation 2.1-9}$$

$$p_2(y, t) = \frac{1}{2} + \sum_{n=1}^{\infty} \exp\left(-\chi n^2 \pi^2 \frac{t}{L^2}\right) \left(\frac{80}{3(n\pi)^2}\right) \cos \frac{n\pi y}{L} \cos \frac{n\pi}{2} \sin \frac{n\pi}{4} \sin \frac{3n\pi}{20} \quad \text{Equation 2.1-10}$$

$$\chi = \frac{k}{\varphi \mu K} \quad \text{Equation 2.1-11}$$

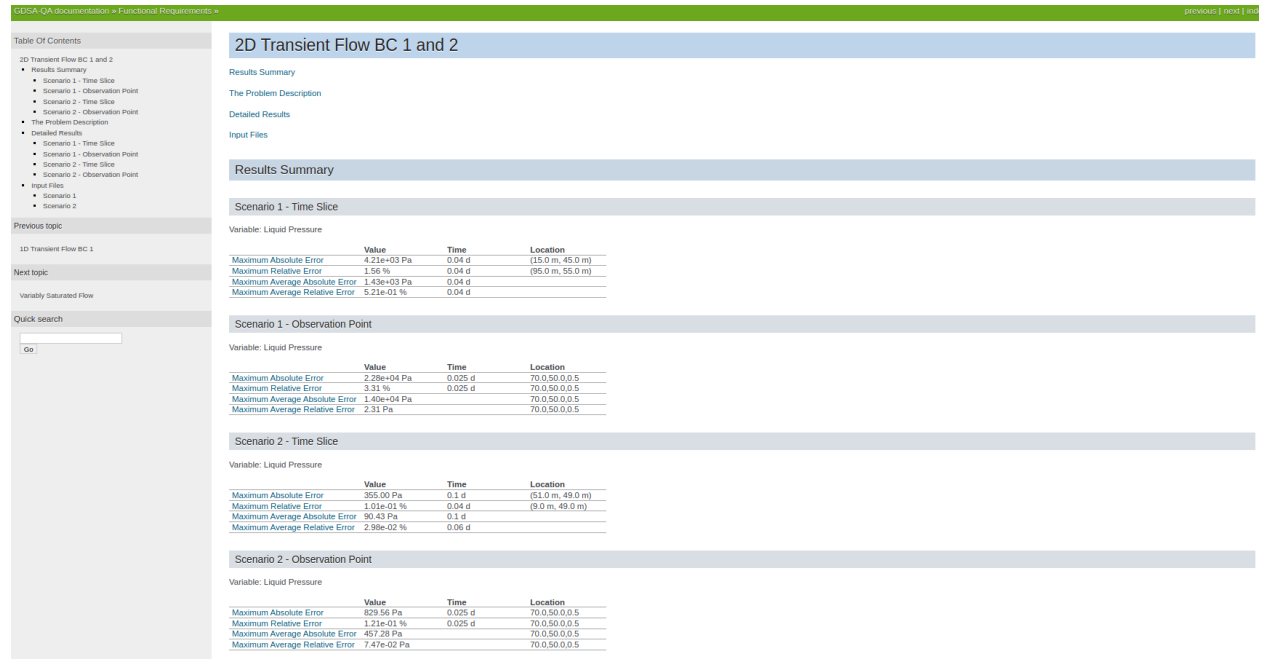


Figure 2.1-6 Screenshot of results summary where each scenario corresponds to different grid sizes. Scenario one uses cell spacing of 10 m and scenario two uses cell spacing of 2 m

**Test Case 2: 1D Transient Flow, Boundary Conditions of the First Type**

The 1D transient flow solution using first type boundary conditions based on Kolditz et al., 2015 Section 2.2.7 was expanded by comparing a structured, unstructured implicit, and unstructured explicit grid to satisfy R16 and R17 (Figure 2.1-7). The domain is a 20x1x1 meter rectangular column. The pressure is initially uniform at  $p(t=0) = 250000$  Pa. The boundary conditions are:

$$p(-L, t) = p_b t + p_{t=0} \tag{Equation 2.1-12}$$

$$p(L, t) = p_b t + p_{t=0} \tag{Equation 2.1-13}$$

where  $L = 10$  m and  $p_b = 200000$  Pa/day. The transient pressure distribution is governed by:

$$\varphi K \frac{\partial p}{\partial t} = \frac{k}{\mu} \left( \frac{\partial^2 p}{\partial x^2} \right) \tag{Equation 2.1-14}$$

With the given boundary conditions, the analytical solution is:

$$p(x, t) = p_b t + \frac{p_b(x^2 - L^2)}{2\chi} + \frac{16p_b L^2}{\chi \pi^3} \sum_{n=0}^{\infty} \frac{(-1)^n}{(2n+1)^3} \cos\left(\frac{(2n+1)x\pi}{2L}\right) e^{-\chi(2n+1)^2 \pi^2 \frac{t}{4L^2}} \tag{Equation 2.1-15}$$

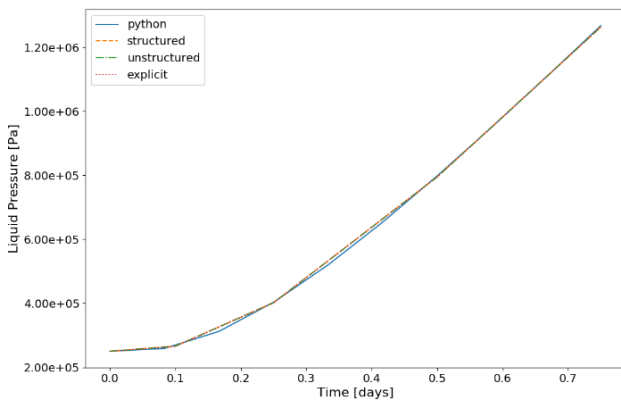
Detailed Results

Scenario 1 - Observation Point

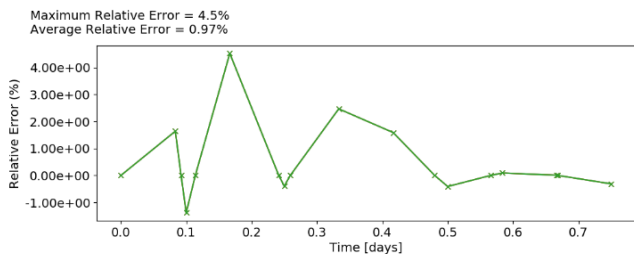
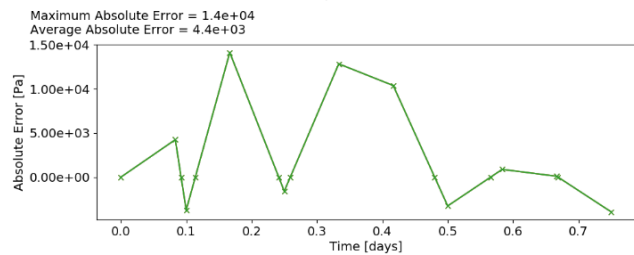
Comparison of Liquid Pressure at 1.0, 0.5, 0.5 for Scenario 1 - Observation Point: python vs structured vs unstructured vs explicit

Average Absolute Error = 4361.815066315217 Pa  
 Average Relative Error = 0.9715112180862497 %  
 Maximum Absolute Error = 14117.639686292172 Pa  
 Maximum Relative Error = 4.521336551037961 %  
 Time of Maximum Absolute Error = 0.16666666666666666 day  
 Time of Maximum Relative Error = 0.16666666666666666 day

1D Transient Flow: Liquid Pressure 1.0, 0.5, 0.5



Liquid Pressure



Input Files

Scenario 1

- The python input file can be downloaded [here](#)
- The structured input file can be downloaded [here](#)
- The unstructured input file can be downloaded [here](#)
- The explicit input file can be downloaded [here](#)

Figure 2.1-7 Screenshot of HTML output of the detailed results at one observation point for the Kolditz et al., 2015 Section 2.2.7 test.

***Test Case 3: Expanded 1D Transient Flow, Boundary Conditions of the First and Second Kind***

To satisfy R6 (PFLOTRAN shall default to "no flow" boundary condition when no boundary condition is specified), the 1D transient flow solution using first and second boundary conditions based on Kolditz et al., 2015 Section 2.2.9 was expanded. The domain is a 100x1x1 meter rectangular beam. In this problem the pressure is initially distributed as Equation 2.1-12 - Equation 2.1-13, with a no fluid flux condition applied at the boundaries and the transient pressure distribution given by Equation 2.1-14 and the analytical solution given by Equation 2.1-15. In the original problem a Neumann flux of  $0 \text{ m s}^{-1}$  is applied at the two boundaries of the domain in the PFLOTRAN input deck. In this test the default "no flow" condition in PFLOTRAN is used by not specifying boundary conditions in the input deck. A screenshot of the test can be seen in Figure 2.1-8.



## Detailed Results

## Scenario 1 - Time Slice

Comparison of Liquid Pressure at 0.05 d for Scenario 1 - Time Slice: python vs zero\_flux  
vs neumann

Average Absolute Error = 214.79636831075587 Pa  
 Average Relative Error = 0.03928030421257642 %  
 Maximum Absolute Error = 580.8019332168042 Pa  
 Maximum Relative Error = 0.2043674177055365 %  
 Location of Maximum Absolute Error = 5.0 m  
 Location of Maximum Relative Error = 5.0 m

1D Transient Flow: Liquid Pressure @ 5.00e-02 d

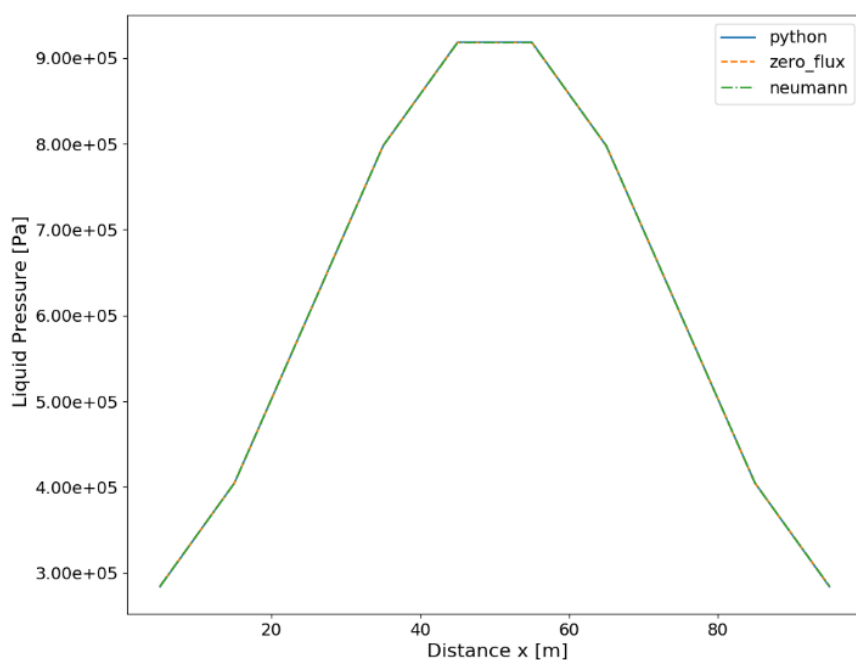


Figure 2.1-8 Screenshot of HTML output of the detailed results at a time slice for the Kolditz et al., 2015 Section 2.2.9 test with default no-flow boundaries.

#### *Test Case 4: 1D Transient flow, Boundary Condition of the Second Type*

The next analytical solution is a 1D transient flow analytical solution using boundary condition of the second type based on Kolditz et al., 2015 Section 2.2.8. The domain is a 25x1x1 meter rectangular column using 25 grid cells. Here the pressure is initially uniform at 0 MPa. At the left end a no fluid flux boundary condition is applied and at the right end a transient fluid flux of  $9.0 \times 10^{-6} t$  in  $\text{m s}^{-1}$  is applied. The transient pressure distribution is given by Equation 2.1-14 and the analytical solution is defined by:

$$p(x, t) = \frac{8q\sqrt{\chi t^3}}{k\mu} \sum_{n=0}^{\infty} \left[ i^3 \operatorname{erfc} \frac{(2n+1)L-x}{2\sqrt{\chi t}} + i^3 \operatorname{erfc} \frac{(2n+1)L+x}{2\sqrt{\chi t}} \right] \quad \text{Equation 2.1-16}$$

where  $i^3 \operatorname{erfc}(g)$  represents the third repeated integral of the complimentary error function given by:

$$i^3 \operatorname{erfc}(g) = \frac{2}{\pi} \int_g^{\infty} \frac{(s-g)^3}{3!} e^{-s^2} ds \quad \text{Equation 2.1-17}$$

To satisfy R22 and R18 (PFLOTTRAN shall be able to run in parallel and support restart and checkpoint files respectively) the test was expanded to run the solution in parallel. The new parallel capabilities in the QA-toolbox were utilized by specifying one input deck to run in parallel using 4 nodes, and another input deck was added to start from a restart file at 0.04 days in Figure 2.1-9.

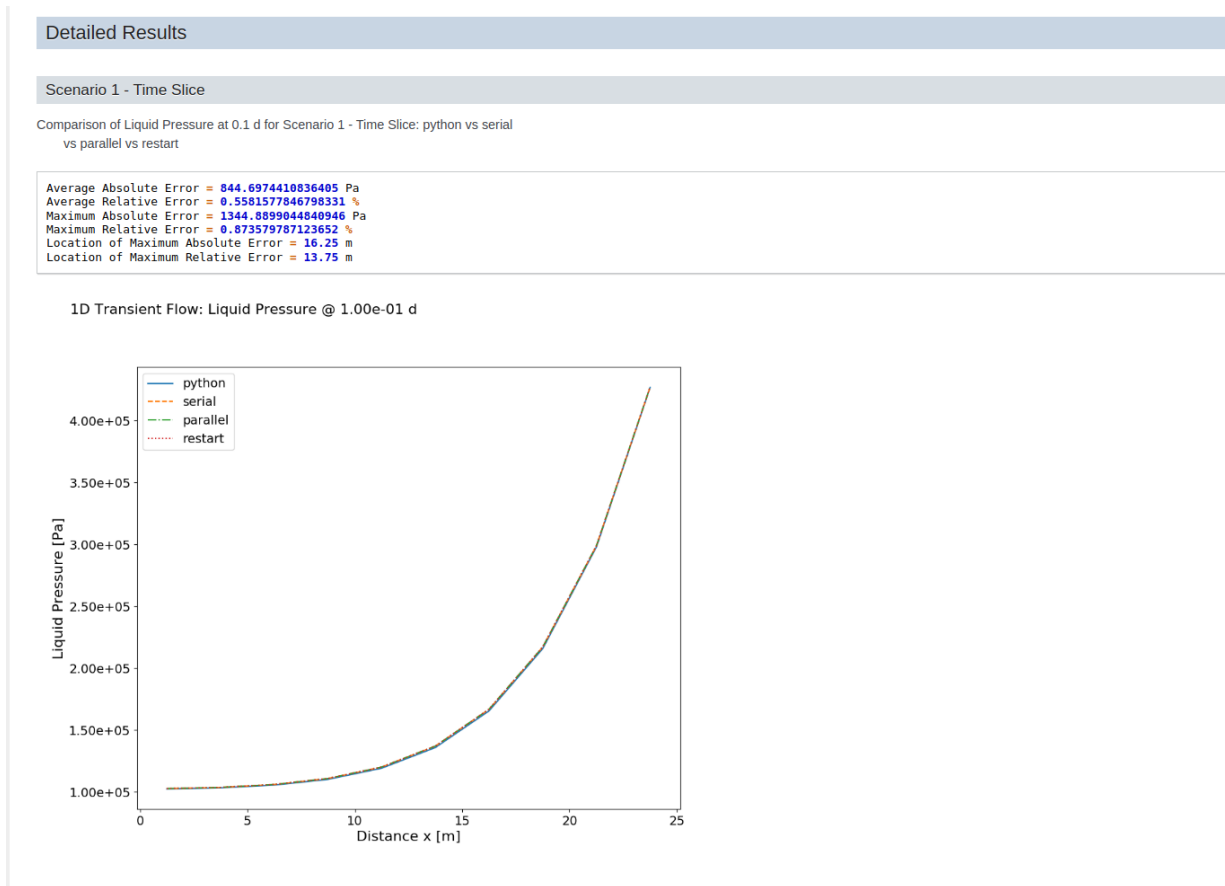


Figure 2.1-9 Screenshot of HTML output of the detailed results at a time slice for the Kolditz et al., 2015 Section 2.2.8 test ran in serial, parallel, and a restart file at 0.04 days.

### 2.1.2.2 TOUGH3 Variably Saturated Flow and Heterogeneous

In order to test variably saturated flow and heterogeneous permeability (R2 and R3) a comparison was done using the TOUGH3 simulator. The first example problem looking at variably saturated flow in a homogeneous media was taken from the TOUGH3 manual (Jung et al., 2018) sample problem 10.1. The

problem looks at a column 1 m in length with 20 cells which is initially saturated with liquid water. The level of water is then lowered to 0.7 m below the column and drained for 24 hours. Then an infiltration flux is applied at the top of the column for 1 hour and drained for 24 more hours. In TOUGH3 this requires running four different input files representing mesh generation, creation of the initial hydrostatic pressure profile, drainage of water, and the final infiltration and drainage. In the QA-toolbox the final input deck was run using the initial conditions from the third step (drainage of water after the level of water is lowered to 0.7 m) as input for both TOUGH3 and PFLOTTRAN. The equation for variably saturated flow using RICHARDS mode in PFLOTTRAN is given by:

$$\frac{\partial}{\partial t}(\varphi s \eta) + \nabla \cdot (\eta q) = Q_w \quad \text{Equation 2.1-18}$$

with the Darcy flux  $q$  [m s<sup>-1</sup>] defined as:

$$q = - \frac{k k_r(s)}{\mu} \nabla (P - \rho g z) \quad \text{Equation 2.1-19}$$

Where  $\varphi$  is porosity,  $s$  is saturation,  $\eta$  is molar density [kmol m<sup>-3</sup>],  $\rho$  is mass water density [kg m<sup>-3</sup>],  $k$  is intrinsic permeability [m<sup>2</sup>],  $k_r$  is relative permeability,  $\mu$  is viscosity [Pa s].  $P$  is pressure [Pa],  $g$  is gravity [m s<sup>-2</sup>], and  $Q_w$  is the source/sink term [kmol m<sup>-3</sup> s<sup>-1</sup>]. Liquid saturation was calculated using the van Genuchten pressure-saturation relationship (R11) and relative permeability was calculated using the van Genuchten-Mualem relationship (R12). The test also satisfied R8 by specifying a mass rate source/sink for the infiltration. The comparison can be seen in Figure 2.1-10 and Figure 2.1-11 of liquid saturation in the column.

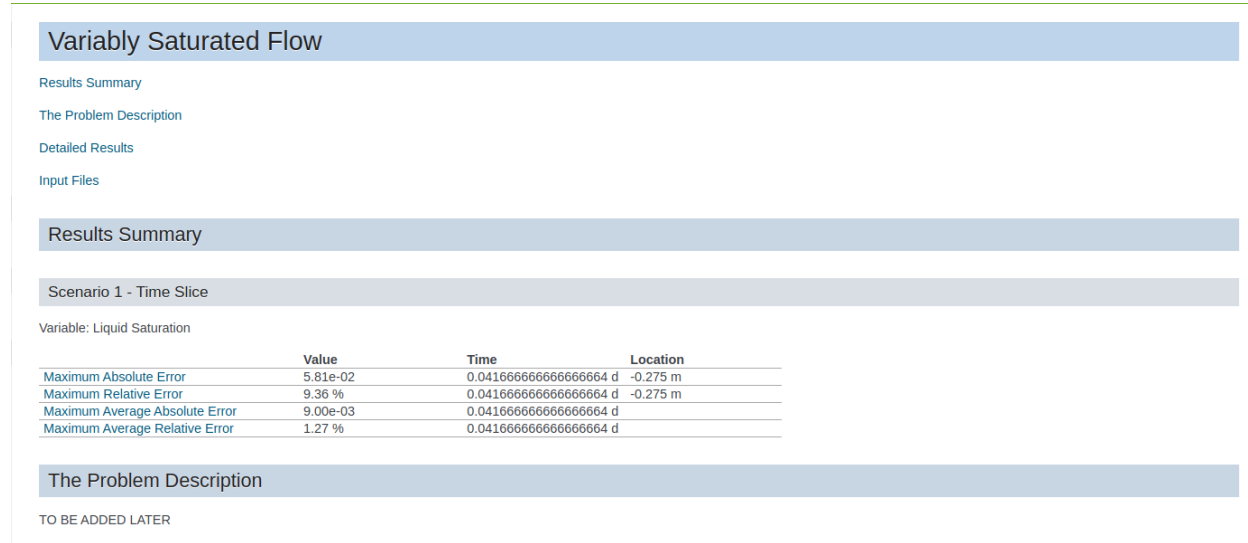


Figure 2.1-10 Results summary of the TOUGH3 vs PFLOTTRAN variably saturated flow test

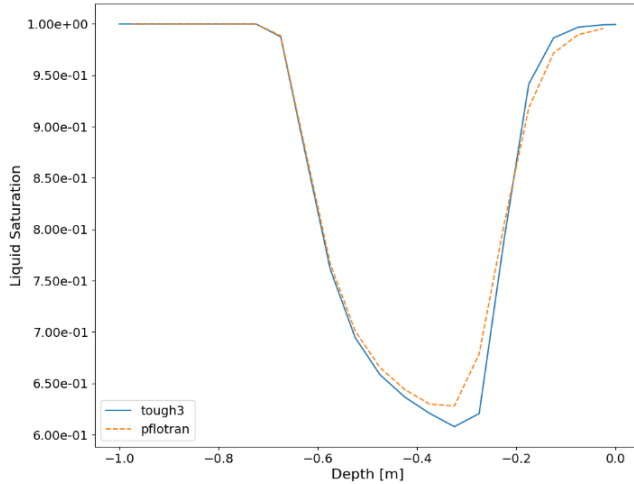
Detailed Results

Scenario 1 - Time Slice

Comparison of Liquid Saturation at 0.04166666666666664 d for Scenario 1 - Time Slice: tough3 vs pflotran

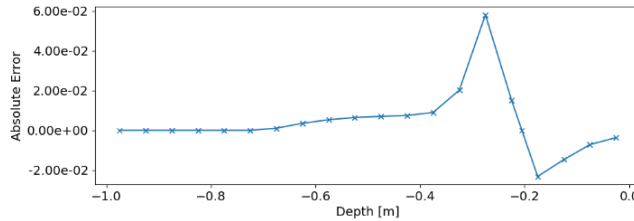
Average Absolute Error = 0.008995195268926665  
 Average Relative Error = 1.2735484893626292 %  
 Maximum Absolute Error = 0.0581213226562878  
 Maximum Relative Error = 9.364861872669035 %  
 Location of Maximum Absolute Error = -0.275 m  
 Location of Maximum Relative Error = -0.275 m

1D Variably Saturated Flow @ 4.17e-02 d

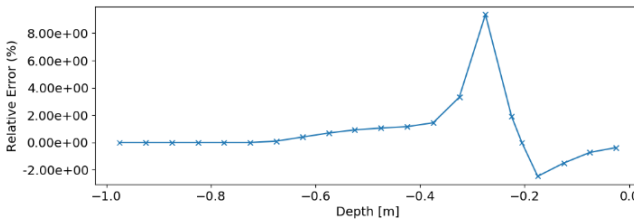


Liquid Saturation

Maximum Absolute Error = 0.058  
 Average Absolute Error = 0.009



Maximum Relative Error = 9.4%  
 Average Relative Error = 1.3%



Comparison of Liquid Saturation at 0.08333333333333333 d for Scenario 1 - Time Slice: tough3 vs pflotran

Average Absolute Error = 0.005103354367182883  
 Average Relative Error = 0.708567012038118 %  
 Maximum Absolute Error = 0.02626013417845685  
 Maximum Relative Error = 3.966444485574863 %  
 Location of Maximum Absolute Error = -0.425 m  
 Location of Maximum Relative Error = -0.425 m

Figure 2.1-11 Detailed results of the TOUGH3 vs PFLOTTRAN variably saturated flow test.

The example problem was then expanded to run in a heterogenous permeability and porosity field. Heterogenous permeability and porosity values were taken from a 1D slice of a heterogenous cube generated via the geostatistical software GSLIB. All parameters remained the same except for the heterogenous permeability and porosity values and the domain was changed to 16 cells in the 1 m column. The comparison can be seen in Figure 2.1-12. Future work will include matching up time stepping and other convergence assumptions made in the input files, which account for the small differences see in the results of Figure 2.1-11 and Figure 2.1-12.

Comparison of Liquid Saturation at 0.08333333333333333 d for Scenario 1 - Time Slice: tough3 vs pflotran

Average Absolute Error = 0.02046735651330466  
 Average Relative Error = 2.4862435289109195 %  
 Maximum Absolute Error = 0.10614929930990291  
 Maximum Relative Error = 11.806500870233677 %  
 Location of Maximum Absolute Error = -0.59375 m  
 Location of Maximum Relative Error = -0.59375 m

Heterogeneous material properties @ 8.33e-02 d

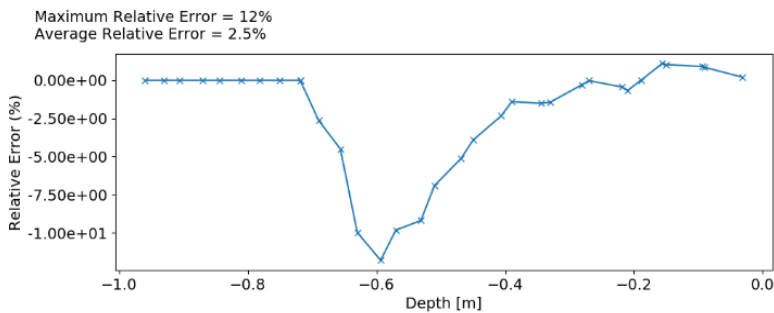
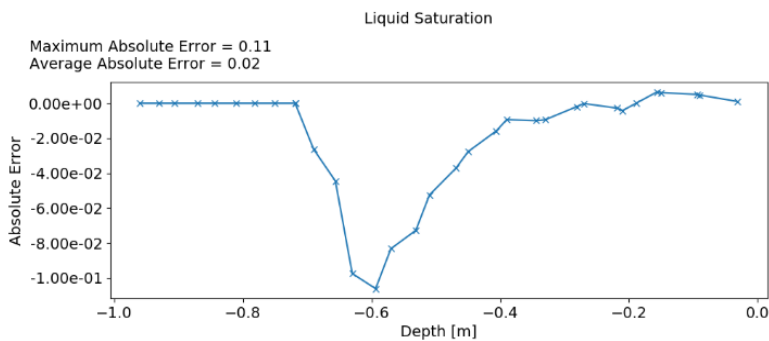
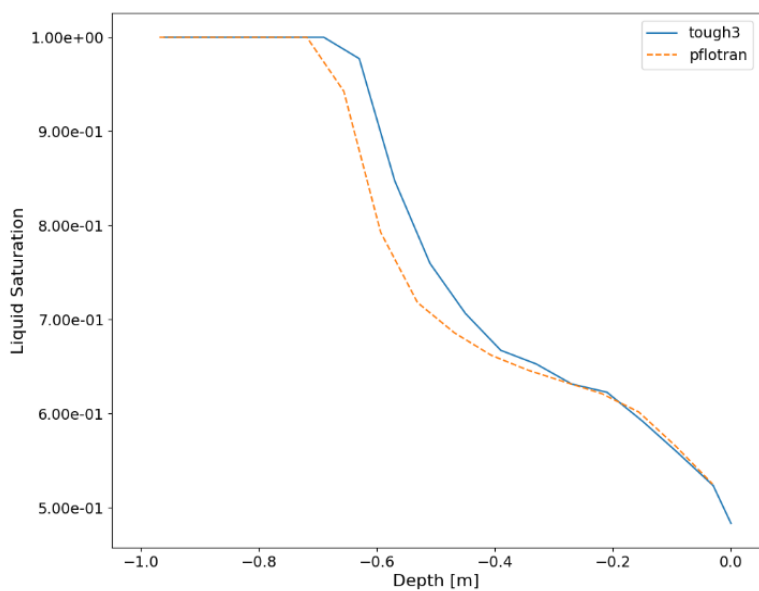


Figure 2.1-12 TOUGH3 vs PFLOTTRAN variably saturated flow test with heterogeneous permeability and porosity.

### 2.1.2.3 Volumetric Source Sink

The volumetric source sink test was created to satisfy R9 (PFLOTRAN shall support sources/sinks using a volumetric rate expression) as well as R21 (PFLOTRAN shall compare mass balance outputs). The later involved coding updates to the QA-toolbox to read mass balance file output from PFLOTRAN. In this test a volumetric injection and extraction rate of  $100 \text{ m}^3 \text{ d}^{-1}$  was specified at the left and right of a  $100 \times 1 \times 1 \text{ m}$  domain. A mass balance output was specified to get the mass (kg) of outflow water from the domain. Using a constant density of  $1000 \text{ m}^3 \text{ d}^{-1}$  the mass of water output per time at the outflow was calculated using Python and compared to the results from the mass balance file in PFLOTRAN (Figure 2.1-13).

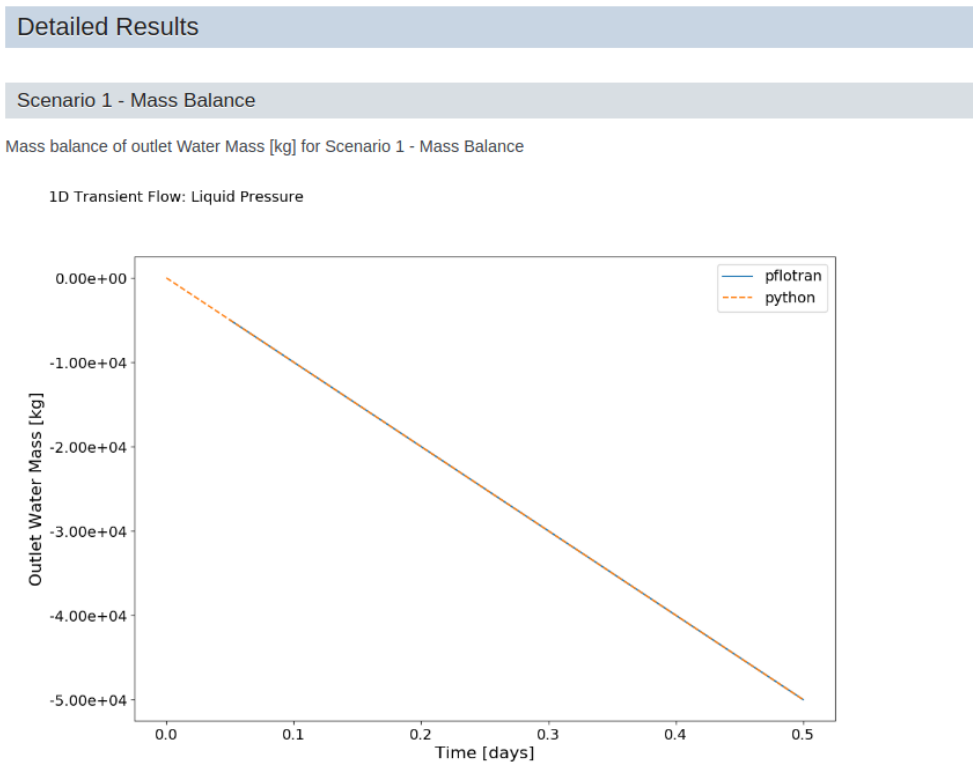


Figure 2.1-13 Volumetric source sink QA test looking at mass balance output. Mass is negative because it is flowing out of the domain.



## 2.2 Process Modeling

### 2.2.1 Material Transform Process Model

The material transform module was added to PFLOTRAN to provide a flexible and modular means to model transient material properties in a simulation domain as a function of available state variables. The module was designed as its own process model in the code, meaning it can make use of its own time-stepper if iterations are required to solve a given material transformation. The process model is sequentially coupled to other process models in PFLOTRAN as a “child” of the flow process model and a “peer” of the transport model, as shown in Figure 2.2-1. In PFLOTRAN, “peer” process models proceed independently and “children” sync with their “parent” at the timestep size of the parent.

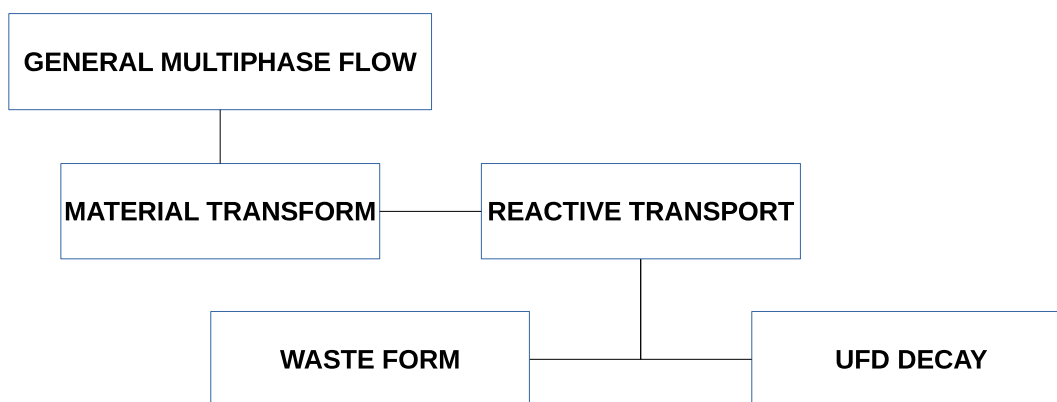


Figure 2.2-1 An example schematic showing process model coupling of the Material Transform module with multiphase flow, reactive transport, and UFD Decay.

#### 2.2.1.1 Overview

Recent developments in PFLOTRAN have been motivated by high temperature applications, such as post-closure criticality consequence assessment. This application requires improving the modeling fidelity of the dynamic thermal environment within and between waste form emplacements during transient thermal pulses that can be generated by significant power spikes. The mechanisms by which heat is generated and dissipated in a waste package by a steady-state criticality event may affect the flow of groundwater, radionuclide transport, near-field conditions, and waste package components.

In this context, the material transform process model has been developed to modify material properties and/or transport parameters during a simulation with specialized functions. This process model is intended to bypass more detailed and expensive calculations (such as with geomechanics or reactive transport) using a-priori surrogate models of physical phenomena. For example, if experimental data has been obtained for the effects of a mineral transition and generalized into a function of key PFLOTRAN variables such as temperature, pressure, etc., then a specialized model can be used to directly introduce modifications to system properties.

The first transformation introduced with this process model is called ILLITIZATION and describes the effects of the smectite-to-illite (S-I) transition in soils containing bentonite clay. This thermally driven process may affect flow and transport between multiple waste forms within a repository. Within this transformation class, models are available from two publications: with each implemented as an ILLITIZATION\_FUNCTION:

- DEFAULT: W-L Huang et al, 1993

- GENERAL: J. Cuadros and J. Linares, 1996

These time- and temperature-dependent models (which will be discussed in some detail) rely on the evolving fraction of smectite in the specified material relative to the initial quantity. Based on the relative change of smectite into illite, the user can specify two different effects:

- The components of the permeability tensor can be uniformly scaled based on a user-defined function. Use of this feature requires a flow mode to be active.
- The sorption distribution coefficients for specified elements can be scaled based on user-defined functions. Use of this feature requires transport to be active and for  $k_d$  values to be defined in the UFD Decay process model.

The second model for demonstration, BUFFER\_EROSION, has been tagged for future inclusion in the process model. While the model has not been incorporated in detail, the basic framework has been established to assist future development.

### 2.2.1.2 *Previous Work*

A preliminary demonstration of the concept was shown in Nole et al. (2021) and Price et al. (2022). In the previous phase of development, the illitization feature formed its own module in the same hierarchy as characteristic curves and thermal characteristic curves and thus featured keywords in the same section of the input deck (i.e., subsurface). The model was applied on a low-level within GENERAL, TH, and RICHARDS flow modes and had other unnecessary extensions into other parts of the code (such as the material module). Furthermore, unlike characteristic curves, not every simulation would need these optional models to be defined for the simulation to proceed.

Given the lack of extensibility and flexibility with this approach, the specific code implementing this feature was refactored into a general-use module for material transformations that could extend beyond the effects of illitization, with illitization being just one type of process that can affect material properties and transport parameters. Now, the material transform process model (pm\_material\_transform.F90) implements the high-level aspects while the material transform module (material\_transform.F90) contains the specific features of the models within each transformation class.

### 2.2.1.3 *Use of the Material Transform Module*

The material transform process model (PM) is activated in the SIMULATION block as shown in Table 2.2-1. The PM requires a flow mode to be active if permeability is modified and for transport (and UFD Decay) to be active if  $K_d$  changes are made. In the SUBSURFACE block, materials are listed, where at least one must have an active MATERIAL\_TRANSFORM. The material in the example, “bentonite,” has isotropic permeability of  $10^{-20}$  m<sup>2</sup> that is subject to modification by the transformation “mtf\_bentonite.” The activation and parameterization of permeability changes are specified within the material transform process model in a separate block.

Table 2.2-1 Definition of the material transform process model (“smectite-to-illite”) and a material (“bentonite”) with the PM active and isotropic permeability that will be modified.

```

===== simulation =====
SIMULATION
SIMULATION_TYPE SUBSURFACE
PROCESS_MODELS
...
  UFD_DECAY ufd_decay
/
  MATERIAL_TRANSFORM smectite-to-illite
/
/
END
===== subsurface =====
SUBSURFACE
...
MATERIAL_PROPERTY bentonite
  ID 1
...
MATERIAL_TRANSFORM mtf_bentonite
PERMEABILITY
  PERM_ISO 1.0d-20
/
/
...
END SUBSURFACE

```

In the UFD\_DECAY process model block (which is outside of the subsurface block), sorption distribution coefficients are listed for two elements Cs and Sr for the material “bentonite,” as shown in Table 2.2-2. These  $K_d$  values are subject to modification by “mtf\_bentonite.” The activation and parameterization of sorption changes are specified further down within the material transform process model.

Table 2.2-3 shows the MATERIAL\_TRANSFORM\_GENERAL process model block, which contains one material transform “mtf\_bentonite.” This block features one transformation class ILLITIZATION that uses the model from Huang *et al.*, 1993, which will be discussed in the next section. Any material with “mtf\_bentonite” active (just the material “bentonite” in this example) will have the permeability shifted by a linear function (via SHIFT\_PERM). The cesium  $K_d$  will also be shifted by a quadratic function and the strontium  $K_d$  will be shifted by an exponential function (via SHIFT\_KD). Within the PM block, model parameters are contained in the MATERIAL\_TRANSFORM sub-block to create material transform objects; the material transform objects are assigned to material properties in the MATERIAL block in subsurface. Auxiliary variables are allocated to ghosted cell ids if and only if the PM is active, and not all materials need to have a material transform object.

Table 2.2-2 The UFD Decay process model block showing  $K_d$  values of “bentonite” that can be modified by the material transform model.

```
# ===== pm ufd decay =====
UFD_DECAY
ELEMENT Sr
  SOLUBILITY 1.0d-11
  KD
  bentonite 1.0d+2 #kg water/m^3 bulk
  /
  /
ISOTOPE Sr90
  ELEMENT Sr
  DECAY_RATE 7.61d-10
  /
ELEMENT Cs
  SOLUBILITY 1.0d-11
  KD
  bentonite 1.0d+0 #kg water/m^3 bulk
  /
  /
ISOTOPE Cs137
  ELEMENT Cs
  DECAY_RATE 7.31d-10
  /
END # UFD_DECAY
```

Table 2.2-3 The material transform process model block with material transformation “mtf\_bentonite” that uses S-I model to modify permeability and  $K_d$  of Cs and Sr.

```
# ===== pm material transform =====
MATERIAL_TRANSFORM_GENERAL
MATERIAL_TRANSFORM mtf_bentonite
  ILLITIZATION # smectite-to-illite transformation
  ILLITIZATION_FUNCTION DEFAULT # Huang et al. 1993 model
  THRESHOLD_TEMPERATURE 2.00000d+1 C
  EA 1.17152d+5 J/mol
  FREQ 8.08000d+4 L/mol-s
  K_CONC 2.16000d-3 M
  SMECTITE_INITIAL 9.75000d-1
  # Permeability modified with linear function
  SHIFT_PERM LINEAR 1.50000d+3
  SHIFT_KD
  # Species must be present in UFD Decay block!
  # Quadratic and exponential functions modify kd
  Cs QUADRATIC -2.50000d-1 -2.50000d-1
  Sr EXPONENTIAL -6.94000d-1
  /
  / # ILLITIZATION_FUNCTION
  TEST # Print test file for function
  / # ILLITIZATION
  / # MATERIAL_TRANSFORM
END # MATERIAL_TRANSFORM_GENERAL
```

During execution, the process model does not print any additional information to the standard output, as there is currently no time-stepper involved. However, some key error messages include the following circumstances:

- The process model is active but no materials employ a material transform.
- Elements listed for sorption modification are duplicated or not available in UFD Decay.
- There are duplicate names among the specified material transform functions.
- A material transform was specified for a material that was not specified in the input deck.
- There are missing, bad, or non-applicable keywords in PM block, including bad function parameters.
- Permeability modification has been specified but no flow mode is active.
- Sorption modification has been specified but reactive transport is not active.

Three regression tests were developed to demonstrate the new smectite-to-illite model in three flow modes: GENERAL, TH, and RICHARDS. These tests also demonstrated use of the new SMECTITE output variable.

#### 2.2.1.4 *Smectite-to-Illite Transition*

In a repository where the waste package is surrounded by an EBS containing a buffer of bentonite, the EBS material provides an effective barrier to radionuclide transport because of low hydraulic conductivity and favorable swelling characteristics. Bentonite is comprised largely of the montmorillonite mineral of the smectite group, which has an articulated, laminar structure allowing for the adsorption of water and subsequent expansion. Thermodynamic equilibrium of the smectite can be affected by the silica reactivity and potassium concentration in the repository environment (Karnland and Birgersson 2006). A potassium cation ( $K^+$ ) can act as a counter-ion and affect the net-negative layer charge of the smectite. If quartz ( $SiO_2$ ) can precipitate (crystallize) in the presence of potassium, there is reduced water interaction and reduced swelling from the interlayer collapse in smectite as it transforms to illite. This loss of swelling capacity and plasticity from the smectite-to-illite (S-I) transition is susceptible to inducing volume shrinkage and increased permeability in the buffer. There is also a counteracting effect from increased radionuclide sorption on illite. This mineral transition is found to be correlated with temperature, so the transition can be driven by elevated waste package temperatures due to large decay heat or, e.g., during a criticality event.

PFLOTRAN has reactive transport modeling capabilities that could potentially be used to account for the reagents of the S-I transition, including quartz, potassium, sodium, etc. However, changes in soil physical properties corresponding to such mineral reactions have not been implemented. Rather than introduce physical changes in materials via the reactive transport side of the code, a reduced-order model can be formulated using state variables from the flow side to handle material property transformations (including the S-I transition) and remove dependence on chemical parameters.

In this new process model, the approach assumes that the S-I transition can be directly translated into a change in the original permeability and sorption characteristics. The scale of this change would have to be estimated a priori as part of the surrogate model. Furthermore, it must be assumed that the geochemical conditions needed for illitization are present either at time zero or when the threshold temperature is exceeded.

Alteration of the buffer permeability is considered part of an irreversible time- and temperature-dependent mineral transition. The rate of illitization is temperature-dependent and the reaction only takes

place when the temperature of a grid cell is above the user-specified threshold (which has a default of 0°C). The rate of illitization is used to determine the fractional increase in illite in the material for a given time step. In a sense, the surrogate model incorporates the effects of mineral phase transitions without detailed reactive transport calculations and without modifying the gridded domain despite the decrease in buffer swelling capacity. Use of the model will be expanded beyond the buffer region into the host rock, as the temperatures of the host rock can become elevated and susceptible to similar mineralogical changes affecting permeability and  $K_d$ .

### Huang et al., 1993

In the DEFAULT model, the time rate of change of smectite into illite is taken from the Huang et al. (1993) study and shown in Equation 2.2-1 for a given time step  $i+1$ .

$$-\left. \frac{df_S}{dt} \right|^{i+1} = \begin{cases} [K^+] \cdot (f_S^i)^2 \cdot A \exp\left(-\frac{E_a}{\mathcal{R} \cdot T^{i+1}}\right) & T^{i+1} \geq T_{th} \\ 0 & T^{i+1} < T_{th} \end{cases} \quad \text{Equation 2.2-1}$$

The equation is based on the potassium cation concentration  $[K^+]$  in mol/L and the previous smectite fraction  $f_S^i$ , where  $A$  is the frequency term in L/(mol-s),  $E_a$  is the activation energy in J/mol,  $\mathcal{R}$  is the ideal gas constant,  $T^{i+1}$  is the temperature in Kelvin of the grid cell, and  $T_{th}$  is the threshold temperature below which the reaction does not take place. The value of  $[K^+]$  is currently implemented as a constant and is not evaluated from reactive transport. The expression implies that at steady-state temperature, the rate of illitization is reduced as more smectite is replaced with illite.

By integrating Equation 2.2-1 over the time period, the smectite fraction is evaluated in Equation 2.2-2.

$$f_S^{i+1} = \frac{f_S^i}{1 - [K^+] \cdot A \exp\left(-\frac{E_a}{\mathcal{R} \cdot T^{i+1}}\right) \cdot (t^{i+1} - t^i) \cdot f_S^i} \quad \text{Equation 2.2-2}$$

The illite fraction is defined in Equation 2.2-3 as the complement of the smectite fraction. For this reason, the code only keeps track of  $f_S$  as a variable for checkpointing and output.

$$f_I^{i+1} = 1 - f_S^{i+1} \quad \text{Equation 2.2-3}$$

A scale factor  $F^{i+1}$  is defined that ranges from 0 to 1. It is based on the relative change in the fraction of illite, as shown in Equation 2.2-4. This is used to modify the permeability and/or sorption based on a user-specified function.

$$F^{i+1} = \frac{f_I^{i+1} - f_I^0}{f_S^0} \quad \text{Equation 2.2-4}$$

### Cuadros and Linares, 1996

A more generalized model for the rate of illitization is provided by Cuadros and Linares, 1996, and is shown in Equation 2.2-5. In this expression, the potassium concentration is modified with the exponent  $m$  and the order for the smectite fraction is raised to order  $n$ . The rate constant  $k$  is also a temperature-dependent Arrhenius term.

$$-\left.\frac{df_S}{dt}\right|^{i+1} = \begin{cases} [K^+]^m \cdot (f_S^i)^n \cdot k(T) & T^{i+1} \geq T_{th} \\ 0 & T^{i+1} < T_{th} \end{cases} \quad \text{Equation 2.2-5}$$

Using the time step notation from earlier, the time-integrated value for the smectite fraction is shown for two solutions of  $n$  in Equation 2.2-6. When employing  $m = 1$  and  $n = 2$ , the solution for the Huang et al. (1993) is obtained, demonstrating that the Cuadros and Linares model is a generalization to arbitrary order. Therefore, including such an option will expand modeling fidelity and impart more realism to a simulation. It can also be convenient for fitting to on-site data for a given performance assessment.

$$f_S^{i+1} = \left\{ [K^+]^m \cdot k(T) \cdot (n-1)(t^{i+1} - t^i) + (f_S^i)^{1-n} \right\}^{1/1-n}, n > 1 \quad \text{Equation 2.2-6}$$

$$f_S^{i+1} = f_S^i \cdot \exp\{-k(T) \cdot [K^+]^m \cdot (t^{i+1} - t^i)\}, n = 1$$

### Material Property Modification

The change in each permeability component  $k_j^{i+1}$  at time step  $i+1$  as a result of illitization can be computed using any of the four functional forms in Table 2.2-4. The default function, LINEAR, is computed with Equation 2.2-7 using the proportional change in the smectite fraction and a shift factor  $C_{k,1}$  along with the original permeability tensor  $k_j^0$ . This equation suggests that when all the original smectite is transformed to illite, the permeability has been modified by a factor of  $1 + C_{k,1}$ . The original permeability is employed as opposed to a recursive solution to maintain the relevance of  $C_{k,1}$  if a simulation needs to be restarted. This reference permeability tensor is saved within the illitization auxiliary variable class before it is replaced with the checkpoint value saved in the material auxiliary variables. Also, given the intermittent nature of the function's temperature dependence (via the temperature threshold), Equation 2.2-7 ensures that the permeability does not change if the mineral fractions do not change over a given time step.

The QUADRATIC and EXPONENTIAL functions accommodate an additional parameter  $C_{k,2}$ . These functions, along with EXPONENTIAL, must behave monotonically and not result in negative values at 100% illite. QUADRATIC is especially prone to introducing parabolic behavior between 0 and 100% illite, which would be non-physical. Therefore, there are error messages to check the user-specified values of  $C_{k,1}$  and  $C_{k,2}$ . Nonetheless, the user may employ increasing or decreasing trends with these functions. The functions shown in Table 2.2-4 can likewise be employed for  $K_d$  instead of the permeability tensor.

**Table 2.2-4** The four functional forms available to modify permeability, these can also be used to modify  $K_d$  values.

Type	Equation	
LINEAR	$k_j^{i+1} = k_j^0 (1 + C_{k,1} \cdot F^{i+1})$	Equation 2.2-7
QUADRATIC	$k_j^{i+1} = k_j^0 [1 + C_{k,1} \cdot F^{i+1} + C_{k,2} \cdot (F^{i+1})^2]$	Equation 2.2-8
POWER	$k_j^{i+1} = k_j^0 [1 + C_{k,1} \cdot (F^{i+1})^{C_{k,2}}]$	Equation 2.2-9
EXPONENTIAL	$k_j^{i+1} = k_j^0 \exp(C_{k,1} \cdot F^{i+1})$	Equation 2.2-10

### 2.2.1.5 Verification

The smectite-to-illite transformation was tested in a 1-D sample problem using RICHARDS mode at 260°C for one region with the process model active. Although RICHARDS mode is isothermal and the S-I functions are temperature-dependent, use of RICHARDS mode provides convenience in implementing a constant reference temperature. Results for smectite fraction, modified permeability, and modified Cesium  $K_d$  from PFLOTTRAN were then compared with analytical solutions for the two available models from Huang et al. (1993) and Cuadros and Linares (1996).

The 1-D problem is shown in Figure 2.1-5 where the gridded domain contains one cell with the S-I transformation active. All other cells do not initialize the smectite fraction although they appear as having zero smectite. The models are compared using the parameter sets shown in Table 2.2-5. These parameters were chosen as representative of the original literature. The potassium concentration is representative of Opalinus clay. The threshold temperature is clearly kept below the reference temperature to allow for continuous evaluation. If the temperature was evolving and dropped below the threshold, this would present difficulties for the analytical solution, as the rate would change to zero and the initial conditions would change for the next instance of a nonzero rate.



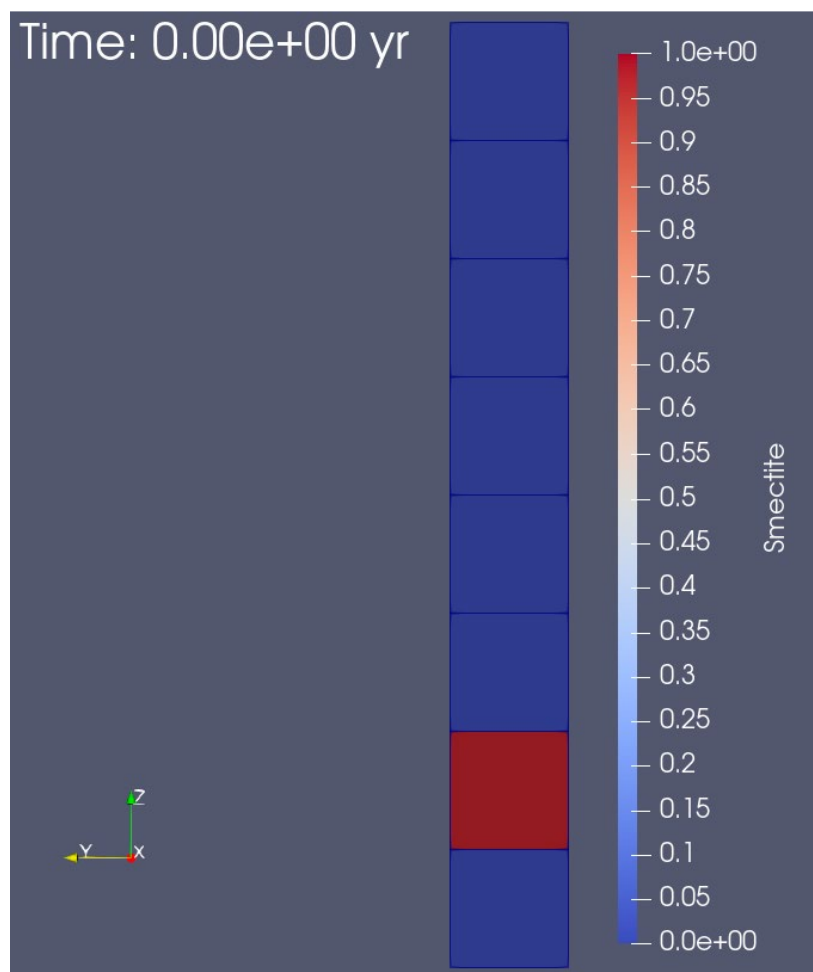


**Figure 2.2-2: View of 1-D verification problem domain with coloring for new smectite fraction output variable active in one grid cell with the material transform process model active.**

For each model, the parameters and governing equations were applied in the *NDSolve* function of Mathematica and then plotted over the same maximum time period as the PFLOTRAN simulation. The results of the isothermal test problem and the corresponding results from *NDSolve* are shown for smectite fraction (Figure 2.2-3), permeability (Figure 2.2-4) and the sorption distribution coefficient of cesium (Figure 2.2-5). The PFLOTRAN results very closely matched the analytical solutions computed in Mathematica for the smectite fraction and corresponding permeability and Cesium  $K_d$  modifications, where the percent differences are shown in Table 2.2-6. The machine precision of Mathematica is about 16 digits while PFLOTRAN results were output in plain text with 11-digit precision from the original double precision floating point value. Overall, for the Huang et al. (1993) model (#1), the smectite fraction from PFLOTRAN did not exceed 0.00098% relative difference from the analytical solution, while permeability was within 0.0022% and  $K_d^{Cs}$  within 0.012%. For the Cuadros and Linares (1996) model (#2), the smectite fraction from PFLOTRAN did not exceed 0.00023% relative difference, while the permeability was within 0.0024% and  $K_d^{Cs}$  within 0.0049%. As the smectite fraction decreased over time from heating, the permeability increased, and the cesium  $K_d$  decreased as specified.

Table 2.2-5 Parameters used for the two S-I models in the verification test

Parameter	Value	Unit	Model
Activation energy – $E_A$	1.17152E+5	J/mol	1 & 2
Frequency factor – $A$	8.08000E+4	L/mol-s	1 & 2
Potassium cation concentration – $[K^+]$	2.16000E-3	mol/L	1 & 2
Initial smectite fraction – $f_s^0$	97.5%	-	1 & 2
$[K^+]$ exponent – $m$	0.25	-	2
Smectite fraction exponent – $n$	5	-	2
Shift Permeability LINEAR $C_{k,1}$	999.0	-	1 & 2
Shift $K_d^{Cs}$ QUADRATIC $C_{k,1}$	-0.25	-	1 & 2
Shift $K_d^{Cs}$ QUADRATIC $C_{k,2}$	-0.25	-	1 & 2

Table 2.2-6 Maximum and median relative differences (in percent) in the parameters of interest between the PFLOTRAN output and the analytical solution.

Parameter	Max. Relative Difference		Median Relative Difference	
	Model 1	Model 2	Model 1	Model 2
Smectite fraction – $f_s$	0.00098%	0.00023%	0.00091%	0.00022%
Permeability $x$ -direction – $k_x$	0.00216%	0.00242%	0.00001%	0.00002%
Cs sorption distribution coefficient – $K_d^{Cs}$	0.01207%	0.00485%	0.00102%	0.00160%

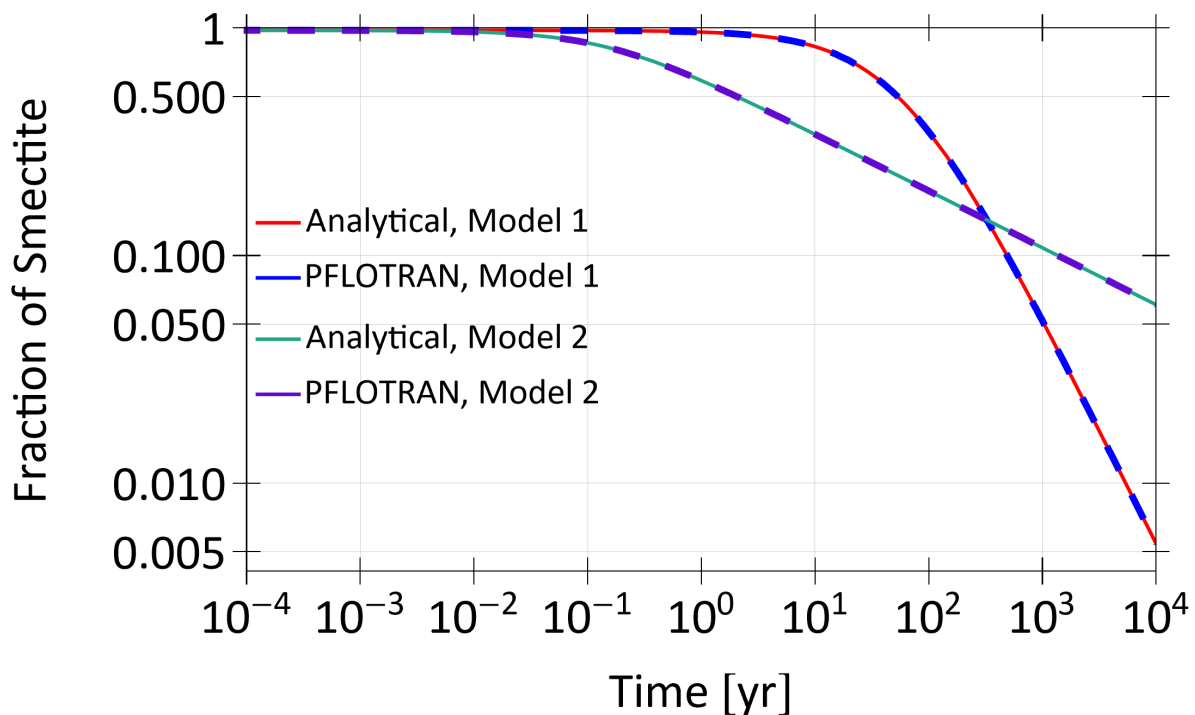


Figure 2.2-3: PFLOTRAN smectite fraction as a function of time ( $\log_{10}$  scale) for both S-I models compared to analytical solutions.

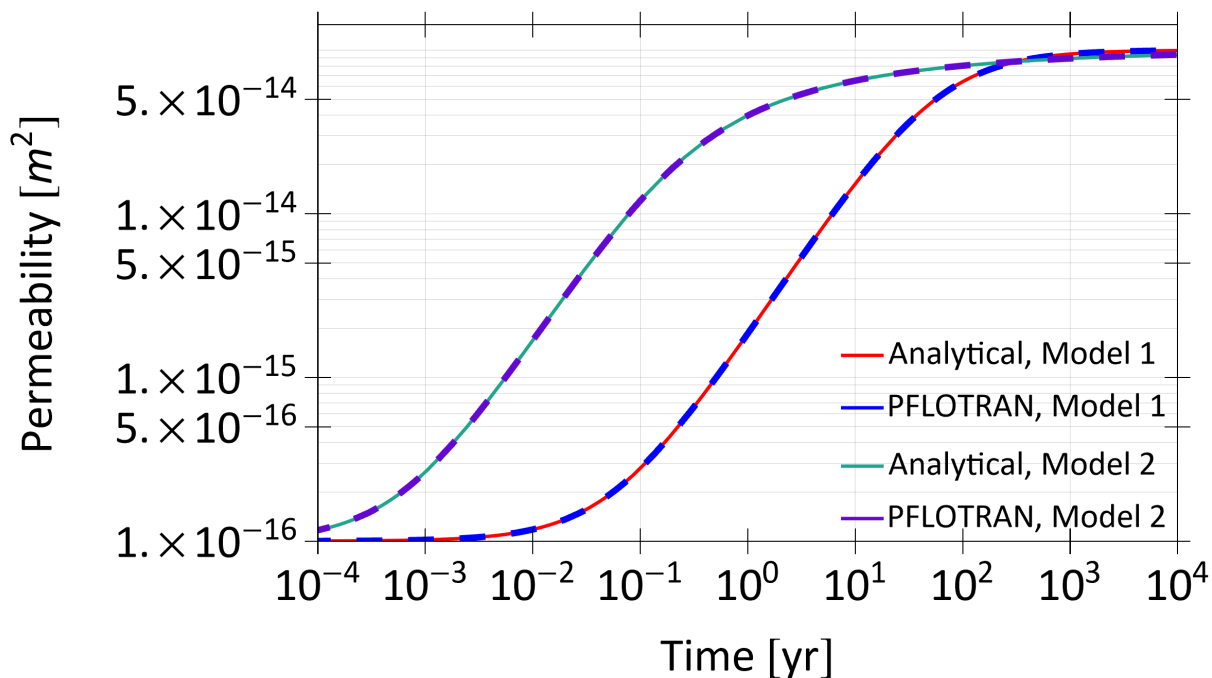


Figure 2.2-4: Shift in permeability as a function of time ( $\log_{10}$  scale) from both S-I models compared to analytical solutions.

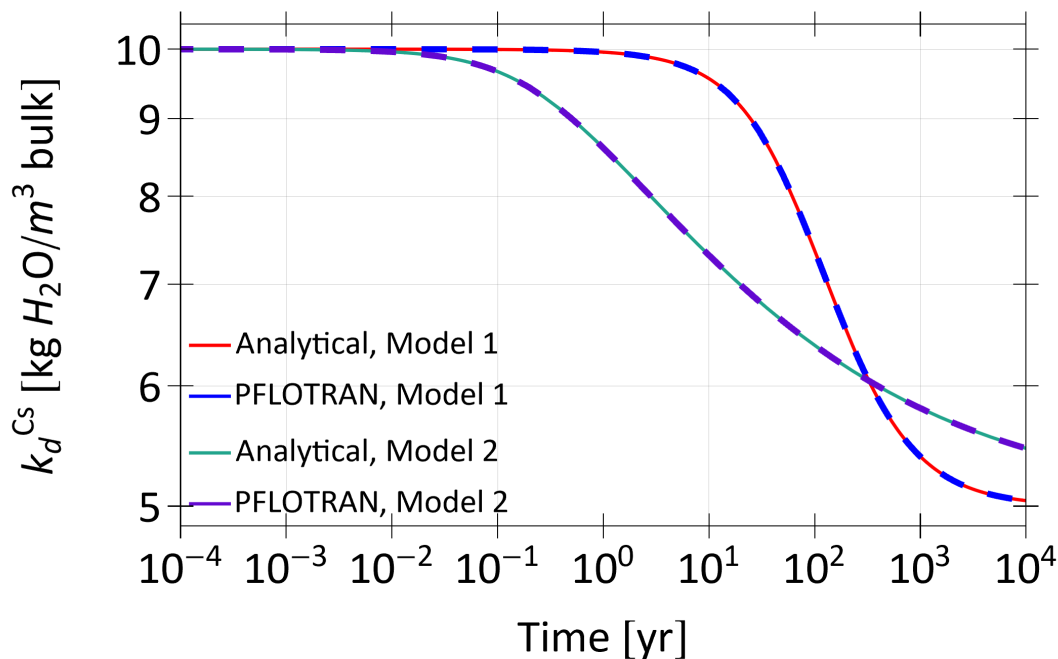


Figure 2.2-5: Shift in cesium  $K_d$  as a function of time ( $\log_{10}$  scale) from both S-I models compared to analytical solutions.

## 2.2.2 3D Lookup Table Interpolation

### 2.2.2.1 Overview

Evaluation of the radionuclide inventory during a criticality event was previously implemented as a 1-D interpolation of a lookup table (LUT) obtained from a single set of depletion results. This restricted the simulation to a set start time and power output for the criticality event.

3-D interpolation has now been added to the LUT capability of PFLOTRAN. Interpolation is available via two methods:

1. LookupTableInterpolate3DLP: Lagrange polynomials (the default) as applied to three axes
2. LookupTableInterpolate3DTrilinear: the trilinear method, which is an extension of linear interpolation in three dimensions.

Neither model is recommended for extrapolation, and the polynomial method is especially unstable in that regard. The first demonstration is a parameterized radionuclide inventory from criticality, but this is a general-purpose feature available for other 3-D data applications.

### 2.2.2.2 Application to Criticality Studies

Multiple sets of depletion results based on different criticality start times and power outputs can now be combined in a single lookup table for 3-D interpolation. This means that the simulation is no longer restricted to a single start time and power level, which allows for uncertainty quantification through continuous sampling of those parameters. Development has introduced an EXPANDED\_DATASET option for evaluating the criticality inventory in a waste form. This development allows for 3-D interpolation of data (e.g., mass fractions) based on two pivot variables (e.g., the criticality start time and power) and an array of independent variables (e.g., the real time). The previous ASCII lookup interface provided by DATASET was limited to 1-D interpolation in time.

Inventory results under certain conditions of steady-state criticality have been provided by ORNL from UNF-ST&DARDS for the MPC-32-162 and MPC-89-W047 canisters. These inventories were post-processed with Perl into a convenient text-based format for PFLOTRAN. Currently, the data cannot be implemented in the HDF5 format because criticality results provide jagged arrays, or multidimensional arrays with constituent vectors of different lengths (i.e., a sparse matrix). These jagged arrays required the development of special data structures.

The ORNL data has the following characteristics:

- 11 criticality start times ranging from 0 to  $5 \times 10^5$  y
- 0, 1, 2, and 4 kW criticality power outputs
- Logarithmic real time points for evaluation
- 28 radionuclides: several actinides + key fission products

An example inventory is plotted in Figure 2.2-6, where the criticality event starts at 500 years and introduces a jump in radionuclide fractions that were previously decaying. Given this discontinuous behavior from criticality, interpolating between two event start times may not be smooth. Special considerations for the DPC Criticality project include the following:

- The real time arrays are not the same size since criticality ceases at a different moment for every given start time and power. Therefore, the real times (and data) can be partitioned under the assumption each set is monotonically increasing.

- Inventories for each nuclide in the waste form can be listed in the data file in blocks with keyword INVENTORY in the order they appear in SPECIES in MECHANISM
- Since duplicate entries for the pivot and independent variables can introduce interpolation discontinuities, an error message appears if duplicates are detected in the lists.
- Other error messages exist for missing/bad information in the data file.

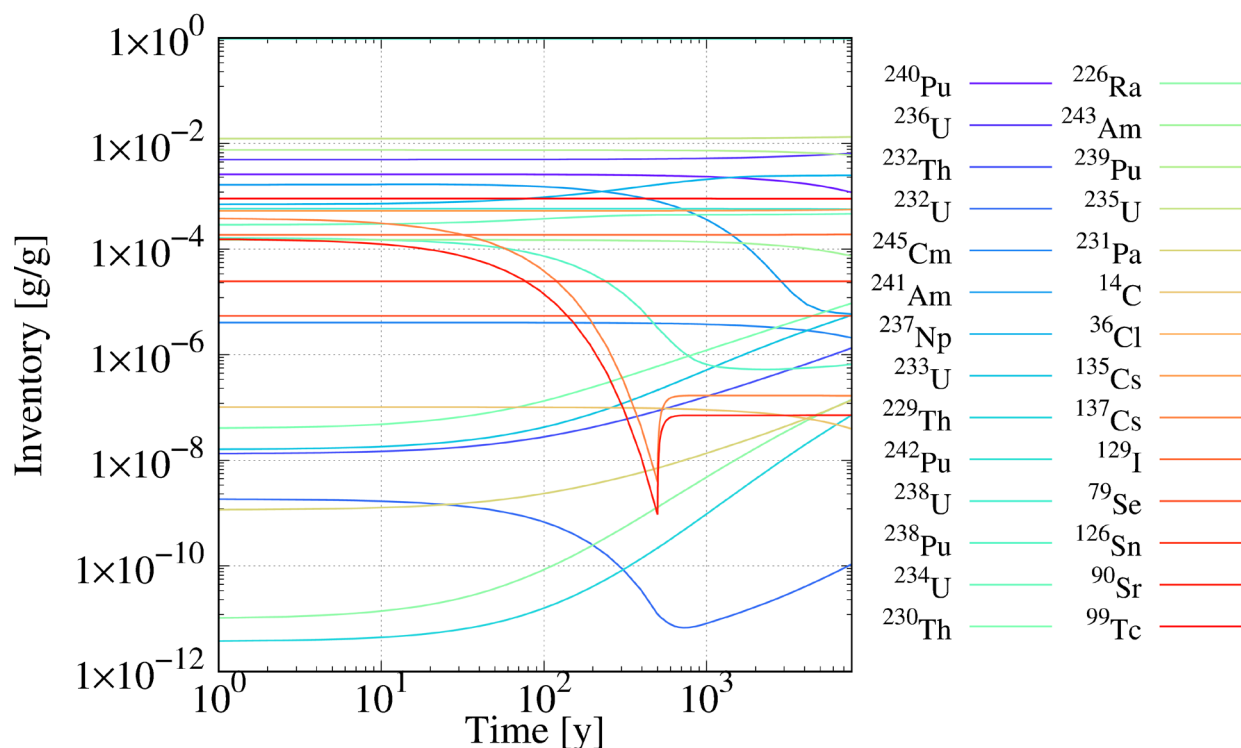


Figure 2.2-6: Radionuclide mass fractions for MPC-32-162 with a criticality event at P = 4 kW,  $t_0 = 500$  y.

### 2.2.2.3 Use of 3D Lookup Tables

Radionuclide inventories in the LUT are activated by the waste form process model in PFLOTRAN. Table 2.2-7 shows the waste form process model block, which features the waste form mechanism “mech\_01.” This MECHANISM includes two radionuclides Pu-240 and Tc-99 in the SPECIES list and is assigned to a waste form that utilizes criticality mechanism “crit\_01.”

In CRITICALITY\_MECH, the criticality start time, end time, and heat of criticality are defined. The inventory is defined with an EXPANDED\_DATASET. This option allows for the specification of an expanded inventory lookup table that can be interpolated in three dimensions for a given criticality start time (CRIT\_START), criticality power output (HEAT\_OF\_CRITICALITY), and a given time during the simulation. While the criticality start time defines an instance in time, the simulation time is the continuous time employed during the simulation. These values are used to interpolate a data matrix where the start time and power are pivot variables and the simulation time is the independent variable.

Table 2.2-7 The waste form process model showing two active radionuclides for use in the 3-D LUT.

```

# ===== pm waste form =====
WASTE_FORM_GENERAL
MECHANISM DSNF
NAME mech_01
MATRIX_DENSITY 3.70d+3 kg/m^3
SPECIES
# name MW[g/mol] dcy[1/s] initMF instRF daughter
Pu-240 240.05d+0 3.34d-12 2.84d-6 0.2d+0
Tc-99 98.91d+0 1.04d-13 8.87d-6 0.0d+0
/
CANISTER_DEGRADATION_MODEL
CANISTER_MATERIAL_CONSTANT 1500
/
/
WASTE_FORM
COORDINATE 1.00d+0 1.00d+0 5.00d-1
EXPOSURE_FACTOR 1.00d+1
VOLUME 1.14d+0 m^3
CANISTER_VITALITY_RATE 2.00d-3 1/day
MECHANISM_NAME mech_01
CRITICALITY_MECHANISM_NAME crit_01
/
...
CRITICALITY_MECH
NAME crit_01
CRIT_START 1.00d+1 d
CRIT_END 4.00d+2 d
HEAT OF CRITICALITY
CONSTANT_POWER 1.00d-7 MW
/
DECAY_HEAT TOTAL
DATASET ./decay_heat.txt
/
INVENTORY
EXPANDED_DATASET crit_inv.txt
OPTION
# extrapolation gives error message w/o option given
USE_LOOKUP_AND_IMPLICIT # decay w/ no extrapolation
# USE_LOOKUP_AND_EXTRAPOLATION # allow extrapolation
USE_LOOKUP_AFTER_CRITICALITY # use LUT after CRIT_END
/
/
END WASTE FORM GENERAL

```

The data table used by the criticality mechanism is labeled “crit\_inv.txt.” Table 2.2-8 shows a portion of this data table, which is simulated from the Bateman equations employed in *NDSolve* in Mathematica and not based on canister data. Here, the `START_TIME` block (the first pivot variable) has a multiplicity of 2x for the two criticality events beginning at 0 days and 120 days. The `POWER` block (the second pivot variable) has a multiplicity of 2x for the power levels of zero watts (decay-only) and 1 W. For the `REAL_TIME` block, which provides the independent variables, there are  $2 \times 2 = 4$  monotonically increasing arrays. Each `INVENTORY` block has an entry for each `REAL_TIME` value. The labels used for `INVENTORY` must match the labels used previously in `SPECIES`. The `INVENTORY` blocks can be listed in any order, and not all radionuclides in the table need to be used (i.e., in the `SPECIES` list).

**Table 2.2-8** Portions of the criticality inventory lookup table “crit\_inv.txt” showing two active radionuclides and an additional radionuclide not employed in the simulation.

```

TIME_UNITS d
POWER_UNITS kW
START_TIME
0.000000e+00 1.200000e+02
POWER
0.000000e+00 1.000000e-03
REAL_TIME
0.000000e+00 5.000000e+01 1.000000e+02 1.500000e+02 2.000000e+02 2.500000e+02 3.000000e+02 ... \
0.000000e+00 3.500000e+01 7.000000e+01 1.050000e+02 1.400000e+02 1.750000e+02 2.100000e+02 ... \
0.000000e+00 5.500000e+01 1.100000e+02 1.650000e+02 2.200000e+02 2.750000e+02 3.300000e+02 ... \
0.000000e+00 2.500000e+01 5.000000e+01 7.500000e+01 1.000000e+02 1.200000e+02 1.600000e+02 ...
INVENTORY Tc-99
8.870000e-06 8.869996e-06 8.869992e-06 8.869988e-06 8.869984e-06 8.869980e-06 8.869976e-06 ... \
8.870000e-06 9.021197e-06 9.172394e-06 9.323591e-06 9.474788e-06 9.625985e-06 9.777182e-06 ... \
8.870000e-06 8.869996e-06 8.869991e-06 8.869987e-06 8.869982e-06 8.869978e-06 8.869974e-06 ... \
8.870000e-06 8.869998e-06 8.869996e-06 8.869994e-06 8.869992e-06 8.869990e-06 9.042787e-06 ...
INVENTORY Pu-240
2.840000e-06 2.839959e-06 2.839918e-06 2.839877e-06 2.839836e-06 2.839795e-06 2.839754e-06 ... \
2.840000e-06 2.991171e-06 3.142340e-06 3.293507e-06 3.444673e-06 3.595837e-06 3.747000e-06 ... \
2.840000e-06 2.839955e-06 2.839910e-06 2.839865e-06 2.839820e-06 2.839775e-06 2.839730e-06 ... \
2.840000e-06 2.839980e-06 2.839959e-06 2.839939e-06 2.839918e-06 2.839902e-06 3.012668e-06 ...
INVENTORY U-236
0.000000e+00 4.097750e-11 8.195440e-11 1.229307e-10 1.639064e-10 2.048816e-10 2.458561e-10 ... \
0.000000e+00 2.868431e-11 5.736833e-11 8.605206e-11 1.147355e-10 1.434186e-10 1.721015e-10 ... \
0.000000e+00 4.507521e-11 9.014971e-11 1.352235e-10 1.802966e-10 2.253689e-10 2.704405e-10 ... \
0.000000e+00 2.048882e-11 4.097750e-11 6.146602e-11 8.195440e-11 9.834500e-11 1.311259e-10 ...

```

Options are introduced to handle the interface between the lookup table and the implicit solution:

- `USE_LOOKUP_AND_IMPLICIT`: resorts to the implicit solution (i.e., decay only with no external sources) when PFLOTRAN attempts to extrapolate beyond maximum time in table. A warning message is given when this occurs during the simulation.
- `USE_LOOKUP_AND_EXTRAPOLATION`: the interpolation subroutines are also used under extrapolation conditions (not recommended).

- `USE_LOOKUP_AFTER_CRITICALITY`: the lookup table is used after the criticality event end time (as opposed to the implicit solution).
- `None`: Error message when PFLOTRAN attempts to extrapolate beyond maximum time in table

#### **2.2.2.4**     *Continuing Work*

The new inventory lookup tables will be employed in a near-field simulation with a DPC containing PWR or BWR spent nuclear fuel. Uncertainty quantification may be performed involving the sampling of criticality start times and power outputs.



### 2.2.3 Multi-continuum

Matrix diffusion coupled with sorption is currently considered one of the most important radionuclide retardation mechanisms in fractured crystalline host rock (SKBF, 1983). One way of modeling diffusive transport between a rock matrix and fractures is by representing the phenomenon as a Fickian diffusion process over a dual porosity (dual continuum) system. The multiple continuum model in PFLOTRAN models a secondary continuum (matrix) coupled to the primary continuum (fracture) modeled as a disconnected one-dimensional domain which is referred to as the DCDM (Dual Continuum Disconnected Matrix) model (Lichtner, 2000). Advection and diffusion are allowed in the primary continuum, and in the secondary continuum transport occurs through diffusion only. The secondary continuum is modeled as a one-dimensional domain where diffusive fluxes occur perpendicular to the fracture wall. Each primary continuum cell has a corresponding set of secondary continuum cells attached to it. The secondary cells cannot interact with secondary cells associated with other primary cells. The equations for the primary and secondary continuum are solved separately and coupled together by a mass exchange flux assuming symmetry along the axis dividing them (Iraola et al., 2019).

The multiple continuum model in PFLOTRAN has undergone several developments in the last year. General maintenance was performed which involved bug fixes, improving error messaging and checking of parameters specified in the input deck, and improvements of the log grid spacing functionality. In addition, larger changes were made including adding multiple continuum functionality to the UFD decay process model and adding in functionality to model gas diffusion.

#### 2.2.3.1 General Maintenance

To improve user functionality of the multiple continuum model and to avoid code crashes, an extensive error messaging system was implemented in the multicontinuum process model. The first change forces the user to specify the geometry type of the secondary continuum first in the input block to check that all properties for the geometry are correctly defined. The multiple continuum geometry is described by the parameters: fracture spacing ( $f$ ), matrix block size ( $d$ ), half-fracture aperture ( $\delta$ ), and fracture volume fraction ( $\varepsilon$ ). These values can be seen in Figure 2.2-7 and Figure 2.2-8 describing the slab and nested cubes geometry, where  $\varepsilon = \delta/(\delta+L)$ . These parameters are not all independent: choosing any two allows the remaining two to be determined. There are six possible combinations to specify:  $\{f, d\}$ ,  $\{f, \delta\}$ ,  $\{f, \varepsilon\}$ ,  $\{d, \delta\}$ ,  $\{d, \varepsilon\}$ , and  $\{\delta, \varepsilon\}$ . Table 2.2-9 displays an example secondary continuum block, with descriptions of each parameter. To make the multicontinuum model more flexible, in the slab geometry the options were added to specify half-fracture aperture and to read in the length parameter from a dataset.

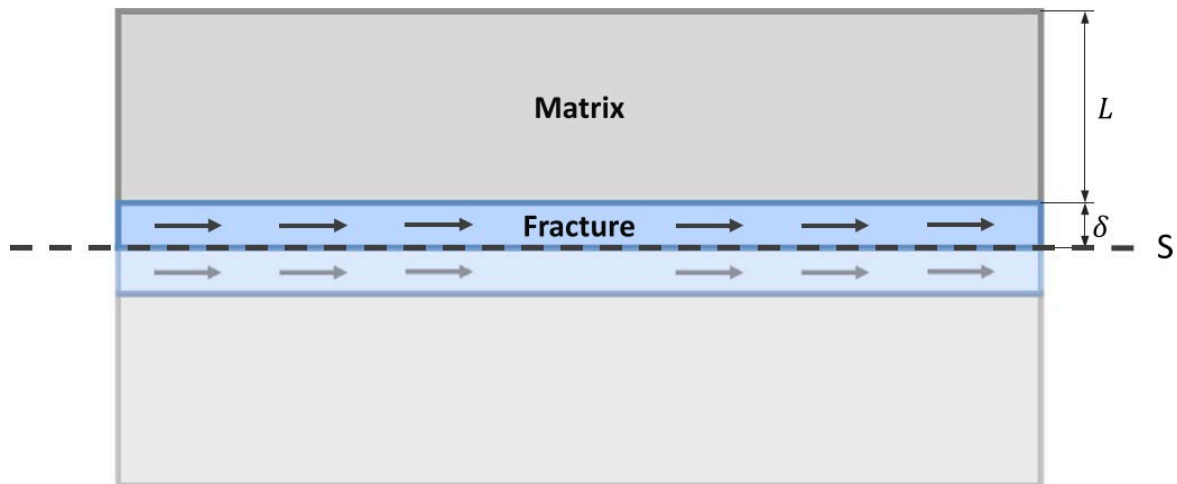


Figure 2.2-7 Slab geometry from Iraola et al., 2019

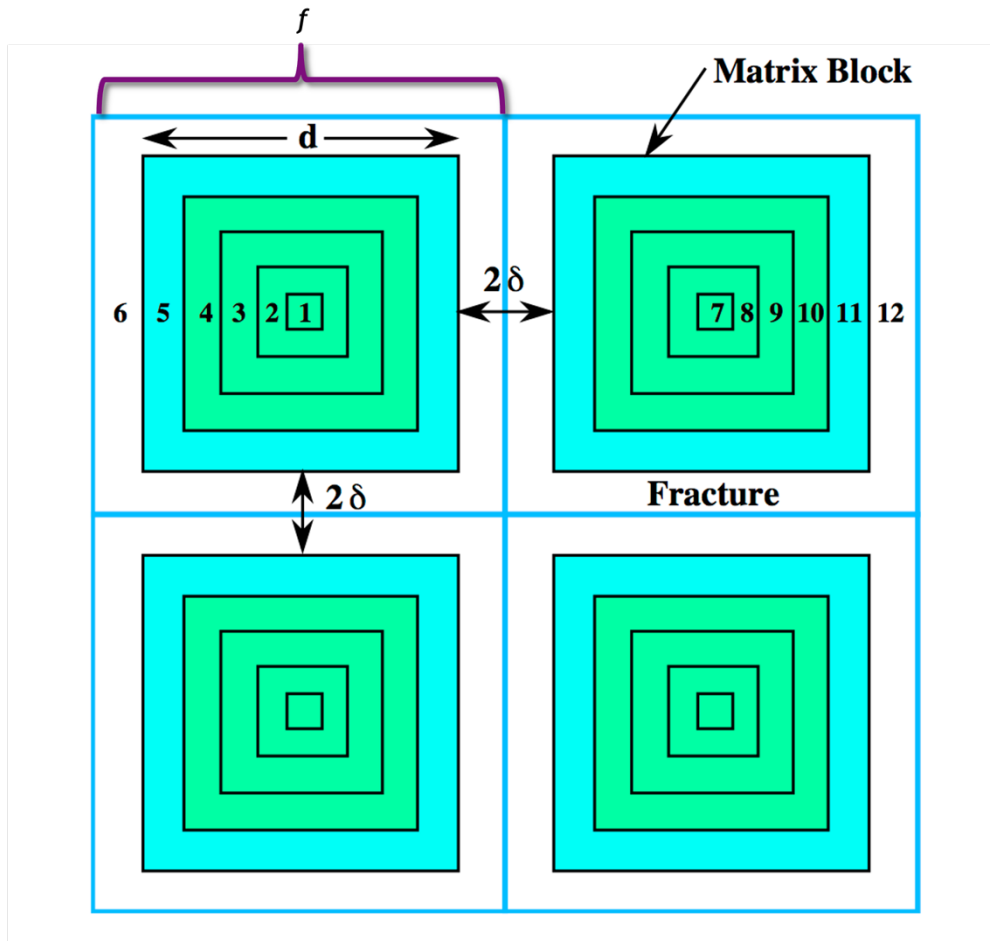


Figure 2.2-8 Nested cubes geometry, taken from Lichtner and Karra, 2014.

**Table 2.2-9 Multiple continuum input card with descriptions of parameters and applicable multiple continuum geometry parameters that each input can be applied to. Values listed are examples and not physically representative.**

Input	Description	Applicable Geometry
SECONDARY CONTINUUM		
TYPE SLAB	Secondary continuum geometry, options include: SLAB, NESTED_CUBES, NESTED_SPHERES. Must be specified first	
LENGTH 1	Half fracture spacing [m] (can be specified as dataset for spatially varying length)	slab
AREA 1.0	Fracture/matrix interfacial area per unit (bulk) volume [1/m]	slab
MATRIX_BLOCK_SIZE 40.d0	Length of largest matrix block size [m].	Nested cubes
FRACTURE_SPACING 50.d0	The size of the matrix block plus the fracture aperture [m]	Nested cubes
RADIUS 50.d0	Length of radius in nested spheres [m]	Nested spheres
EPSILON 0.00005d0	Fracture volume fraction (can be specified as dataset for spatially varying epsilon)	Slab, nested cubes, nested spheres
APERTURE 1.0d0	Half fracture aperture [m]	Slab, nested cubes
NUM_CELLS 100	Number of cells in secondary continuum (per primary cell)	Slab, nested cubes, nested spheres
POROSITY 0.01	Porosity of the matrix	Slab, nested cubes, nested spheres
LIQUID_DIFFUSION_COEFFICIENT 1.6d-10	Effective aqueous diffusion coefficient, includes tortuosity	Slab, nested cubes, nested spheres
GAS_DIFFUSION_COEFFICIENT 1.6d-10	Effective gas diffusion coefficient, includes tortuosity	Slab, nested cubes, nested spheres
LOG_GRID_SPACING 0.01d0	Enables log spacing and specifies size of outer spacing [m] (with outer cell being the secondary cell closest to the primary)	Slab, nested cubes

### 2.2.3.2 Log Grid Spacing

The log grid spacing functionality in the multiple continuum model was also updated. To obtain the logarithmic grid spacing, a user specifies the spacing of the grid cell closest to the primary continuum. Spacing can then be calculated as (Lichtner and Karra, 2014):

$$\Delta\xi_l = \rho\Delta\xi_{l-1}, (l = 1, \dots, M) \quad \text{Equation 2.2-11}$$

with  $\Delta\xi_1$  being the inner most grid spacing (farthest away from primary continuum) and  $\Delta\xi_M$  being the outer spacing. The factor  $\rho$  is then calculated using the following relationship:

$$\frac{1-\rho}{1-\rho^M}\rho^{M-1} = \frac{2\Delta\xi_M}{d} \quad \text{Equation 2.2-12}$$

with  $\Delta\xi_1$  calculated as:

$$\Delta\xi_1 = \frac{\Delta\xi_M}{\rho^{M-1}} \quad \text{Equation 2.2-13}$$

Depending on the value specified for the outer spacing, the cell closest to the primary continuum can either be the smallest or largest cell in the secondary continuum. An error message has been added when the latter occurs since it doesn't make physical sense or improve convergence. This ability has also been extended to the slab geometry with new regressions tests added to ensure future compatibility. In the future, the log grid spacing is planned for the nested spheres geometry.

### 2.2.3.3 UFD Decay

To use the multiple continuum model with a full-scale repository assessment, compatibility with PFLOTRAN's Used Fuel Disposition (UFD) Decay Process Model was added. This process model simulates radionuclide isotope decay, ingrowth, and phase partitioning and was created for use as part of the Geologic Disposal Safety Assessment (GDSA) Framework. The model is called at each transport time step where the total mass of each isotope is summed based on the mass in the aqueous, sorbed, and precipitated phase. The total mass then decays according to the Bateman Equations. Afterward, the total mass is partitioned back into aqueous, sorbed, and precipitated phases and isotope concentrations are calculated from the isotope mole fraction and elemental concentrations.

A single decay chain was modeled using the UFD Decay process model and applied to a single fracture domain considering the isotope  $^{241}\text{Am}$  decaying to  $^{237}\text{Np}$  versus a non-decaying tracer diffusing into the matrix. Solubility, distribution coefficients, and decay rates were taken from Mariner et al., 2011 and are listed in Table 2.2-10.

**Table 2.2-10 UFD Decay test problem values**

Parameter	Value
Inlet concentration <sup>241</sup> Am	4 x 10 <sup>-7</sup> mol/kg
Inlet concentration <sup>237</sup> Np	1 x 10 <sup>-12</sup> mol/kg
<sup>241</sup> Am Solubility	4 x 10 <sup>-7</sup> mol/L
<sup>237</sup> Np Solubility	4 x 10 <sup>-9</sup> mol/L
<sup>241</sup> Am Matrix K <sub>d</sub>	0.04 m <sup>3</sup> /kg
<sup>237</sup> Np Matrix K <sub>d</sub>	0.2 m <sup>3</sup> /kg
<sup>241</sup> Am Decay Rate	5.08 x 10 <sup>-11</sup> 1/s
<sup>237</sup> Np Decay Rate	1.03 x 10 <sup>-14</sup> 1/s

A Dirichlet boundary condition was assumed at the inlet of the fracture and modeled with a 10 m length in the primary continuum and 1 m in the secondary continuum. In the primary continuum, 100 cells were used where each cell had 100 secondary cells associated with it. The concentration in the fracture and matrix can be seen in Figure 2.2-9 and Figure 2.2-10 at 1000 and 5000 days. Tracer can be seen as far as ~4 m down the fracture at 5,000 days in the non-decaying tracer scenario. In the decaying isotope scenario, the isotope travels less than 2 m down the fracture at 5000 days. The results demonstrate an increase in radionuclide retardation when considering decay in a fractured system. This is illustrated by diffusion into and decay within the secondary continuum decreasing the concentrations downgradient in the fractured system.

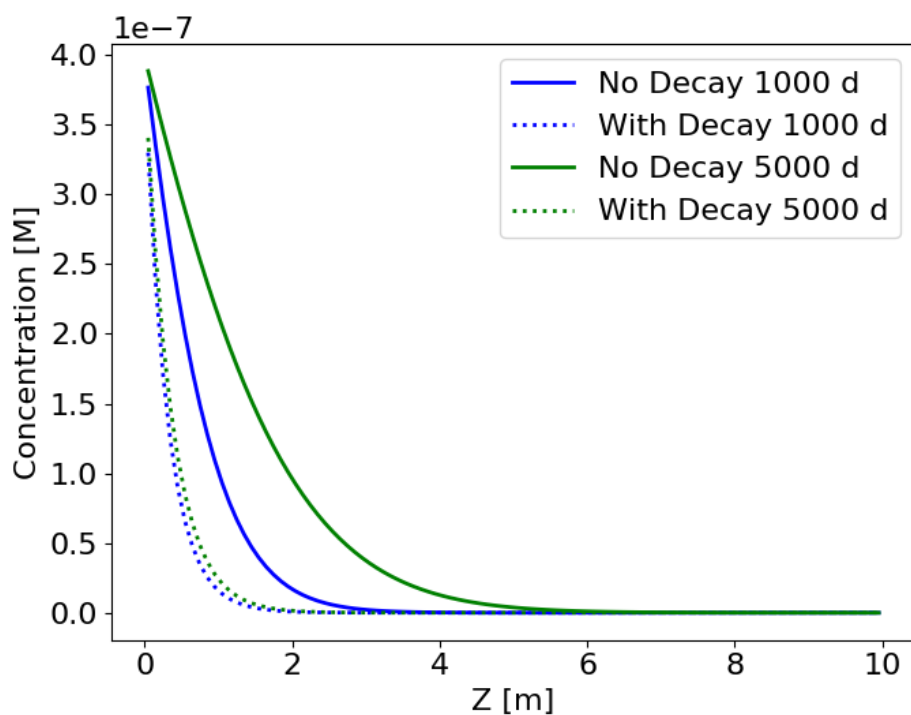


Figure 2.2-9 Concentration in the fracture with a decaying isotope (dotted line) versus non decaying tracer (solid line)

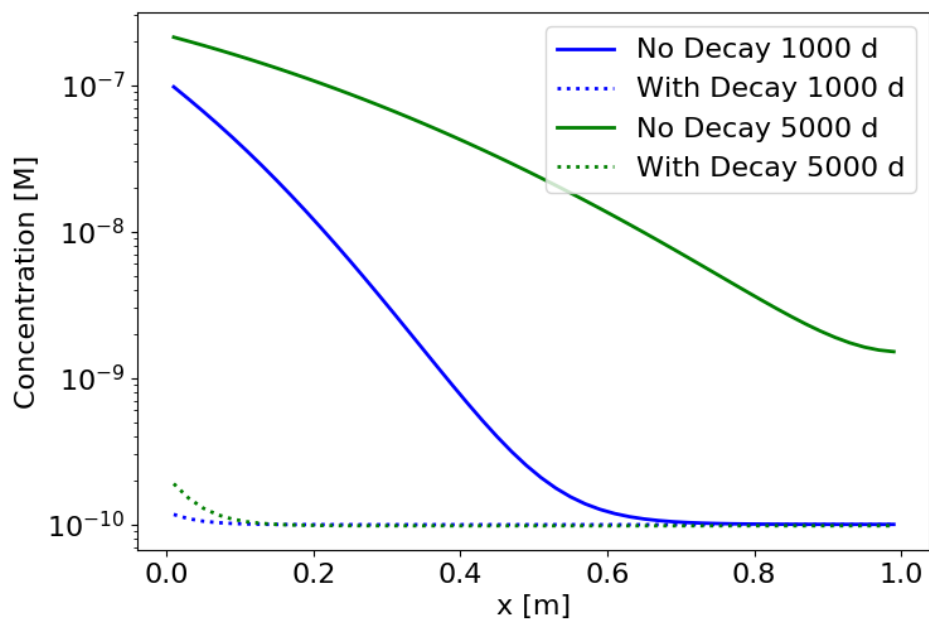


Figure 2.2-10 Concentration in the matrix with a decaying isotope (dotted line) versus non decaying tracer (single line)

The multicontinuum capability was then applied to a 4-fracture network (built based on an example provided with dfnWorks [Hyman et al., 2015]). The problem models advection and diffusion through the four fractures within a cubic domain into the rock matrix. The fractures were generated using dfnWorks. The fractures were upscaled to an Equivalent Continuous Porous Medium (ECPM) via the Python script mapDFN (Stein et al., 2017). dfnWorks outputs apertures, permeabilities, radii, the vector defining the unit normal to the fractures, and coordinates of the fracture center. These files along with parameters defining the domain and grid cell size for the ECPM were used as input for mapDFN. Upscaled anisotropic permeability, porosity, and tortuosity were then output based on the intersection of fractures within grid cells. The porosity values for the ECPM were then used as input into the DCDM model to define fracture volume fraction. The matrix length for each grid cell was specified as  $(1 - \phi) \times 20$  m, where  $\phi$  is the porosity in the grid cell.

Groundwater flow was simulated by a steady (saturated, single-phase) pressure gradient along the x-axis (Figure 2.2-11). Transport was simulated using PFLOTTRAN's multiple continuum model and UFD Decay process model. An initial pulse of  $^{241}\text{Am}$  was inserted uniformly along the fractures on the west face ( $x = -500$ ) of the domain at time zero; the concentration at the west face was set to zero for all other times. The isotope exits the domain through the fractures on the east face ( $x = 500$ ). Figure 2.2-12 shows the mean concentration of each isotope in the entire system and Figure 2.2-13 shows moles of each isotope passing through the outflow boundary ( $x = 500$  m) with time. The mean concentration of  $^{237}\text{Np}$  increases once  $^{241}\text{Am}$  decays and then decreases again around  $\sim 1000$  years as it exits the domain.

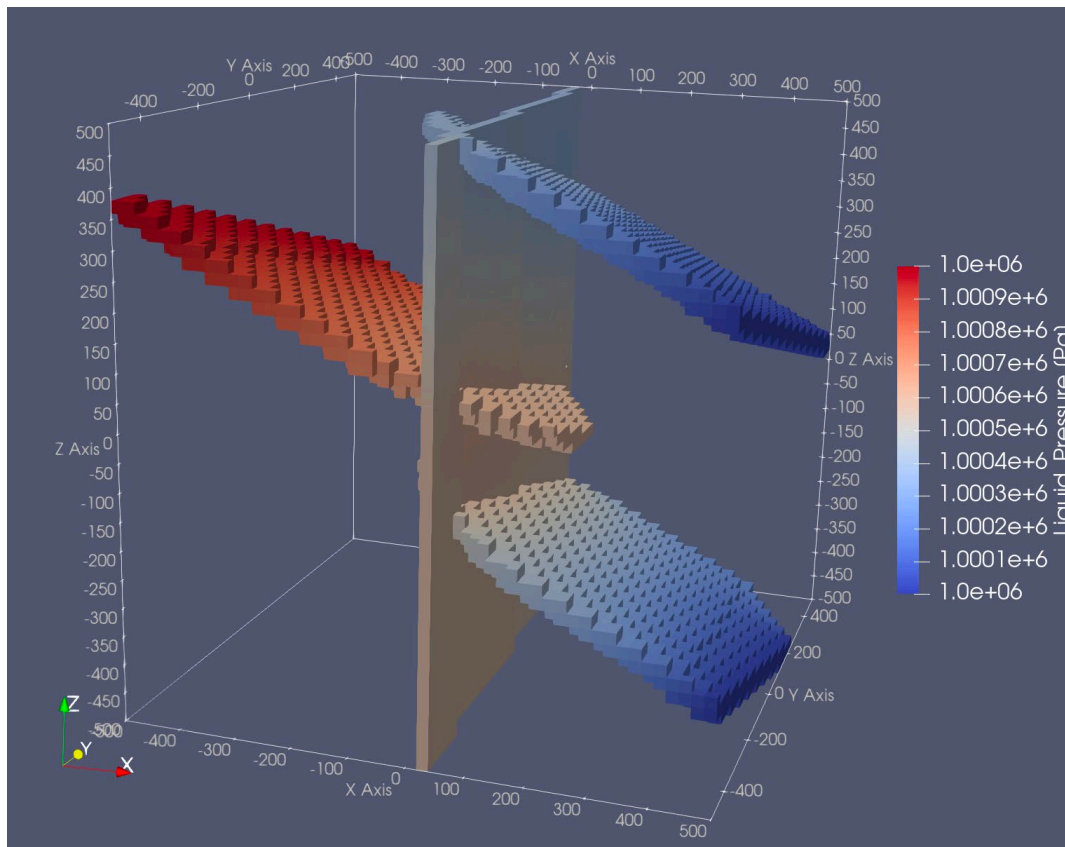


Figure 2.2-11 Four-fracture pressure solution for ECPM used as steady state solution for the transport problem.



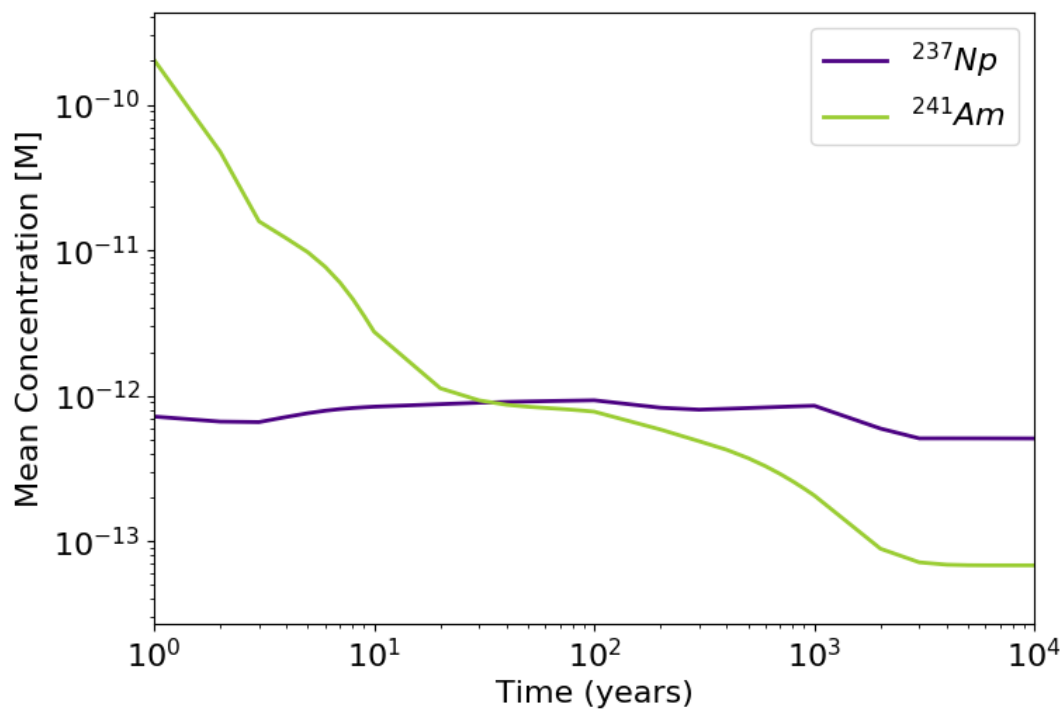


Figure 2.2-12 Mean concentration of isotopes in the entire 4-fracture system.

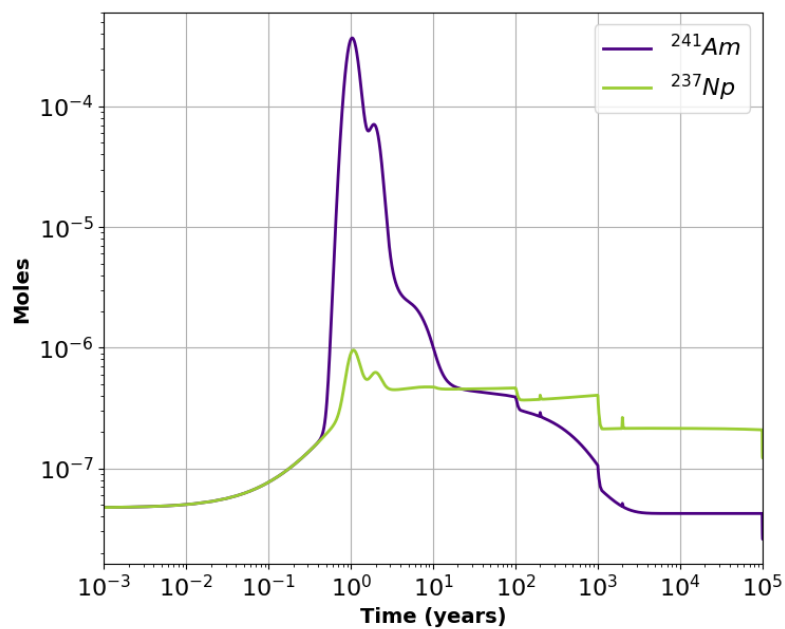
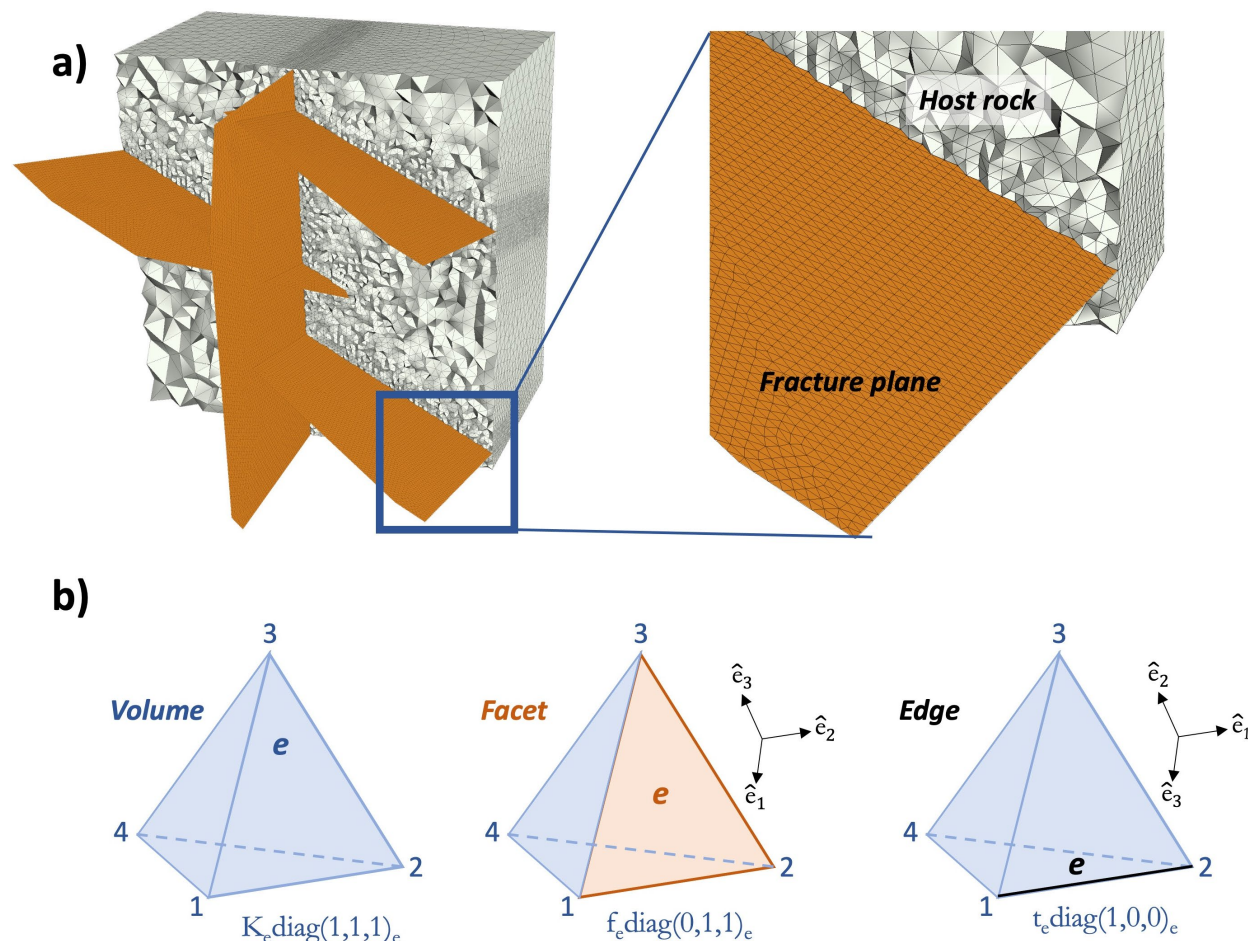


Figure 2.2-13 Moles of each isotope passing through 4-fracture outflow (x=500 m).

## 2.2.4 Hi-FEM

Groundwater flow in the four-fracture model was also simulated by using a new technique developed at Sandia known as the hierarchical finite element method (Hi-FEM; Weiss, 2017; USPTO-application:15/871,282). In this model, it is assumed that the fluid flow is steady state, and that saturated flow is driven by a pressure gradient along the x-axis and can occur in both fractures and the porous rock matrix. Matrix diffusion becomes particularly important in flow and transport problems where the heterogenous porous rock is permeable and contributes to the overall flow pattern. Moreover, in the case of considering multiple physical processes for the same geologic model, neglecting the host porous rock that may be vital for other physics (i.e., heat or electromagnetics) challenges the multi-physics coupling by imposing strong physical assumptions.

Explicit, volumetric fracture representations in geologic media require excessive mesh refinement and impose a computational burden. To overcome these challenges, Hi-FEM employs the hierarchical basis functions in the classical finite element analysis to represent material properties on each dimensional component of a given tetrahedral finite element (Weiss, 2017). The hierarchical material concept in the finite element analysis is introduced by using a composite function of the hydraulic conductivity that incorporates the contributions not only from volume elements of a finite element mesh but also from their lower dimensional components such as facets and edges (Figure 2.2-14a). The basis functions of the lower dimensional elements are defined in the local coordinates considering a reference frame with orthogonal unit vectors  $\hat{e}_1$ - $\hat{e}_2$ - $\hat{e}_3$  (Figure 2.2-14b). While the basis function employs  $\hat{e}_2$ - $\hat{e}_3$  plane for facets, solely the  $\hat{e}_1$  vector is used in the basis function for edges. Considering the superposition principle, the hierarchical conductivity function composes the hydraulic conductivity on volumes, the conductance on facets and the product of conductivity and cross-sectional area on edges. Because the geometric and physical properties of the small model features are incorporated into the modeling by utilizing the composite conductivity function before any calculation for the solution, there is no need to impose internal boundary conditions, constraints or any other special treatment in the finite element analysis.



**Figure 2.2-14 (a) Illustration of lower dimensional model features in a 3D conforming tetrahedral finite element mesh (b) Hierarchical material representations at a tetrahedron (volume  $e$ , facet  $e$ , edge  $e$ ).  $K_e$  is the hydraulic conductivity,  $f_e$  is the conductance and  $t_e$  is the conductivity-area product.  $\hat{e}_1$ ,  $\hat{e}_2$  and  $\hat{e}_3$  denote the principal axes of a reference frame.**

Therefore, Hi-FEM is able to simultaneously represent 2D structures in the form of connected facets (i.e., fractures) and 1D curvilinear features in the form of connected edges (i.e., streams, canals, wellbores) in 3D geologic media without the need for a dual grid. The flow process occur at the boundary between conductive fractures and a host rock without any need of transfer mechanism or coupling (Beskardes et al., 2022). In addition, conductive fractures can contribute to the flow in Hi-FEM simulations without any restriction regardless of their location and connectivity (i.e., non-intersecting, isolated and dead-end fractures). The accuracy of Hi-FEM has been benchmarked against the analytical solutions of various models and its performance has been evaluated for both the Poisson's equation and transient fluid flow (Weiss, 2017; Beskardes et al., 2022).

The fractures in the four-fracture problem are represented as 2D planes in the form of connected facets in the tetrahedral mesh. Here, the conforming mesh is generated by using the meshing package "Cubit" (Blacker et al., 1994) and by employing the advancing-front technique for discretization. The entire 1 km<sup>3</sup> computational domain results in a total of 1.98 M tetrahedra and the fractures are defined with ~ 60,000 facets (Figure 2.2-15).

Since the insignificant dimension of fractures (aperture) is reduced in *Hi-FEM* simulations, it requires their properties to be incorporated into the material property. For this reason, instead of hydraulic

conductivity, conductance is used for fractures. By using the relation between hydraulic permeability ( $k$ ) and conductivity ( $K$ ), ( $K = k\rho_w g/\mu$ ), the model parameters needed for the *Hi*-FEM simulations can straightforwardly be calculated (Table 2.2-10).

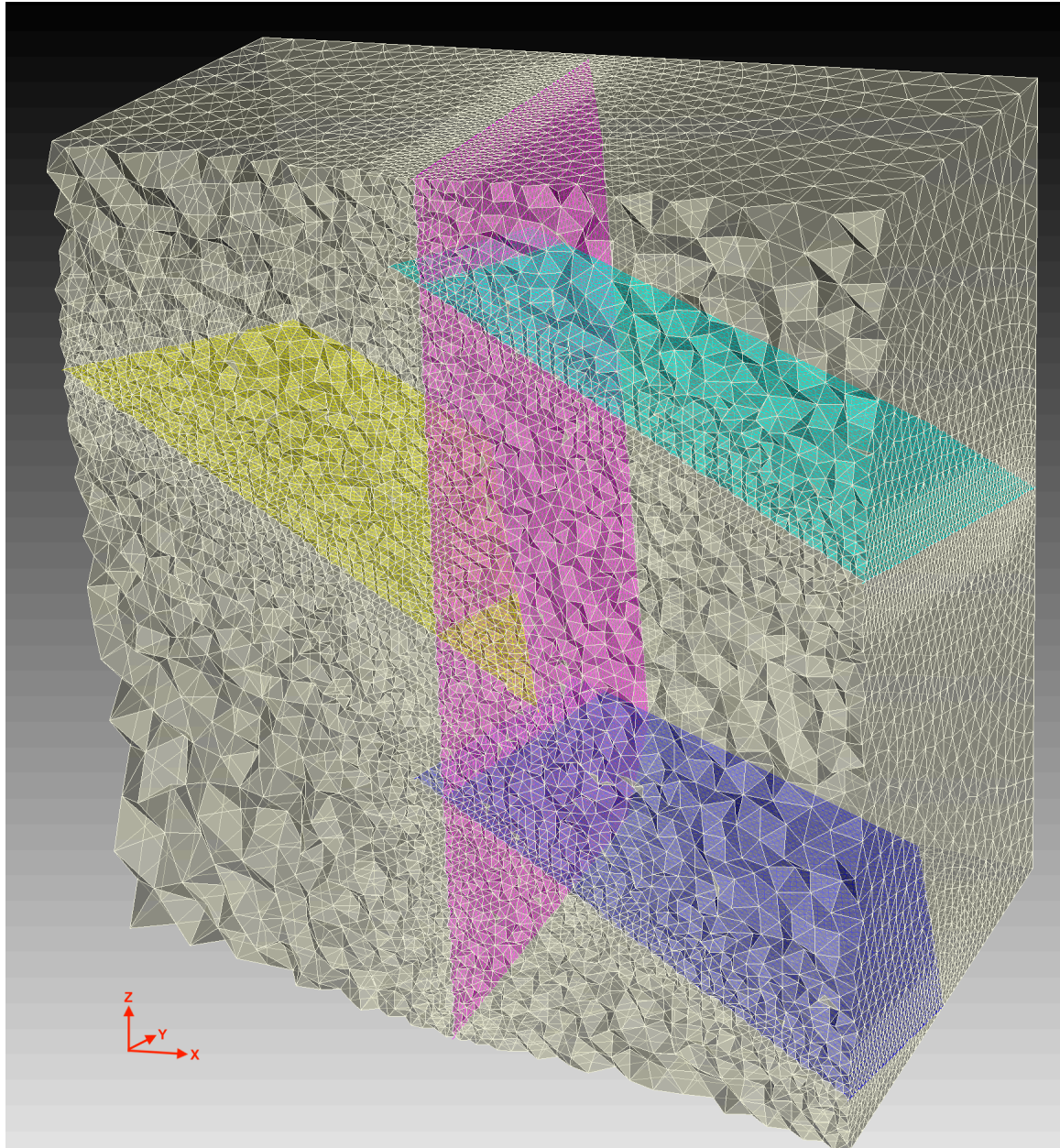


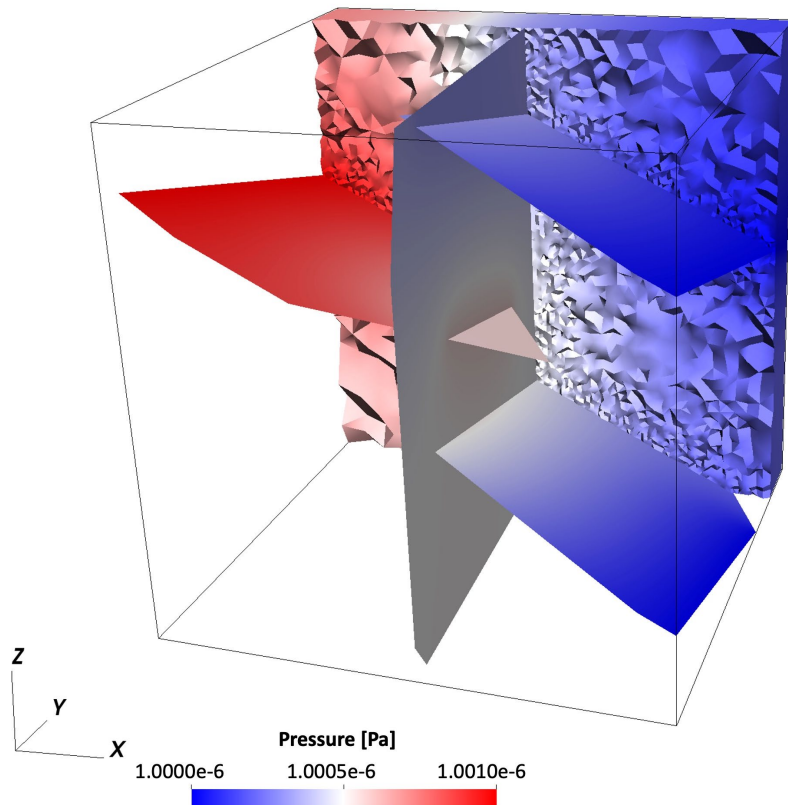
Figure 2.2-15 Cross section of the tetrahedral mesh of the four-fracture model.



**Table 2.2-11 Parameter values used in the Hi-FEM simulation for the four-fracture problem**

	$k$ [m <sup>2</sup> ]	$K$ [m/s]	Aperture [m]	Conductance ( $K \times$ Aperture) [m <sup>2</sup> /s]
Host rock	1.e-18	7.5e-12		
Fracture 1	8.333e-8	0.62	1.e-3	6.2e-4
Fracture 2	8.333e-8	0.62	1.e-3	6.2e-4
Fracture 3	8.333e-8	0.62	1.e-3	6.2e-4
Fracture 4	2.083e-8	0.156	5.e-4	7.8e-5

The simulated pressure distribution is shown in Figure 2.2-16. In addition, the Darcy velocity field of the four-fracture model is obtained by using the Hi-FEM Yeh approach that implements the Yeh's Galerkin model for both 3D and 2D features to compute the nodal velocity field of the fractured porous media with 2D fractures (Beskardes et al., 2022). The components of the Darcy velocity field obtained from the Hi-FEM's head distribution are shown in Figure 2.2-17.

**Figure 2.2-16 Pressure distribution of the four-fracture model obtained from *Hi-FEM* simulation.**

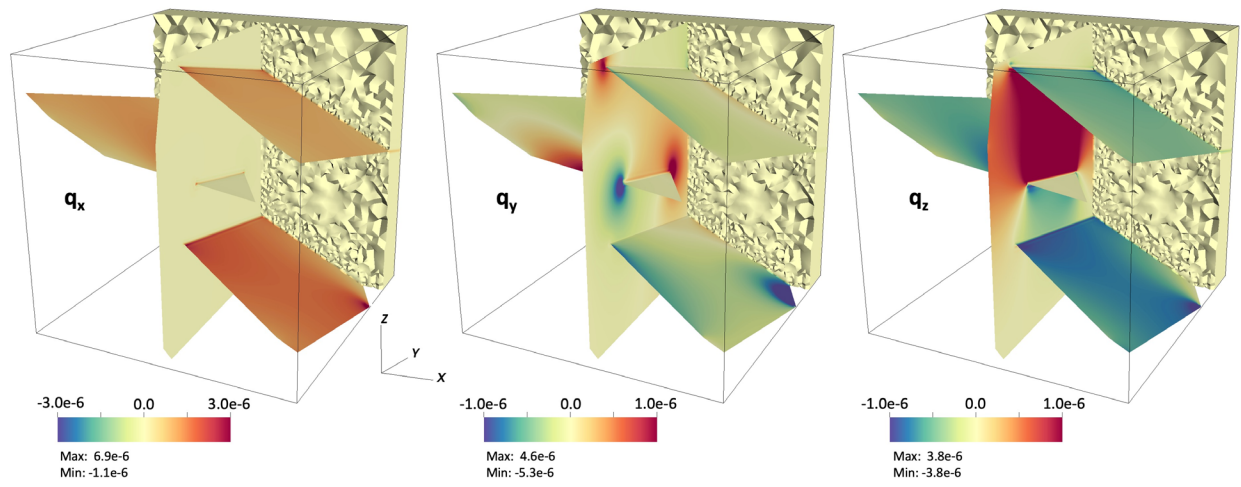


Figure 2.2-17 The nodal velocity field components  $q_x$ ,  $q_y$  and  $q_z$  of the four-fracture model.

## 2.2.5 Mass and Molar Representations of Two-Phase Reactive Transport Equations Including Aqueous, Gas and Mineral Reactions

This technical note compares balance equations involving advective and diffusive flow and transport based on mass and molar formulations. A multicomponent system is considered consisting of liquid and gas phases with homogeneous aqueous reactions and heterogeneous gas and mineral reactions. Aqueous and gas reactions are assumed to be intrinsically fast, obeying conditions of local equilibrium with transport-controlled reaction rates, whereas mineral reactions are considered to be slow, requiring a kinetic description. Details such as changes in phase (liquid to two-phase gas-liquid, gas to two-phase, two-phase to liquid or gas) are not considered (see Lichtner and Karra, 2014).

In the mass-based formulation the diffusive flux is assumed proportional to the gradient in the mass fraction. Consequently, consistency requires that factors of the average formula weight appear in the molar formulation of the molar diffusive flux. Conversely if the diffusive flux in the molar formulation is taken to be proportional to the gradient of the mole fraction, then factors of the average formula weight appear in the mass-based formulation.

### 2.2.5.1 Multicomponent Mass- and Molar-Based Diffusive Flux

#### Mass-Based Conservation Equations

The mass-based flow and transport equations in a partially saturated porous medium containing liquid and gas phases in equilibrium with each other are given by

$$\frac{\partial}{\partial t} \phi (s_l \rho_l y_k^l + s_g \rho_g y_k^g) + \bar{\nabla} \cdot (\bar{F}_k^l + \bar{F}_k^g) = Q_k \quad \text{Equation 2.2-14}$$

for the  $k$ th component, where  $\phi$  denotes porosity,  $\rho_\beta$  is mass density,  $Q_k$  denotes a source/sink term,  $s_\beta$  is saturation satisfying

$$s_l + s_g = 1 \quad \text{Equation 2.2-15}$$

and  $y_k^\beta$  the mass fraction of the  $k$ th species in phase  $\beta$  satisfying

$$\sum_k y_k^\beta = 1 \quad \text{Equation 2.2-16}$$

The flux  $F_k^\beta$  consists of contributions from advection and diffusion (dispersion is not considered for simplicity)

$$\bar{F}_k^\beta = \bar{q}_\beta \rho_\beta y_k^\beta + \bar{J}_k^\beta \quad \text{Equation 2.2-17}$$

where  $\vec{q}_\beta$  denotes the Darcy velocity of fluid phase  $\beta$ . The diffusive flux  $\vec{J}_k^\beta$  is assumed to be proportional to the gradient in the mass fraction given by

$$\vec{J}_k^\beta = -\phi s_\beta D_\beta \rho_\beta \vec{\nabla} y_k^\beta \quad \text{Equation 2.2-18}$$

not all of which are independent as their sum is zero

$$\sum_k \vec{J}_k^\beta = 0 \quad \text{Equation 2.2-19}$$

These equations are assumed to apply to variable density liquid and gas phases. Note that mass is not conserved separately for liquid and gas phases, but only the total mass is conserved since mass may be transferred from one phase to another to maintain equilibrium.

### ***Molar-Based Conservation Equations***

To convert the mass-based equations to a molar concentration scale it is necessary to convert the mass density to molar density and mass fractions to mole fractions  $x_\beta^k$  satisfying

$$\sum_k x_\beta^k = 1 \quad \text{Equation 2.2-20}$$

To do this, note that

$$y_k^\beta = \frac{M_k^\beta}{M_\beta} \quad \text{Equation 2.2-21}$$

$$= \frac{W_k n_k^\beta}{n_\beta M_\beta} \quad \text{Equation 2.2-22}$$

$$= W_\beta^{-1} W_k x_k^\beta \quad \text{Equation 2.2-23}$$

where  $M_k^\beta$  and  $M_\beta$  denote the mass of the  $k$ th species and total mass of phase  $\beta$ , respectively,  $n_\beta$  denotes the total number of moles of phase  $\beta$ ,  $W_k$  denotes the formula weight of the  $k$ th species, and the average formula weight  $W_\beta$  is given by

$$W_\beta = \frac{M_\beta}{n_\beta} = \sum_k W_k x_k^\beta = \frac{1}{\sum_k W_k^{-1} y_k^\beta} \quad \text{Equation 2.2-24}$$



Multiplying Equation 2.2-14 through by  $W_k^{-1}$  and noting that

$$W_k^{-1} \rho_\beta y_k^\beta = \eta_\beta x_k^\beta \quad \text{Equation 2.2-25}$$

where  $\eta_\beta$  denotes the molar density

$$\rho_\beta = W_\beta \eta_\beta \quad \text{Equation 2.2-26}$$

leads to the molar-based equation

$$\frac{\partial}{\partial t} \phi (s_l \eta_l x_k^l + s_g \eta_g x_k^g) + \bar{\nabla} \cdot (\vec{f}_k^l + \vec{f}_k^g) = W_k^{-1} Q_k \quad \text{Equation 2.2-27}$$

where the flux  $\vec{f}_k^\beta$  consists of advective and diffusive components defined by

$$\vec{f}_k^\beta = \vec{q}_\beta \eta_\beta x_k^\beta + \vec{j}_k^\beta \quad \text{Equation 2.2-28}$$

with diffusive flux

$$\vec{j}_k^\beta = W_k^{-1} \vec{j}_k^\beta \quad \text{Equation 2.2-29}$$

$$= -\phi s_\beta D_\beta \eta_\beta W_\beta \bar{\nabla} (W_\beta^{-1} x_k^\beta) \quad \text{Equation 2.2-30}$$

As in the mass-based formulation, not all diffusive fluxes are independent and this is also the case for the molar formulation since

$$\sum_k W_k \vec{j}_k^\beta = \vec{0} \quad \text{Equation 2.2-31}$$

The expression for the molar-based flux differs from the usual formulation by the presence of the average formula weight  $W_\beta$  appearing in the diffusive flux terms. If  $W_\beta \approx \text{constant}$ , these factors cancel out and the usual formulation is retrieved.

### 2.2.5.2 Modeling Multicomponent Systems with Aqueous, Gas and Mineral Reactions

#### Aqueous-Gas-Mineral Reactions

Mass is conserved by chemical reactions as opposed to a molar-based formulation in which moles are not conserved. However, the molar formulation has the advantage that reaction rates are proportional to the stoichiometric coefficients, whereas the mass-based approach is proportional to the species formula weight which is more difficult to interpret. Nevertheless, the two approaches should be equivalent and must give identical results.

In the following, reactions involving aqueous complexes, gases and minerals are written in terms of an independent set of aqueous species referred to as the canonical form (Lichtner, 1985). Primary species (basis species or components) are denoted by  $A_j^l$ , ( $j = 1, \dots, N_c$ ), where  $N_c$  denotes the number of primary species. Each aqueous homogeneous reaction is associated with a single aqueous species  $A_i^l$  referred to as a secondary species given by



with stoichiometric coefficients  $\nu_{ji}^l$  and reaction rate  $\Gamma_i^l$ . In what follows it is assumed that the aqueous homogeneous reactions are intrinsically fast and therefore the reaction rates  $\Gamma_i^l$  can be replaced by algebraic mass action equations given by

$$m_i^l = \frac{K_i^l}{\gamma_i^l} \prod_{j \in \text{pri}} (\gamma_j^l m_j^l)^{\nu_{ji}^l} \quad \text{Equation 2.2-33}$$

where  $m_j^l$ ,  $m_i^l$  refer to the molality of the subscripted species with corresponding activity coefficients  $\gamma_j^l$ ,  $\gamma_i^l$  and equilibrium constants  $K_i^l$ . The notation  $j \in \text{pri}$ ,  $i \in \text{sec}$ ,  $k \in \text{gas}$  or  $m \in \text{min}$  is used in the product or summation symbols  $\Pi$ ,  $\Sigma$ , to indicate that  $j$  runs over the set of primary species,  $i$  runs over all secondary species,  $k$  runs over all gases and  $m$  runs over all minerals, respectively.

Secondary species play a special role in that they may be swapped with primary species provided that the resulting set of reactions are linearly independent. The results are not changed by this operation because of the assumption of local equilibrium. For example,  $\text{Al}^{3+}$  may be swapped with  $\text{Al}(\text{OH})^{-4}$  without altering the results provided an equilibrium mass action relation exists between the two species.

In addition to aqueous complexing reactions, gas and mineral reactions are also assumed to take place and can be written in the form



with gas species  $A_k^g$  and stoichiometric coefficients  $\nu_{jk}^g$ , and mineral precipitation and dissolution reactions

$$\sum_{j \in pri} \nu_{jm} A_j^l \rightleftharpoons M_m, \quad m \in min \quad \text{Equation 2.2-35}$$

for the  $m$ th mineral  $M_m$  with stoichiometric coefficients  $\nu_{jm}$ . These reactions have rates  $\Gamma_k^g$  and  $\Gamma_m$ , respectively.

Reactions involving gases are assumed to be intrinsically fast with concentrations obeying law of mass action equations given by

$$c_k^g = \frac{K_k^g}{RT} \prod_{j \in pri} (\gamma_j^l m_j^l)^{\nu_{ji}^g} \quad \text{Equation 2.2-36}$$

where the gas concentration is denoted by  $c_k^g$  with equilibrium constants  $K_k^g$ . The latter expression is derived from the ideal gas law. The actual reaction rates for secondary and gas species can be obtained by differentiation once the solution to the primary species transport equations has been obtained using the transport equations, Equation 2.2-44 and Equation 2.2-45, below.

Examples of equivalent gas reactions are given by



Mineral reactions, which are assumed have rates which range from surface to transport controlled depending on several factors including the rate constant, specific surface area, temperature and solubility, are treated kinetically using a phenomenological transition state theory rate law (Lichtner, 2016). Furthermore, minerals may not be present over the entire computational domain, but form subregions referred to as reaction zones. This is more difficult to implement in a local equilibrium approach requiring different sets of primary species in each domain or zone where minerals are present.

Because of the assumption of local equilibrium for secondary species, they may be eliminated from gas and mineral reactions without loss in generality. If, for example, a gas or mineral reaction includes secondary species in addition to primary species as in the following gas reaction for the  $k$ th gas species

$$\sum_{j \in pri} \nu_{jk}^g A_j^l + \sum_{i \in sec} \nu_{ik}^g A_i^l \rightleftharpoons A_k^g \quad \text{Equation 2.2-40}$$

the secondary species may be eliminated using Equation 2.2-32 to yield

$$\sum_{j \in pri} \nu_{jk}^g A_j^l + \sum_{i \in sec} \sum_{j \in pri} \nu_{jk}^g \nu_{ji}^l A_j^l \rightleftharpoons A_k^g \quad \text{Equation 2.2-41}$$

or, collecting terms,

$$\bar{v}_{jk}^g = v_{jk}^g + \sum_{i \in \text{sec}} v_{ji}^l v_{ik}^g \quad \text{Equation 2.2-42}$$

The same consideration applies to mineral reactions.

Other reactions such as sorption reactions including ion exchange and surface complexation can be easily included but are not considered further in what follows. No special consideration of redox reactions is needed which are treated in a similar fashion as any other homogeneous or heterogeneous reaction but may require a kinetic treatment as they can be intrinsically slow.

### 2.2.5.3 Mass-Based Reactive Transport Equations

#### Kinetics

In what follows, the subscripts  $j$ ,  $i$ ,  $k$ , and  $m$  are reserved for primary, secondary, gas and generic species, and minerals, respectively, unless otherwise stated. The mass-based reactive transport equations treating all reactions described by kinetic rate laws for reactions (Equation 2.2-32), (Equation 2.2-34) and (Equation 2.2-35), applied to a porous medium with porosity  $\phi$  are given by

$$\frac{\partial}{\partial t} (\phi S_l \rho_l y_j^l) + \bar{\nabla} \cdot \bar{F}_j^l = -W_j \sum_i v_{ji}^l \Gamma_i^l - W_j \sum_k v_{jk}^g \Gamma_k^g - W_j \sum_m v_{jm} \Gamma_m \quad \text{Equation 2.2-43}$$

for primary species, and

$$\frac{\partial}{\partial t} (\phi S_l \rho_l y_i^l) + \bar{\nabla} \cdot \bar{F}_i^l = W_i \Gamma_i^l \quad \text{Equation 2.2-44}$$

$$\frac{\partial}{\partial t} (\phi S_g \rho_g y_k^g) + \bar{\nabla} \cdot \bar{F}_k^g = W_k \Gamma_k^g \quad \text{Equation 2.2-45}$$

$$\frac{\partial}{\partial t} (\rho_m \phi_m) = W_m \Gamma_m \quad \text{Equation 2.2-46}$$

for secondary species, gases and minerals with respective reaction rates  $\Gamma_i^l$ ,  $\Gamma_k^g$ , and  $\Gamma_m$ . The quantities  $W_j$ ,  $W_i$ ,  $W_k$ ,  $W_m$  refer to the formula weight of the subscripted species and convert the reaction rate expressed in moles  $\text{m}^{-3} \text{s}^{-1}$  to  $\text{kg} \text{m}^{-3} \text{s}^{-1}$ . Finally,  $\phi_m$  denotes the mineral volume fraction with molar volume  $\bar{V}_m$  and mineral mass density  $\rho_m$

$$\rho_m = W_m \bar{V}_m^{-1} \quad \text{Equation 2.2-47}$$

A disadvantage of the kinetic approach is that it is necessary to solve a large number of partial differential equations with one equation per species. In addition, kinetic rate laws must be provided for each reaction. If some reactions are intrinsically fast local chemical equilibrium conditions apply and the reaction rates may be replaced by algebraic constraints given by mass action equations. This simplification is explored in the next section.

### ***Homogeneous Equilibria***

In this section reaction rates for homogeneous aqueous and heterogeneous gas reactions are eliminated from the primary species transport equations and replaced by algebraic constraints given in Eqns. (Equation 2.2-33) and (Equation 2.2-36) corresponding to secondary and gas species (Lichtner, 1985). Reaction rates for minerals are considered to be slow provided by transition state theory. This leads to the revised equations for primary species

$$\frac{\partial}{\partial t} \phi (s_l \rho_l Y_j^l + s_g \rho_g Y_j^g) + \vec{\nabla} \cdot \vec{\mathcal{F}}_j = -W_j \sum_m \nu_{jm} \Gamma_m \quad \text{Equation 2.2-48}$$

with total mass fractions  $Y_j^\beta$  in the aqueous and gas phases defined, respectively, by

$$Y_j^l = y_j^l + W_j \sum_i W_i^{-1} \nu_{ji}^l y_i^l \quad \text{Equation 2.2-49}$$

$$Y_j^g = y_j^g + W_j \sum_k W_k^{-1} \nu_{jk}^g y_k^g \quad \text{Equation 2.2-50}$$

The total mass flux  $\vec{\mathcal{F}}_j$  is given by the sum of liquid  $\vec{\mathcal{F}}_j^l$  and gas  $\vec{\mathcal{F}}_j^g$  fluxes

$$\vec{\mathcal{F}}_j = \vec{\mathcal{F}}_j^l + \vec{\mathcal{F}}_j^g \quad \text{Equation 2.2-51}$$

defined as

$$\vec{\mathcal{F}}_j^l = \vec{F}_j^l + W_j \sum_i W_i^{-1} \nu_{ji}^l \vec{F}_i^l \quad \text{Equation 2.2-52}$$

$$\vec{\mathcal{F}}_j^g = \vec{F}_j^g + W_j \sum_k W_k^{-1} \nu_{jk}^g \vec{F}_k^g \quad \text{Equation 2.2-53}$$

with  $\vec{F}_{j,i}^l$  and  $\vec{F}_k^g$  defined in Equation 2.2-17. The primary species transport equations in Equation 2.2-48 apply to both kinetic and local equilibrium formulations. The auxiliary transport equations for secondary and gas species are replaced with mass action equations for conditions of local equilibrium or as partial differential equations for kinetics.

Noting the mass conservation relations obeyed by chemical reactions

$$\sum_{j \in pri} W_j v_{ji}^l = W_i \quad \text{Equation 2.2-54}$$

$$\sum_{j \in pri} W_j v_{jk}^g = W_k \quad \text{Equation 2.2-55}$$

$$\sum_{j \in pri} W_j v_m = W_m \quad \text{Equation 2.2-56}$$

it follows from the definition of  $Y_j^{l,g}$  given in Equation 2.2-49 and Equation 2.2-50 that they sum to unity as demonstrated in the following

$$\sum_{j \in pri} Y_j^l = \sum_{j \in pri} y_j^l + \sum_{j \in pri} W_j \sum_{i \in sec} W_i^{-1} v_{ji}^l y_i^l \quad \text{Equation 2.2-57}$$

$$= \sum_{j \in pri} y_j^l + \sum_{i \in sec} y_i^l = \sum_{k \in aq} y_k^l = 1 \quad \text{Equation 2.2-58}$$

$$\sum_{j \in pri} Y_j^g = \sum_{j \in pri} W_j + \sum_{k \in gas} v_{jk}^g W_k^{-1} y_k^g \quad \text{Equation 2.2-59}$$

$$= \sum_{k \in gas} y_k^g = 1 \quad \text{Equation 2.2-60}$$

Thus the  $Y_j^\beta$  represent mass fractions of the total primary species concentrations.

The mass flux term, as with the accumulation term, can be written in terms of the total mass fraction  $Y_j^\beta$  for species-independent diffusion coefficients. In terms of primary species mass fractions the flux has the form

$$\mathcal{F}_j^l = \bar{q}_l \rho_l (y_j^l + W_j \sum_i W_i^{-1} v_{ji}^l y_i^l) - \phi [s_l D_l \rho_l \bar{\nabla} (y_j^l + W_j \sum_i W_i^{-1} v_{ji}^l y_i^l)] \quad \text{Equation 2.2-61}$$

$$= \bar{q}_l \rho_l Y_j^l - \phi s_l D_l \rho_l \bar{\nabla} Y_j^l \quad \text{Equation 2.2-62}$$

for the aqueous phase, and similarly for the gas phase

$$\mathcal{F}_j^g = \bar{q}_g \rho_g (W_j \sum_i W_i^{-1} v_{ji}^g y_i^g) - \phi [s_g D_g \rho_g \bar{\nabla} (W_j \sum_i W_i^{-1} v_{ji}^g y_i^g)] \quad \text{Equation 2.2-63}$$

$$= \bar{q}_g \rho_g Y_j^g + \bar{J}_j^\beta \quad \text{Equation 2.2-64}$$

where the diffusive flux,  $\bar{J}_j^\beta$ , for fluid phase  $\beta$  is given by

$$\bar{J}_j^\beta = -\phi s_\beta D_\beta \rho_\beta \bar{\nabla} Y_j^\beta \quad \text{Equation 2.2-65}$$

The diffusive flux satisfies the identity

$$\sum_{j \in \text{pri}} \vec{J}_j^\beta = \vec{0} \quad \text{Equation 2.2-66}$$

Species-dependent diffusion can be similarly derived for the primary species through inclusion of the Nernst-Planck equation to conserve electric charge. However, the total flux is no longer simply a function of the total primary species concentrations in that case.

#### 2.2.5.4 Equivalent Molar-Based Reactive Transport Equations

The following relations are used to obtain the molar-based transport equations derived from the mass-based formulation (in the following the subscript k is used to designate a generic species):

$$\rho_\beta y_k^\beta = W_\beta \eta_\beta y_k^\beta = \eta_\beta W_k x_k^\beta \quad \text{Equation 2.2-67}$$

$$y_k^\beta = \frac{W_k x_k^\beta}{\sum_{k'} W_{k'}^{-1} y_{k'}^\beta} \quad \text{Equation 2.2-68}$$

$$x_k^\beta = \frac{W_k^{-1} y_k^\beta}{\sum_{k'} W_{k'}^{-1} y_{k'}^\beta} \quad \text{Equation 2.2-69}$$

#### Kinetics

The molar-based transport equation for primary species consistent with the mass-based formulation follow from Equation 2.2-48 making use of Equation 2.2-67 - Equation 2.2-69. This results in the equation

$$\frac{\partial}{\partial t} (\phi_{S_l} \eta_l x_j^l) + \vec{\nabla} \cdot \vec{f}_j^l = -\sum_k \nu_{jk}^g \Gamma_k^g - \sum_m \nu_{jm} \Gamma_m \quad \text{Equation 2.2-70}$$

Likewise molar-based equations for secondary species, gas species and minerals consistent with the mass-based formulation are given by

$$\frac{\partial}{\partial t} (\phi_{S_l} \eta_l x_i^l) + \vec{\nabla} \cdot \vec{f}_i^l = \Gamma_i^l \quad \text{Equation 2.2-71}$$

$$\frac{\partial}{\partial t} (\phi_{S_g} \eta_g x_k^g) + \vec{\nabla} \cdot \vec{f}_k^g = \Gamma_k^g \quad \text{Equation 2.2-72}$$

$$\frac{\partial c_m}{\partial t} = \Gamma_m \quad \text{Equation 2.2-73}$$

with the mineral concentration defined as

$$c_m = \bar{V}_m^{-1} \phi_m \quad \text{Equation 2.2-74}$$

Aqueous and gas fluxes,  $\vec{f}_k^\beta$ , are given by Equation 2.2-28 where the molar-based diffusive flux is k defined in Equation 2.2-30.

### ***Homogeneous Equilibria***

The molar formulation of the primary species transport equations in local equilibrium with homogeneous aqueous reactions and heterogeneous gas reactions consistent with the mass formulation is considered next. The molar-based primary species transport equations after eliminating reaction rates for secondary species and gases become

$$\frac{\partial}{\partial t} \phi (s_l \eta_l X_j^l + s_g \eta_g X_j^g) + \vec{\nabla} \cdot \vec{\Omega}_j = - \sum_m \nu_{jm} \Gamma_m \quad \text{Equation 2.2-75}$$

with molar quantities  $X_j^{l,g}$  defining total concentrations in the aqueous and gas phases given by

$$X_j^l = x_j^l + \sum_i \nu_{ji}^l x_i^l \quad \text{Equation 2.2-76}$$

$$X_j^g = \sum_k \nu_{jk}^g x_k^g \quad \text{Equation 2.2-77}$$

The molar primary species transport equation can be obtained directly from the mass-based transport equation and holds for both kinetically controlled reactions as well as homogeneous equilibria.

The quantities  $X_j^\beta$  are analogous to  $Y_j^\beta$  in the mass-based formulation but are not fractions in the sense that they do not sum to one. The average formula weight can be expressed in terms of the total molar primary species concentrations as follows

$$W_\beta = \sum_{k \in pri \cup sec} W_k x_k^\beta \quad \text{Equation 2.2-78}$$

$$= \sum_{j \in pri} W_j x_j^\beta + \sum_{i \in sec} W_i x_i^\beta \quad \text{Equation 2.2-79}$$

$$= \sum_j W_j x_j^\beta + \sum_j W_j \sum_i \nu_{ji}^\beta x_i^\beta \quad \text{Equation 2.2-80}$$

$$= \sum_j W_j (x_j^\beta + \sum_i \nu_{ji}^\beta x_i^\beta) \quad \text{Equation 2.2-81}$$



$$= \sum_j W_j X_j^\beta \quad \text{Equation 2.2-82}$$

The total molar concentration  $X_j^\beta$  and mass fraction  $Y_j^\beta$  are related. Noting that

$$y_k^\beta = W_\beta^{-1} W_k x_k^\beta \quad \text{Equation 2.2-83}$$

It follows that

$$Y_j^\beta = W_\beta^{-1} W_j x_j^\beta + W_j \sum_i W_i^{-1} v_{ji}^\beta W_\beta^{-1} W_i x_i^\beta \quad \text{Equation 2.2-84}$$

$$= W_\beta^{-1} W_j (x_j^\beta + \sum_i v_{ji}^\beta x_i^\beta) \quad \text{Equation 2.2-85}$$

$$= W_\beta^{-1} W_j X_j^\beta \quad \text{Equation 2.2-86}$$

confirming the property

$$\sum_j Y_j^\beta = \frac{1}{W_\beta} \sum_j W_j X_j^\beta = 1 \quad \text{Equation 2.2-87}$$

The gradient term for the liquid phase transforms according to

$$\rho_l \bar{\nabla} Y_j^l = \rho_l \bar{\nabla} (y_j^l + W_j \sum_i W_i^{-1} v_{ji}^l y_i^l) \quad \text{Equation 2.2-88}$$

$$= W_j \eta_l W_l (\bar{\nabla} (W_l^{-1} x_j^l) + \sum_i W_i^{-1} v_{ji}^l \bar{\nabla} (W_l^{-1} W_i x_i^l)) \quad \text{Equation 2.2-89}$$

$$= W_j \eta_l W_l \bar{\nabla} [W_l^{-1} (x_j^l + \sum_i v_{ji}^l x_i^l)] \quad \text{Equation 2.2-90}$$

$$= W_j \eta_l W_l \bar{\nabla} (W_l^{-1} X_j^l) \quad \text{Equation 2.2-91}$$

and similarly for the gas phase. Note that summing over primary species yields

$$\sum_j W_j \eta_l W_l \bar{\nabla} (W_l^{-1} X_j^l) = \eta_l W_l \bar{\nabla} [W_l^{-1} \sum_j W_j X_j^l] \quad \text{Equation 2.2-92}$$

$$= \eta_l W_l \bar{\nabla} [W_l^{-1} W_l] = \eta_l W_l \bar{\nabla} 1 = 0 \quad \text{Equation 2.2-93}$$

As noted, the quantities  $X_j^\beta$  do not sum to one. For example, for the aqueous phase ( $\beta = 1$ ) one has

$$\sum_j X_j^l = \sum_j (x_j^l + \sum_i \nu_{ji} x_i^l) \quad \text{Equation 2.2-94}$$

$$= \sum_j x_j^l + \sum_{ij} \nu_{ji}^l x_i^l \quad \text{Equation 2.2-95}$$

$$= \sum_j x_j^l + \sum_i x_i^l + \sum_{ij} \left( \nu_{ij}^l - \frac{1}{N_c} \right) x_i^l \quad \text{Equation 2.2-96}$$

$$= 1 + \sum_{ij} \left( \nu_{ij}^l - \frac{1}{N_c} \right) x_i^l \neq 1 \quad \text{Equation 2.2-97}$$

in general.

The total molar flux is given by the sum over aqueous and gas phases

$$\bar{\Omega}_j = \bar{\Omega}_j^l + \bar{\Omega}_j^g \quad \text{Equation 2.2-98}$$

where the total aqueous flux of the  $j$ th primary species is defined as

$$\bar{\Omega}_j^l = \bar{f}_j^l + \sum_i \nu_{ji}^l \bar{f}_i^l \quad \text{Equation 2.2-99}$$

and the gas flux as

$$\bar{\Omega}_j^g = \sum_k \nu_{jk}^g \bar{f}_k^g \quad \text{Equation 2.2-100}$$

where the fluxes  $\bar{f}_k^g$  are defined in Equation 2.2-28. Substituting expressions for the flux given in Equation 2.2-28 and Equation 2.2-30 yields for the total flux

$$\bar{\Omega}_j = \bar{q}_l \eta_l X_j^l + \bar{q}_g \eta_g X_j^g - \phi \left[ s_l D_l \eta_l W_l \bar{\nabla} (W_l^{-1} X_j^l) + s_g D_g \eta_g W_g \bar{\nabla} (W_g^{-1} X_j^g) \right] \quad \text{Equation 2.2-101}$$

Expanding the term  $W_\beta \bar{\nabla} (W_\beta^{-1} X_j^\beta)$  yields

$$W_\beta \bar{\nabla} (W_\beta^{-1} X_j^\beta) = \bar{\nabla} X_j^\beta - X_j^\beta W_\beta^{-1} \bar{\nabla} W_\beta \quad \text{Equation 2.2-102}$$

$$= \bar{\nabla} X_j^\beta - X_j^\beta \bar{\nabla} \ln W_\beta \quad \text{Equation 2.2-103}$$

The first term on the right-hand side is the usual formulation, but with  $X_j^\beta$  interpreted as mole fraction which is not the case with secondary species present. The second term vanishes if  $W_\beta \approx \text{constant}$ .

### 2.2.5.5 Continuity Equation

The continuity equation for the total mass follows by summing the mass-based conservation equations, Equation 2.2-48, over all primary species. The sum over the total flux for aqueous and gas phases yields according to Equation 2.2-62 and Equation 2.2-64 using Equation 2.2-58 and Equation 2.2-60 for the liquid phase

$$\sum_{j \in pri} \bar{F}_j^l = \sum_{j \in pri} \bar{F}_j^l + \sum_{j \in pri} W_j \sum_{i \in sec} W_i^{-1} \nu_{ji}^l \bar{F}_i^l \quad \text{Equation 2.2-104}$$

$$= \sum_{j \in pri} \bar{F}_j^l + \sum_{i \in sec} \bar{F}_i^l \quad \text{Equation 2.2-105}$$

$$= \bar{q}_l \rho_l \quad \text{Equation 2.2-106}$$

and for the gas phase

$$\sum_{j \in pri} \bar{F}_j^g = \sum_{j \in pri} W_j + \sum_{k \in gas} W_k^{-1} \nu_{jk}^g \bar{F}_k^g \quad \text{Equation 2.2-107}$$

$$= \sum_{k \in gas} \bar{F}_k^g \quad \text{Equation 2.2-108}$$

$$= \bar{q}_g \rho_g \quad \text{Equation 2.2-109}$$

The diffusive flux terms disappear according to Equation 2.2-19.

Summing Equation 2.2-48 over primary species and making use of Equation 2.2-58 and Equation 2.2-60, the mass conservation equations yield the continuity equation for the total mass with a source/sink term appearing on the right-hand side due to mineral reactions

$$\frac{\partial}{\partial t} \phi (s_l \rho_l + s_g \rho_g) + \bar{\nabla} \cdot (\bar{q}_l \rho_l + \bar{q}_g \rho_g) = - \sum_m W_m \Gamma_m \quad \text{Equation 2.2-110}$$

Multiplying the molar conservation equations, Equation 2.2-75, by the formula weight  $W_j$  and summing over primary species retrieves the mass-based continuity equation.

Merely summing Equation 2.2-75 over the primary species the continuity equation in the molar formulation takes the form

$$\frac{\partial}{\partial t} \phi (s_l \eta_l \sigma_l + s_g \eta_g \sigma_g) + \bar{\nabla} \cdot (\bar{q}_l \eta_l \sigma_l + \bar{q}_g \eta_g \sigma_g + \vec{j}_i + \vec{j}_g) = - \sum_m W_m \Gamma_m \quad \text{Equation 2.2-111}$$

where  $\sigma_\beta$  is defined as

$$\sigma_\beta = \sum_{j \in \text{pri}} X_j^\beta \quad \text{Equation 2.2-112}$$

The diffusive contribution to the flux is not zero as in the mass-based case but given by

$$\vec{j}_i = -\phi s_l D_l \eta_l W_l \bar{\nabla} (W_l^{-1} \sigma_l) \quad \text{Equation 2.2-113}$$

$$\vec{j}_g = -\phi s_g D_g \eta_g W_g \bar{\nabla} (W_g^{-1} \sigma_g) \quad \text{Equation 2.2-114}$$

Thus the continuity equation in the molar formulation has extra factors  $\sigma_{l,g}$  appearing in the accumulation and diffusive flux terms that do not appear in the mass formulation which is the conventional form of the continuity equation. In order for  $\sigma_l = 1$ , would require the absence of any aqueous complexes (secondary species), and for  $\sigma_g = 1$  the absence of gas species.

### 2.2.5.6 Discussion

The molar-based continuity equation is modified from its usual form by factors involving the average molecular weight  $W_\beta$ . For constant density  $\rho_\beta$  implying also constant molar density  $\eta_\beta$  and average formula weight  $W_\beta$ , the factor  $W_\beta$  cancels out in the molar-based transport equations and the usual form for constant density is retrieved. This result entails the approximation

$$W_l = \sum_k W_k x_k^l \quad \text{Equation 2.2-115}$$

$$= W_w x_w^l + \sum_{k \neq w} W_k x_k^l \quad \text{Equation 2.2-116}$$

$$\approx W_w \quad \text{Equation 2.2-117}$$

for  $x_w^l \approx 1$ , where the subscript  $w$  refers to the solvent, e.g., H<sub>2</sub>O.

One could equally take the molar-based formulation as fundamental and derive the mass-based formulation consistent with it. Chen et al. (2006) use the molar formulation with the diffusive flux proportional to the gradient in the mole fraction, noting that it is in widespread use but give no further justification. They do not consider partitioning species into primary and secondary species. And they do not attempt to compare it with the mass-based formulation. These authors define the molar diffusive flux as given by

$$\vec{J}_k^{\beta'} = -\phi s_\beta D_\beta \eta_\beta \vec{\nabla} x_i^\beta \quad \text{Equation 2.2-118}$$

with the property

$$\sum_k \vec{J}_k^{\beta'} = \vec{0} \quad \text{Equation 2.2-119}$$

Transforming this expression to the mass-based formulation gives

$$\vec{J}_k^{\beta'} = W_k \vec{J}_k^{\beta'} \quad \text{Equation 2.2-120}$$

$$= -\phi s_\beta D_\beta \rho_\beta W_\beta^{-1} \vec{\nabla} (W_\beta y_k^\beta) \quad \text{Equation 2.2-121}$$

Note that the weighted sum of the diffusive flux now vanishes

$$\sum_k W_k^{-1} \vec{J}_k^{\beta'} = \vec{0} \quad \text{Equation 2.2-122}$$

### 2.2.5.7 Conclusion

This technical report revisits the formulation of reactive flow and transport equations in a porous medium for a multicomponent, two-phase, liquid-gas system. Reactions included homogeneous aqueous reactions, and heterogeneous gas and mineral reactions. Aqueous and gas reactions were assumed to be fast with their reaction rates replaced by algebraic mass action laws. Mineral reactions were described through surface controlled kinetic rate laws.

Molar-based reactive transport equations were derived that are consistent with a mass-based formulation for which the diffusive flux is proportional to the gradient of the mass fraction and vice versa with the diffusive flux proportional to the gradient in the mole fraction. The added factor vanishes for constant average formula weight, retrieving the usual formulation of the molar-based reactive transport equations consistent with the mass-based formulation. Finally, it was noted that in the molar formulation the quantities  $X_j^\beta$  defined in Equation 2.2-76 and Equation 2.2-77 representing total primary species concentrations do not sum to unity and therefore do not represent mole fractions. This observation has an impact on formulating a molar continuity equation for the total system.

## 2.2.6 Gas Transport Integration in Multicontinuum Transport

The multiple continuum model in PFLOTRAN solves equations for a primary and secondary continuum in a fully coupled implementation. The primary continuum with gas transport is modeled via

$$\frac{\partial}{\partial t} \epsilon_f \phi_f (s^{aq} \Psi_j^{aq,f} + s^g \Psi_j^{g,f}) + \nabla \cdot (\Omega_j^{aq,f} + \Omega_j^{g,f}) = -A_{fm} (\Omega_j^{aq,fm} + \Omega_j^{g,fm}) - \epsilon_f \sum_k \nu_{jk} \Gamma_k^f \quad \text{Equation 2.2-123}$$

where f and m denote the fracture and matrix continua, respectively,  $\epsilon_f$  is the fracture volume fraction,  $\phi_f$  is fracture porosity,  $s_{aq}$  and  $s_g$  are the saturation in the aqueous and gas phases respectively,  $\Psi_j^{aq,f}$  is the total component concentration in the aqueous phase in the fracture of species j,  $\Psi_j^{g,f}$  is the total component concentration in the gas phase in the fracture of species j,  $\Omega_j^{aq,f}$ ,  $\Omega_j^{g,f}$  is total solute flux in the fracture in the aqueous and gas phase respectively,  $\Omega_j^{fm}$  is total solute flux between the fracture and matrix,  $A_{fm}$  is the fracture-matrix interfacial area,  $\nu_{jk}$  is the stoichiometric coefficient, and  $\Gamma_k^f$  is the mineral reaction. The secondary continuum with gas transport is modeled as:

$$\frac{\partial}{\partial t} \phi_m (s^{aq} \Psi_j^{aq,m} + s^g \Psi_j^{g,m}) + \nabla_{\xi} \cdot (\Omega_j^{aq,m} + \Omega_j^{g,m}) = -\sum_k \nu_{jk} \Gamma_k^m \quad \text{Equation 2.2-124}$$

where  $\phi_m$  is matrix porosity and the gradient operator  $\nabla_{\xi}$  refers to the effective one-dimensional secondary continuum geometry. The equations for the primary and secondary continuum are solved separately and coupled together by the mass exchange flux assuming symmetry along the axis dividing them (Iraola et al., 2019):

$$\Omega_j^{aq,fm}(x, t) = \Omega_j^{aq,m}(\xi_{fm}, x|r) \quad \text{Equation 2.2-125}$$

$$\Omega_j^{g,fm}(x, t) = \Omega_j^{g,m}(\xi_{fm}, x|r) \quad \text{Equation 2.2-126}$$

where  $x$  is a point in the primary continuum,  $t$  is time, and  $\xi_{fm}$  is the outer boundary of the secondary continuum.

The first test to validate the gas diffusion implementation in PFLOTRAN's multiple continuum model considered gas diffusion in the secondary continuum only. The domain consisted of a single primary cell which was kept at a constant concentration (using the EQUILIBRIUM transport condition in PFLOTRAN) to mimic a Dirichlet boundary condition on the first cell in the secondary continuum (the cell closest to the primary continuum). In the secondary continuum, 100 cells were used and gas saturation was set to 0.999. The analytical solution for 1D gas diffusion is described as:

$$C = C_0 - C_0 \operatorname{erf}\left(\frac{x}{\sqrt{4Dt}}\right) \quad \text{Equation 2.2-127}$$

where  $C_0$  is the boundary concentration, set to 1 mol/L,  $x$  is distance,  $t$  is time, and  $D$  is the diffusion coefficient set to  $1 \times 10^{-5}$  m<sup>2</sup>/s. The results can be seen in Figure 2.2-18 where the concentration 50 meter into the secondary continuum is plotted at a time of 101 days showing excellent agreement.

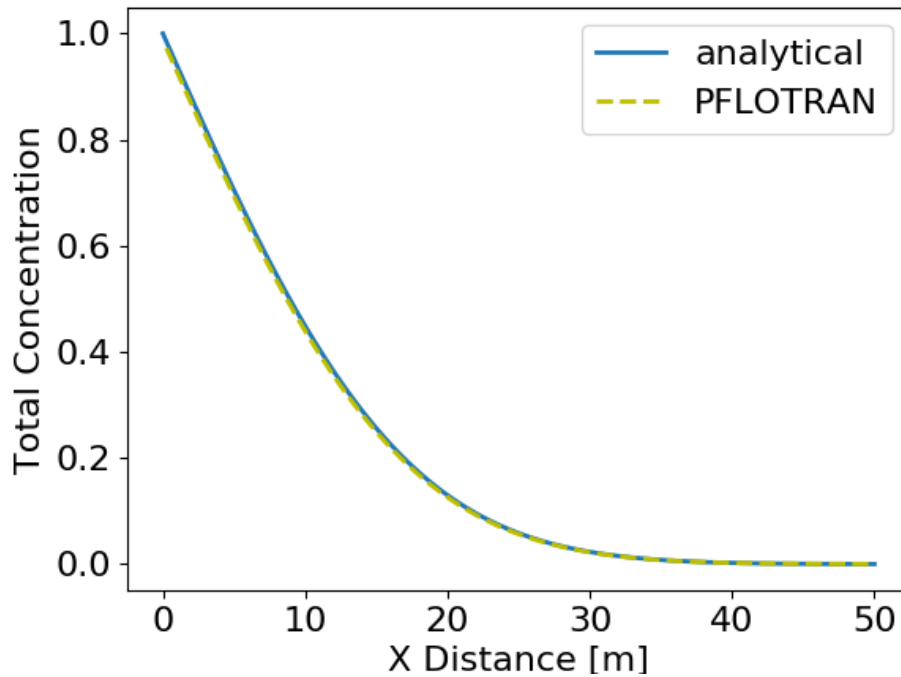


Figure 2.2-18 Analytical solution showing gas transport via diffusion in secondary continuum only, keeping primary continuum concentration constant

The next benchmark test is based on the analytical solution by Tang et al., 1981 for the problem of transport of a radionuclide in a single fixed-aperture fracture with diffusion into the rock matrix, where the rock matrix is assumed to be infinite. To obtain the transport equations with the same form as Tang et al., 1981 but including gas transport in the fracture and matrix, the governing equations of the primary continuum are defined as:

$$\frac{\partial}{\partial t} (\varphi_f (s^{aq,f} c^{aq,f} + s^g c^{g,f})) + \nabla \cdot (q^{aq} c^{aq,f} + q^g c^{g,f} - \varphi_f s^{aq,f} D_f^{aq} \nabla c^{aq,f} - \varphi_f s^{g,f} D_f^g \nabla c^g) = -\frac{\varphi_m}{b} \left( s_m^{aq} D_m^{aq} \frac{\partial c_m^{aq}}{\partial y} + s_m^g D_m^g \frac{\partial c_m^g}{\partial y} \right) \quad \text{Equation 2.2-128}$$

where  $b$  is the half fracture aperture [m]. And for the secondary continuum:

$$\frac{\partial}{\partial t} \varphi_m (s^{aq,m} c^{aq,m} + s^{g,m} c^{g,m}) + \nabla \cdot (-\varphi_m s^{aq,m} D_m^{aq} \nabla c^{aq,m} - \varphi_m s^{g,m} D_m^g \nabla c^{g,m}) = 0 \quad \text{Equation 2.2-129}$$

where it is assumed that transport in the secondary continuum only takes place from diffusion. Aqueous and gaseous species concentrations in primary and secondary continua are related through Henry's constant:

$$c^g = K c^l \quad \text{Equation 2.2-130}$$

Substituting Henry's relation yields:

$$\frac{\partial}{\partial t} \varphi_f (s^{aq,f} + K s^g) c^{aq,f} + \nabla \cdot ((q^{aq} + K q^g) c^{aq,f} - \varphi_f (s^{aq,f} D_f^{aq} - K s^{g,f} D_f^g) \nabla c^{aq,f}) = -\frac{\varphi_m}{b} (s_m^{aq} D_m^{aq} + K s_m^{g,m} D_m^g) \frac{\partial c_m^{aq}}{\partial y} \quad \text{Equation 2.2-131}$$

and

$$\frac{\partial}{\partial t} \varphi_m (s^{aq,m} + K s^{g,m}) c^{aq,m} + \nabla \cdot (-\varphi_m (s^{aq,m} D_m^{aq} + K s^{g,m} D_m^g) \nabla c^{aq,m}) = 0 \quad \text{Equation 2.2-132}$$

The Darcy velocity and diffusion coefficient can then be defined as:

$$q_{eff} = \frac{q^{aq} + K q^g}{s^{aq,f} + K s^{g,f}} \quad \text{Equation 2.2-133}$$

$$D_{eff} = \frac{s^{aq,f} D_f^{aq} + K s^{g,f} D_f^g}{s^{aq,f} + K s^{g,f}} \quad \text{Equation 2.2-134}$$

$$D'_{eff} = \frac{s^{aq,m} D_m^{aq} + K s^{g,m} D_m^g}{s^{aq,m} + K s^{g,m}} \quad \text{Equation 2.2-135}$$

$$D''_{eff} = \frac{s^{aq,m} D_m^{aq} + K s^{g,m} D_m^g}{s^{aq,m} + K s^{g,m}} \quad \text{Equation 2.2-136}$$

The transport equations for the primary continuum then become:

$$\frac{\partial}{\partial t} \varphi_f c^{aq,f} + \nabla \cdot (q_{eff} c^{aq,f} - \varphi_f D_{eff} \nabla c^{aq,f}) = -\frac{\varphi_m}{b} D'_{eff} \frac{\partial c_m^{aq}}{\partial y} \quad \text{Equation 2.2-137}$$

And for the secondary continuum:



$$\frac{\partial}{\partial t} \varphi_m c^{aq,m} + \nabla \cdot (-\varphi_m D_{eff}'' \nabla c^{aq,m}) = 0 \quad \text{Equation 2.2-138}$$

It is required that  $D'_{eff}=D''_{eff}$  for the analytical solution, resulting in equal saturation states in the primary and secondary continua. In addition, it is assumed  $\varphi_f=1$ . With these limitations, the conservation equations including gas transport are identical to the single-phase dual continuum transport equations with effective properties replacing the original values for advection and diffusion.

The analytical solution was coded in Python for comparison where material and fluid properties are listed in Table 2.2-12. The benchmark case is then modeled in PFLOTRAN using the slab geometry with a fracture length of 10 m and a matrix length of 80 m. A Dirichlet boundary condition was assumed at the inlet and modeled to 500 days. 100 cells were used to model the primary continuum where each cell had 200 secondary cells. Normalized concentration along the fracture and concentration in the matrix at 100 and 500 days can be seen in Figure 2.2-19 and Figure 2.2-20 where the DCDM model shows excellent agreement with the analytical solution in the fracture and matrix.

**Table 2.2-12 Parameters for modified Tang et al., 1981 benchmark solution**

Parameter	Value
Aqueous diffusion coefficient in fracture	$1.0 \times 10^{-9} \text{ m}^2/\text{s}$
Gas diffusion coefficient in fracture	$1.0 \times 10^{-5} \text{ m}^2/\text{s}$
Aqueous diffusion coefficient in matrix	$1.0 \times 10^{-9} \text{ m}^2/\text{s}$
Gas diffusion coefficient in matrix	$1.0 \times 10^{-5} \text{ m}^2/\text{s}$
Fracture porosity	1.0
Matrix porosity	0.01
Liquid saturation	0.1
Gas saturation	0.9
Aqueous linear velocity	0.09 m/d
Gas linear velocity	0.09 m/d
Half fracture width	$50 \times 10^{-6} \text{ m}$

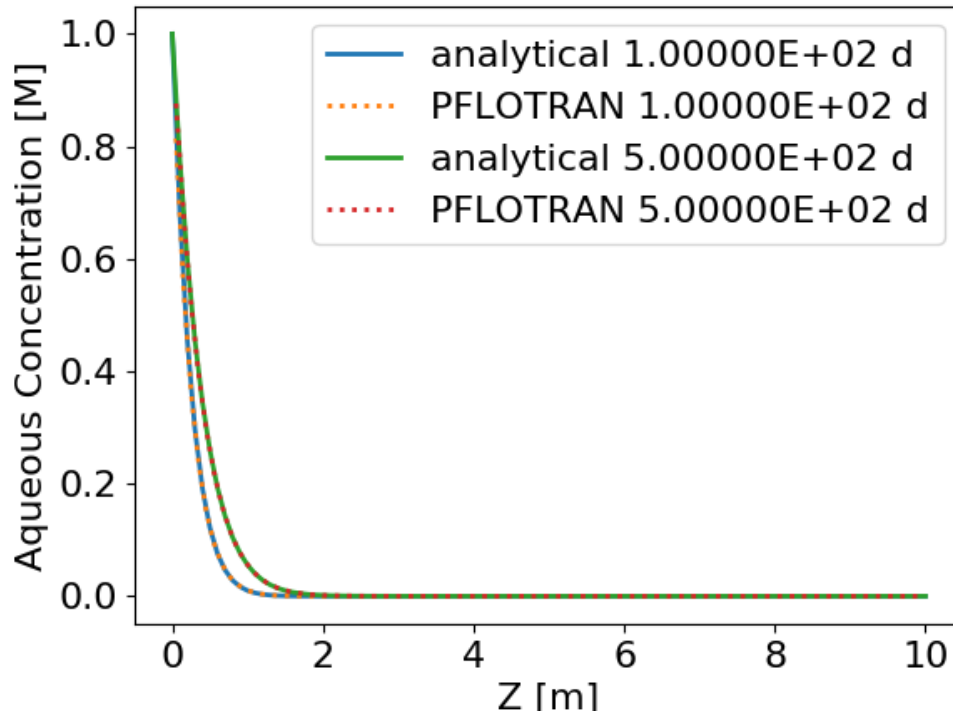


Figure 2.2-19 Modified Tang et al., 1981 (solid) comparison with PFLOTRAN (dotted) in the fracture at 100 and 5000 days.

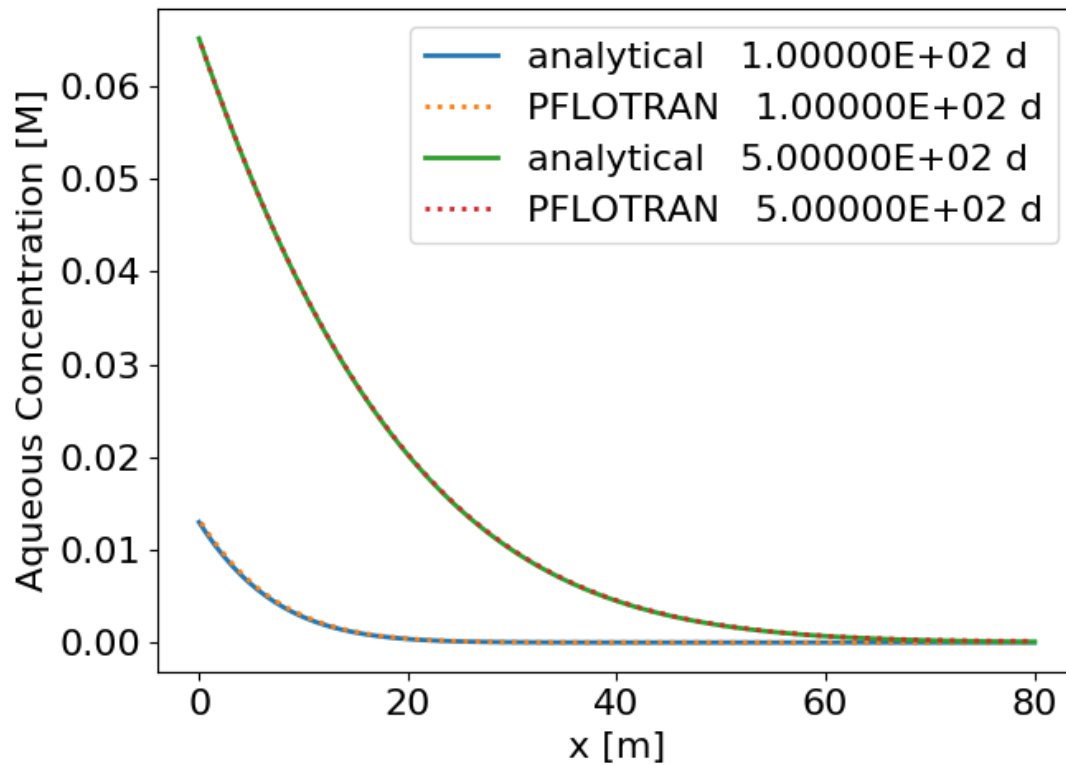


Figure 2.2-20 Modified Tang et al., 1981 (solid) comparison with PFLOTTRAN (dotted) in the matrix, 1 m down the fracture at 100 and 5000 days.

The multiple continuum model was then compared to an unstructured explicit grid modeled in PFLOTTRAN. The unstructured explicit grid simulated transport using only the primary continuum reactive transport model. The domain consisted of three cells designated as the “fracture” or primary domain and thirty cells designated as the “matrix” or secondary domain (Figure 2.2-21). Connections occurred between each of the fracture/primary cells and the corresponding secondary/matrix cells. Each matrix cell is only connected to the cell directly on the right or left to mimic the multiple continuum model in PFLOTTRAN. The same set up was used in a structured grid using the dual continuum model with slab geometry and 9 secondary cells designated to each primary continuum cell. Parameters used for this test can be seen in Table 2.2-13. A Dirichlet boundary condition was assumed at the inlet fracture cell and modeled to 100 days. Figure 2.2-22 and Figure 2.2-23 show comparison at the black and yellow star respectively, showing excellent agreement.

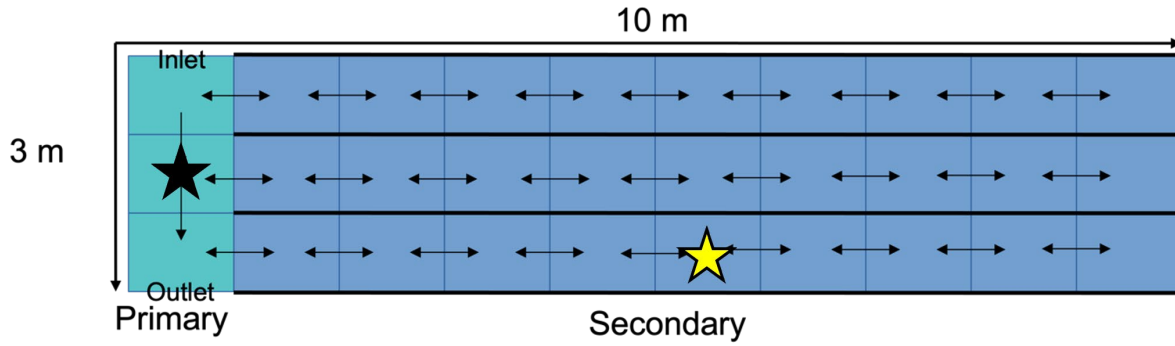


Figure 2.2-21 Domain set up for unstructured explicit grid. Primary represents fracture and secondary represents matrix.

Table 2.2-13 Parameters used for unstructured explicit grid comparison

Parameter	Value
Aqueous diffusion coefficient in fracture	$1.0 \times 10^{-5} \text{ m}^2/\text{s}$
Gas diffusion coefficient in fracture	$1.0 \times 10^{-9} \text{ m}^2/\text{s}$
Aqueous diffusion coefficient in matrix	$1.0 \times 10^{-9} \text{ m}^2/\text{s}$
Gas diffusion coefficient in matrix	$1.0 \times 10^{-5} \text{ m}^2/\text{s}$
Fracture porosity	1.0
Matrix porosity	0.01
Liquid saturation	0.4
Gas saturation	0.6
Linear velocity	0.0001 m/d

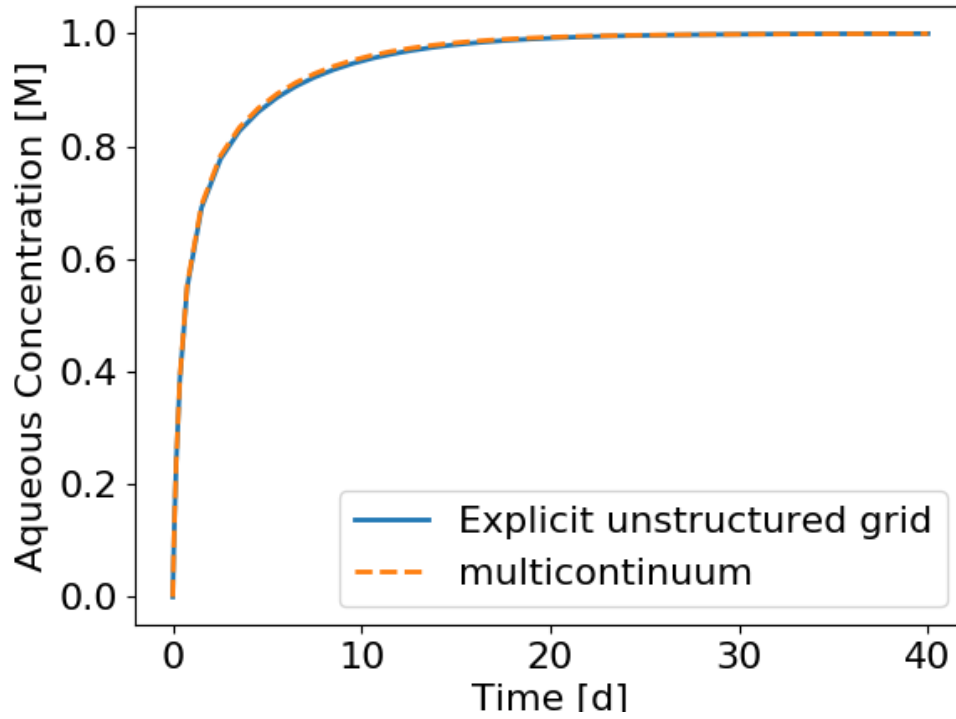


Figure 2.2-22 Comparison of aqueous concentration between the dual continuum model (orange dotted) and explicit unstructured grid (blue solid) at the fracture/primary cell denoted by the black star in Figure 2.2-21.

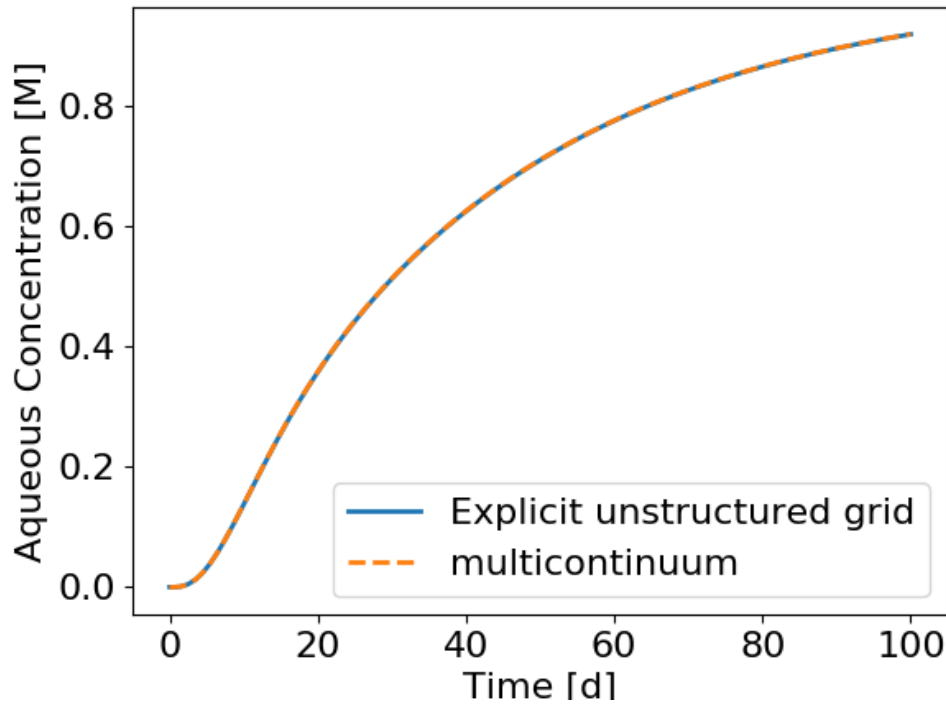


Figure 2.2-23 Comparison of aqueous concentration between the dual continuum model (orange dotted) and explicit unstructured grid (blue solid) at the matrix/secondary cell denoted by the yellow star in Figure 2.2-21.

## 2.2.7 Buffer Erosion and Canister Corrosion

The buffer erosion and canister corrosion (BECC) model is a performance assessment model capability intended for implementation in the GDSA PA Framework. Moreno et al. (2011) report the importance of including the effect of bentonite erosion where nuclear waste packages are placed such that they cross fractures in crystalline rock with fluid flowing around them. The BECC model developed in this report will be based on the models developed and used by SKB (Aakesson et al., 2010) and Posiva (Posiva, 2013) for the Forsmark and Olkiluoto repositories.

The primary goal of the BECC model is to simulate erosion of the buffer surrounding a waste package until the waste package surface is exposed to flowing groundwater and corrosion of the exposed waste package until the waste package is breached. The breach of the waste package will trigger the waste form degradation and radionuclide release model in PFLOTRAN (in the Waste Form Process Model). The aim of the BECC model is to add to PFLOTRAN's more physics-based models as compared to, e.g., a stochastic model that samples on waste package breach time. The BECC model implementation plan includes three submodels: virtual buffer erosion model, buffer cell erosion model, and the canister corrosion model.

The virtual buffer erosion model calculates the amount of buffer eroded at each time step and the volume of buffer erosion needed to expose the canister. The mathematical formulation of this model is primarily taken from Neretnieks et al. (2017, Section 4). This model does not determine the physical property (e.g., porosity, permeability) response to removing buffer from the buffer cells in a model mesh; hence the word "virtual". That function is the purpose of the buffer *cell* erosion model.

The buffer cell erosion model determines how to modify the buffer properties in the cells surrounding the canisters to reflect buffer erosion calculated by the virtual buffer erosion model. Finally, the canister corrosion model calculates the cumulative canister corrosion at each time step and compares this value to the amount of corrosion needed to fail the canister, at which point failure is initiated in the waste form process model. The mathematical formulation of this model is primarily taken from Posiva (2013, Sections 6.11 and 6.19).

### 2.2.7.1 Buffer Erosion and Canister Corrosion (BECC) conceptual model

The BECC conceptual model is shown in Figure 2.2-24. When groundwater ionic strength is below a defined threshold, the buffer in a deposition borehole erodes due to groundwater from an intersecting fracture. Buffer erosion eventually exposes the waste package surface to flowing groundwater. The integrity of the buffer depends on the buffer properties and the velocity of groundwater flowing in the fracture from the flow and transport simulation. After the exposure, corrosive agents like hydrogen sulfide in the flowing groundwater attack the exposed waste package material. The canister breaches after prolonged attack of the incoming reactant corroding the canister. The conceptual model includes a series of the two concepts: buffer erosion and canister corrosion. The model is based on the chemical erosion and corrosion models summarized in Posiva (2013, Sections 6.11 and 6.19) with updates to the buffer erosion model generally in accordance with Neretnieks et al. (2017).

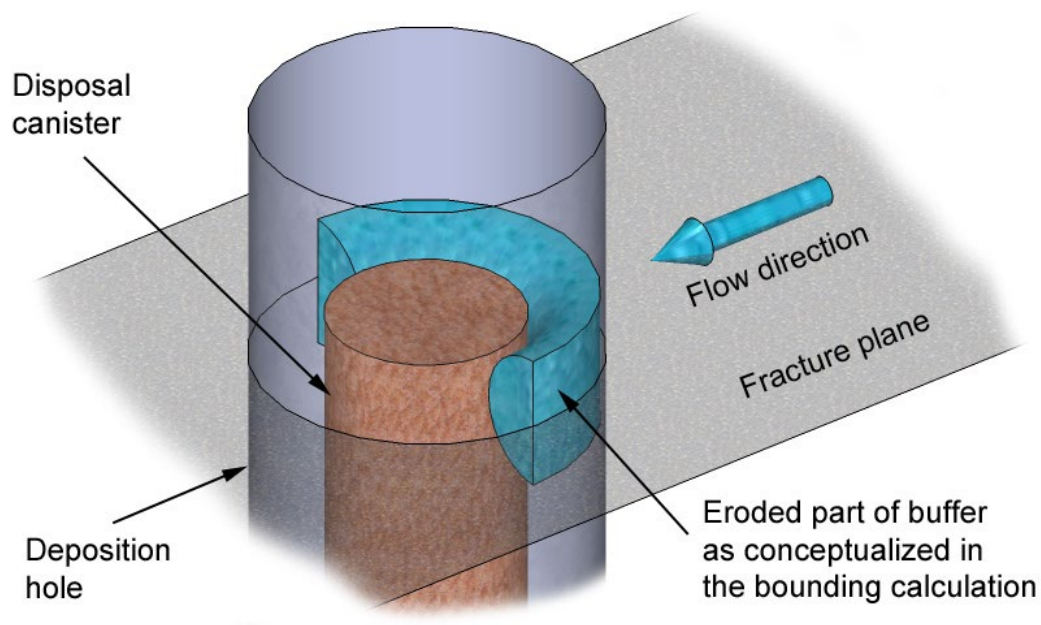


Figure 2.2-24 Conceptual model of buffer erosion due to a flowing fracture (Fig 6-108, Posiva 2013)

### 2.2.7.2 *Virtual Buffer Erosion Model*

As shown in Figure 2.2-24, buffer intrudes into the fracture and potentially erodes at the expanding rim of the intrusion at each time step. The rate of buffer loss during a given time step depends on the ionic strength of the groundwater, groundwater velocities in the intersecting fracture, fracture properties, and smectite behavior. The model of Neretnieks et al. (2017), adopted here, involves three primary processes:

**Buffer intrusion** – Buffer intrusion is the gradual movement of smectite particles as a gel/sol from the borehole into the fracture due to swelling pressure in the borehole. Buffer intrusion always occurs. However, when groundwater ionic strength exceeds a value for significant diffusion of smectite particles in water (such as might occur during a non-glacial period), buffer intrusion is the only major process accounting for the loss of buffer from a borehole.

**Buffer erosion by seeping water** – Buffer loss is enhanced by erosion when the water velocities are high and the ionic strength of the groundwater at the rim of the buffer intrusion is low enough for significant aqueous diffusion of smectite particles. Overall buffer loss under these conditions involves calculating the extent of the intruding rim considering the shear forces of flowing groundwater and the ionic strength-dependent aqueous diffusivity of smectite particles.

**Buffer erosion by sedimentation** – Sedimentation also requires low ionic strength groundwater. Sedimentation is the loss of buffer at the rim due to gravitational forces and inclined fractures. As the angle of the fracture increases, there is an increasing propensity for small smectite agglomerates to be released from the rim of the intrusion. This process is modeled to be independent of water velocity and limited by fracture aperture. For small fracture apertures (e.g., less than 0.1 mm), viscous forces can inhibit sedimentation.

The goal of the virtual buffer erosion model is to assist in determining the time at which buffer erosion exposes the canister to more rapidly flowing groundwater. This is the first model in development

for this work; the buffer cell erosion model and canister corrosion model are still in the planning stage of implementation.

### **2.2.7.3 Implementation Plan for Virtual Buffer Erosion Model**

#### **1. Implement intersecting fracture code for virtual buffer erosion model**

For input to the virtual buffer erosion (VBE) model, we are building a capability in `mapDFN.py` that searches for and identifies all waste package cell locations in the repository where connected fractures exist in the rock prior to excavation (later, when the buffer cell erosion model is being implemented, we will expand that search to include buffer cell locations). We will then automate a way to use that information to record fracture apertures and to monitor fracture flow velocities and concentrations of Na, Ca, and hydrogen sulfide (and potentially other dissolved constituents) over time at those locations from flow and transport simulations of the pre-excavated rock. The collected information shall be formatted for use as an external data file for the VBE model to be implemented in PFLOTRAN. Note: In the pre-excavated rock simulations, heat sources and drifts near borehole-emplaced WPs may be simulated.

#### **2. Implement virtual buffer erosion model in PFLOTRAN**

In the `WASTE_FORM` process model in PFLOTRAN, we will create a new canister degradation sub-block, e.g., `BUFFER_EROSION_CANISTER_DEGRADATION`. We will implement the virtual buffer erosion (VBE) model part here. The VBE model will be a function of the fracture flow velocity, concentrations of Na, Ca, and hydrogen sulfide, and other inputs as needed (e.g., borehole radius). Many of the inputs will be provided by the intersecting fracture code implemented in `mapDFN.py`. Some inputs will be user-provided in the PFLOTRAN input file. The model will use all inputs to calculate the mass of buffer that must be eroded to expose the waste package, the buffer erosion rate for the time step, and the cumulative buffer volume eroded. The code will record at each time step the following to an output file: buffer erosion rate, cumulative volume of buffer eroded, and interpolated time when the WP becomes exposed to flowing groundwater. Virtual buffer only erodes when the groundwater contains Na and Ca concentrations below a user-provided threshold. When the cumulative virtual buffer eroded reaches the critical value needed to expose the waste package, the VBE model terminates, and the VBE-enhanced canister degradation model turns on.

#### **3. Implement VBE-enhanced canister degradation model in PFLOTRAN**

In the new canister degradation sub-block, we will implement a canister degradation model like the copper corrosion model used by SKB. This implementation will allow for flexible description of canister materials (i.e., not just a copper canister). Inputs include fracture flow rate, hydrogen sulfide concentration, canister wall thickness, canister wall density, etc. The model is turned on as soon as the critical volume of buffer erodes. If that time happens in the middle of a time step, canister wall degradation that occurs during that time step will be determined by linear interpolation. The code will record at each time step the following to an output file: canister degradation rate (m/yr), cumulative canister thickness degraded (m), and interpolated time when the waste package breaches. This file can be the same one as the one used to record virtual buffer erosion outputs. Upon waste package breach, the



model will allow the waste package to be fully breached as if there were no canister at all. Partial waste package performance can be added later as needed.

### 2.2.8 Salinity-Dependent Equations of State

The addition of dissolved salt (sodium chloride) changes the density, enthalpy, viscosity, and saturation pressure of the fluid. In a multi-phase system, these changes become particularly important in reaching an accurate simulation solution. Of primary importance to pore water brines is the solubility of salt in water. We use the formulation described by Sparrow (2003) to find the temperature-dependent solubility (Figure 2.2-25).

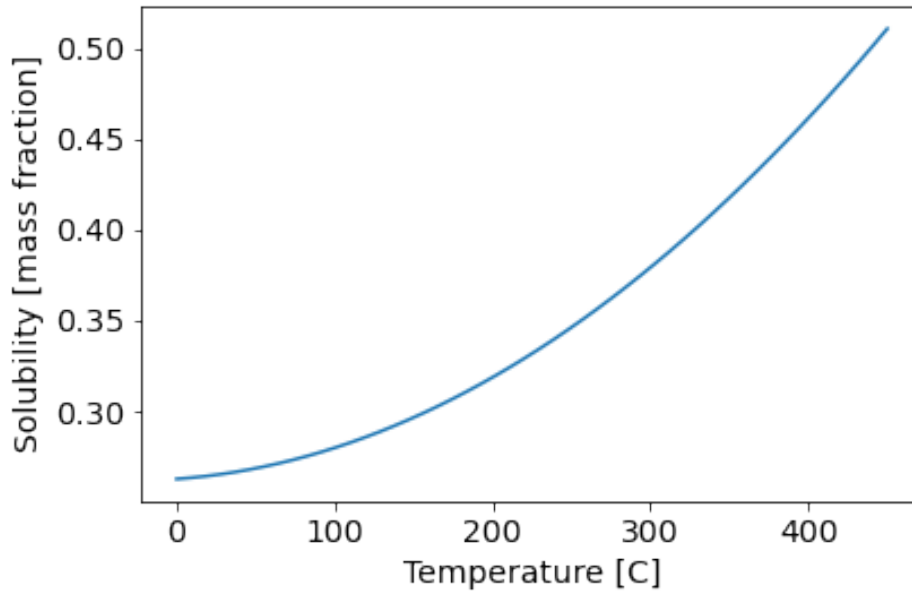


Figure 2.2-25 Solubility of salt in water as a function of temperature.

The solubility,  $X_{sat}$  is expressed as a function of temperature,  $T(^{\circ}\text{C})$ :

$$X_{sat} = 0.2628 + 62.75 \times 10^{-6}T + 1.084 \times 10^{-6}T^2 \quad \text{Equation 2.2-139}$$

The mass fraction used in the Sparrow equations of state can be related to molality by the following equation:

$$X = \frac{mM_{NaCl}}{1000+mM_{NaCl}} \quad \text{Equation 2.2-140}$$

where  $X$  is the mass fraction of salt,  $m$  is the molality of the solution (mol NaCl/kg  $\text{H}_2\text{O}$ ) and  $M_{NaCl}$  is the molar mass of NaCl (58.443 g/mol).

The density of brine is a function of temperature, pressure, and concentration of salt (Figure 2.2-26). Two options for density computation are available: Sparrow (2003), and Batzle and Wang (1992).

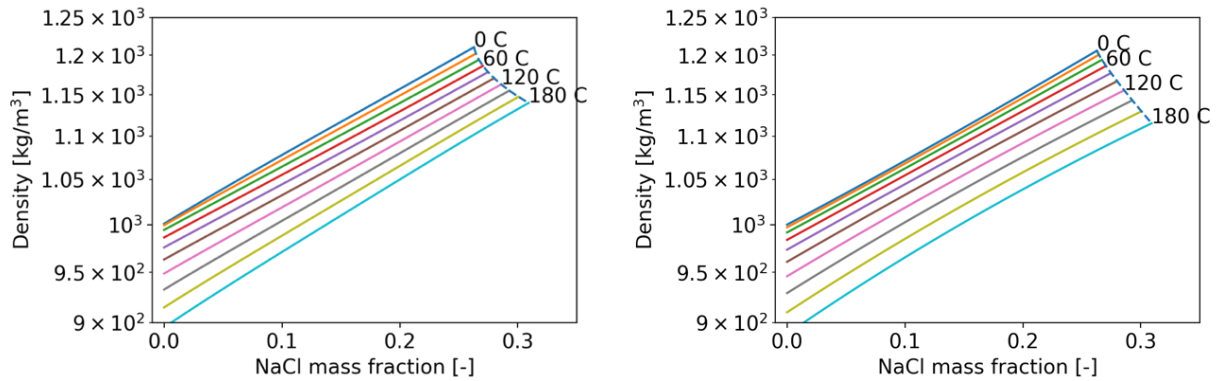


**Figure 2.2-26 Density of brines as a function of mass fraction and temperature (Left: Sparrow, Right: Batzle and Wang). The dashed line indicates the density of a brine with a salt concentration at solubility.**

The Sparrow equation for density,  $\rho$  ( $\text{kg/m}^3$ ), is a function of salt concentration,  $X$  (mass fraction) and temperature,  $T$  ( $^{\circ}\text{C}$ ):

$$\rho = A + BT + CT^2 + DT^3 + ET^4 \quad \text{Equation 2.2-141}$$

where:

$$A = (1.001 + 0.7666X - 0.0149X^2 + 0.2663X^3 + 0.8845X^4) \times 10^3$$

$$B = 0.0214 - 3.496X + 10.02X^2 - 6.56X^3 - 31.37X^4$$

$$C = (-5.263 + 39.87X - 176.2X^2 + 363.5X^3 - 7.784X^4) \times 10^{-3}$$

$$D = (15.42 - 167X + 980.7X^2 - 2573X^3 + 876.6X^4) \times 10^{-6}$$

$$E = (-0.0276 + 0.2978X - 2.017X^2 + 6.345X^3 - 3.914X^4) \times 10^{-6}$$

The Batzle and Wang formulation first calculates pure water density  $\rho_w$ , ( $\text{g/cm}^3$ ) as a function of pressure  $P$  (MPa), and temperature  $T$  ( $^{\circ}\text{C}$ ):

$$\rho_w = 1 + 1 \times 10^{-6}(-80T - 3.3T^2 + 0.00175T^3 + 489P - 2TP + 0.016T^2P - 1.3 \times 10^{-5}T^3P - 0.333P^2 - 0.002TP^2) \quad \text{Equation 2.2-142}$$

Then uses the pure water density to calculate a brine density  $\rho_b$ , ( $\text{g/cm}^3$ ) as a function of pressure, temperature, and salt concentration,  $S$  ( $\text{ppm}/1 \cdot 10^6$ ):

$$\rho_b = \rho_w + S \left( 0.668 + 0.44S + 1 \times 10^{-6} (300P - 2400PS + T(80 + 3T - 3300S - 13P + 47PS)) \right) \quad \text{Equation 2.2-143}$$

A correction was made to the original Batzle and Wang density subroutine, which incorrectly computed the molar density of water from the mass density,  $\rho_b$ , without removing the salt component. Molar density is now calculated as follows:

$$\rho_{w,molar} = \frac{\rho_b(1-S)}{M_{H_2O}} \quad \text{Equation 2.2-144}$$

where  $\rho_{w,molar}$  is the molar density of water ( $\text{kmol}/\text{m}^3$ ),  $\rho_b$  is the brine density ( $\text{kg}/\text{m}^3$ ),  $S$  is the salt mass fraction ( $\text{ppm}/1 \cdot 10^6$ ), and  $M_{H_2O}$  is the molar mass of water ( $\text{kg}/\text{kmol}$ ).

Vapor pressure lowering with increased solute concentration is an important consideration of multi-phase flow near the boiling point. Increased concentrations of salt in brine lower the vapor pressure, increasing the boiling point of the water (Figure 2.2-27). We have implemented two options for vapor pressure calculation: Sparrow (2003) and Haas (1976).

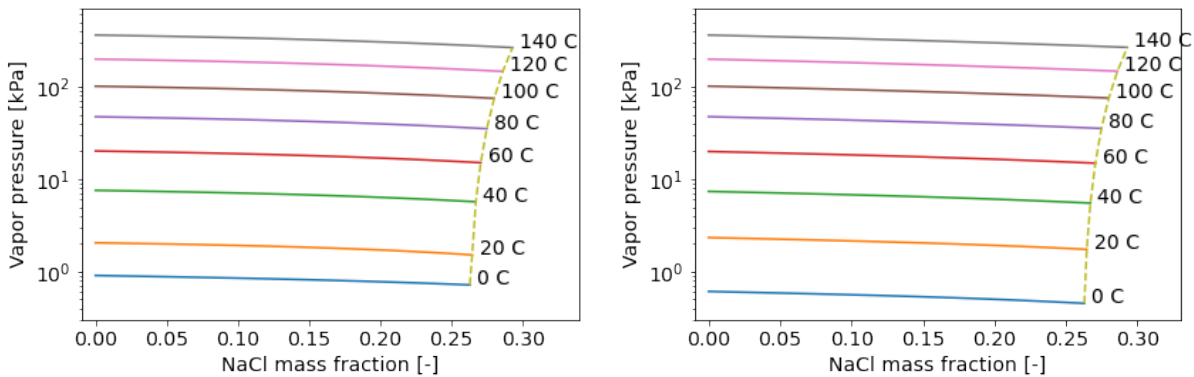


**Figure 2.2-27 Vapor pressure as a function of salt concentration (Left: Sparrow, Right: Haas). Vapor pressure of brines decreases with increased mass fraction. The vapor pressure lowering with increased salt concentration raises the boiling point of water. The dashed line indicates vapor pressure at solubility.**

The Sparrow formulation calculates vapor pressure,  $P_{vap}$  (MPa) as a function of temperature,  $T$  ( $^{\circ}\text{C}$ ) and dissolved salt concentration,  $X$  (mass frac.):

$$P_{vap} = A + BT + CT^2 + DT^3 + ET^4 \quad \text{Equation 2.2-145}$$

where:

$$A = (0.9083 - 0.569X + 0.1945X^2 - 3.736X^3 + 2.82X^4) \times 10^{-3}$$

$$B = (-0.0669 + 0.0582X - 0.1668X^2 + 0.6761X^3 - 2.091X^4) \times 10^{-3}$$

$$C = (7.541 - 5.143X + 6.482X^2 - 52.62X^3 + 115.7X^4) \times 10^{-6}$$

$$D = (-0.0922 + 0.0649X - 0.1313X^2 + 0.8024X^3 - 1.986X^4) \times 10^{-6}$$

$$E = (1.237 - 0.753X + 0.1448X^2 - 6.964X^3 + 14.61X^4) \times 10^{-9}$$

The Haas formulation first relates the temperature of the brine,  $T_s$  (°C), to the temperature of H<sub>2</sub>O liquid,  $T_0$  (°C), at the same pressure, where  $x$  is the molality (mol salt/kg solution):

$$\ln(T_0) = m \ln(T_x) + c \quad \text{Equation 2.2-146}$$

where:

$$m = (a + bT_x)^{-1}$$

$$a = 1.0 + a_1x + a_2x^2 + a_3x^3$$

$$b = b_1x + b_2x^2 + b_3x^3 + b_4x^4 + b_5x^5$$

$$c = 0$$

The vapor pressure,  $p$  (bar), is then calculated as a function of the H<sub>2</sub>O liquid temperature,  $T_0$  (°C):

$$\ln(p) = e_0 + \frac{e_1}{z} + \frac{e_2w}{z} (10^{e_3w^2} - 1.0) + e_4 10^{e_5y^{1.25}} \quad \text{Equation 2.2-147}$$

where:

$$w = z^2 - e_6$$

$$y = 647.27 - T_0$$

$$z = T_0 + 0.01$$

The constants used in the Haas vapor pressure equations are presented in Table 2.2-14.

Table 2.2-14 Constants for vapor pressure calculation by Haas.

Constant	Value
$a_1$	$5.93582 * 10^{-6}$
$a_2$	$-5.19386 * 10^{-5}$
$a_3$	$1.23156 * 10^{-5}$
$b_1$	$1.15420 * 10^{-6}$
$b_2$	$1.41254 * 10^{-7}$
$b_3$	$-1.92476 * 10^{-8}$
$b_4$	$-1.70717 * 10^{-9}$
$b_5$	$1.05390 * 10^{-10}$
$e_0$	12.50849
$e_1$	$-4.616913 * 10^3$
$e_2$	$3.193455 * 10^{-4}$
$e_3$	$1.1965 * 10^{-11}$
$e_4$	$-1.013137 * 10^{-2}$
$e_5$	$-5.7148 * 10^{-3}$
$e_6$	$2.9370 * 10^5$

We note that the third and fourth terms,  $\left(\frac{e_2 w}{z} (10^{e_3 w^2} - 1.0)\right)$ , of the vapor pressure equation are multiplied instead of added (Haas, 1976, Eq. 6). This is corroborated in a paper by the same author (Haas, 1971, Eq. 10).

Liquid enthalpy is also a function of salt concentration (Figure 2.2-28). Here, we use the formulation of Sparrow (2003), where  $h$  is specific enthalpy (kJ/kg),  $T$  is temperature ( $^{\circ}\text{C}$ ), and  $X$  is mass fraction of dissolved salt in water (kg salt/kg solution).

$$h = A + BT + CT^2 + DT^3 + ET^4 \quad \text{Equation 2.2-148}$$

where:

$$A = (0.0005 + 0.0378X - 0.3682X^2 - 0.6529X^3 + 2.89X^4) \times 10^3$$

$$B = 4.145 - 4.973X + 4.482X^2 + 18.31X^3 - 46.41X^4$$

$$C = 0.0007 - 0.0059X + 0.0854X^2 - 0.4951X^3 + 0.8255X^4$$

$$D = (-0.0048 + 0.0639X - 0.714X^2 + 3.273X^3 - 4.85X^4) \times 10^{-3}$$

$$E = (0.0202 - 0.2432X + 2.054X^2 - 8.211X^3 + 11.43X^4) \times 10^{-6}$$

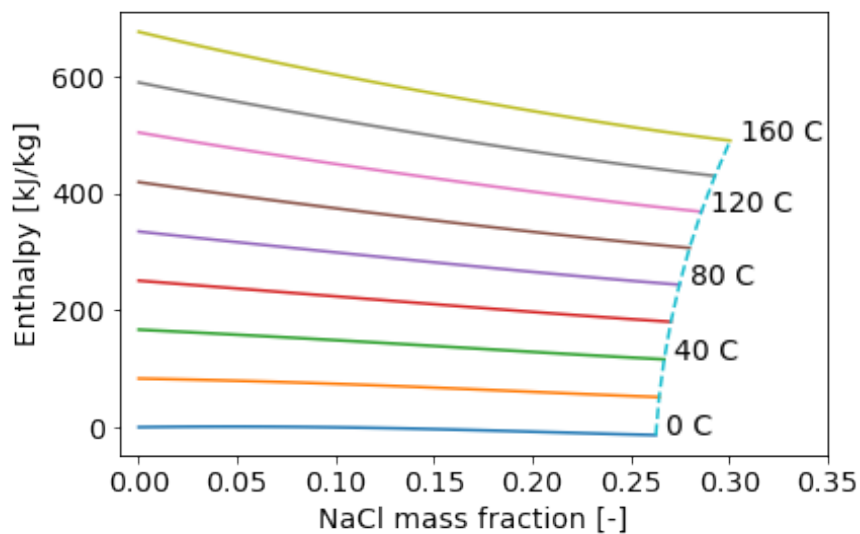


Figure 2.2-28 Specific enthalpy as a function of salt concentration.

### 2.2.9 Fully-Coupled Solute Mass Balance

In freshwater aquifers, aqueous chemical species are typically light enough and found in low enough concentrations as to not significantly affect the flow properties of the water solvent, like density and viscosity. This concept forms the basis of a justification for sequentially coupling fluid flow and reactive transport in PFLOTTRAN. If the transport primary solution variables do not significantly affect the flow primary solution variables, then solving both the flow and transport solutions can oftentimes be more effectively achieved through sequential coupling.

One exception to this is the case of a brine pore water system. If the pore water contains salt (as exemplified by pore water contained in a salt host rock where the rock itself can dissolve into the water), salt dissolves in high enough concentrations to meaningfully affect the density, viscosity, and saturation pressure of the pore water. Considering this feedback between the solute and the liquid flow properties is therefore very important. Until now, modeling salinity effects on flow properties required modeling salinity as part of the transport equations and then handing off updated salinity to the flow solution at sync points under the standard sequential flow and transport coupling scheme. Since these two systems are much more tightly coupled when salt is a solute, sequential coupling in this manner requires taking very small time steps in order to avoid numerical artifacts. The developments described in this section for fully coupling a solute in GENERAL mode are currently still in testing stages and are not yet available in the master branch of the code.

We build upon GENERAL (two-component, multi-phase air/water flow) mode to accommodate solute transport as a third component either dissolved in the liquid phase or as a solid precipitate. GENERAL mode, in its prior formulation, implicitly solves two component mass balance equations (Equation 2.2-149):

$$\frac{\partial}{\partial t} \phi (s_l \rho_l x_i^l + s_g \rho_g x_i^g) + \nabla \cdot (\mathbf{q}_l \rho_l x_i^l + \mathbf{q}_g \rho_g x_i^g - \phi s_l D_l \rho_l \nabla x_i^l - \phi s_g D_g \rho_g \nabla x_i^g) = Q_i \quad \text{Equation 2.2-149}$$

and an energy balance equation (Equation 2.2-150):

$$\sum_{\alpha=l,g} \left( \frac{\partial}{\partial t} (\phi s_\alpha \rho_\alpha U_\alpha) + \nabla \cdot (\mathbf{q}_\alpha \rho_\alpha H_\alpha) \right) + \frac{\partial}{\partial t} ((1 - \phi) \rho_r C_p T) - \nabla \cdot (\kappa \nabla T) = Q \quad \text{Equation 2.2-150}$$

for components  $i$  = water, air and phases  $\alpha$  = liquid, gas.

Our newly implemented, fully implicit solute transport mode includes an additional solute component mass balance equation (Equation 2.2-151):

$$\frac{\partial}{\partial t} \phi (s_l \rho_l x_{solute}^l + s_s \rho_s x_{solute}^s) + \nabla \cdot (\mathbf{q}_l \rho_l x_{solute}^l - \phi s_l D_l \rho_l \nabla x_{solute}^l) = Q_{solute} \quad \text{Equation 2.2-151}$$

In our new formulation, we assume that the vapor pressure of the solute is negligible, and therefore only present in the liquid phase. The solute can also form a solid precipitate phase ( $\alpha = s$ ), which is immobile in the pore space. Diffusion through the solid phase is considered negligible on the timescales used in our simulations and is therefore not present in this mass balance equation.



Primary variable switching is used to track phase transitions. The phase states used depend on whether the rock matrix is comprised of a soluble or insoluble material. For example, a quartz sandstone rock matrix is largely insoluble in water, therefore the possible phase states are any combination of liquid, gas, and solid precipitate. The phase states and primary variables associated with the phase state are presented in Table 2.2-15.

A halite rock matrix, on the other hand, readily dissolves in water, which changes the porosity of the rock matrix. In the case of a soluble halite rock matrix, the concentration of salt in the pore water is held at solubility (Equation 2.2-139), and as salt comes out of solution, or the rock matrix dissolves, the porosity changes.

**Table 2.2-15 Phase states and corresponding primary variables for an insoluble rock matrix.**

State	Primary variables
Liquid	$P_l, X_{air}, X_s, T$
Gas	$P_g, P_{air}, T$
Liquid/Gas	$P_g, P_{air}, X_s, T$
Liquid/Precipitate	$P_l, X_{air}, S_p, T$
Gas/Precipitate	$P_g, P_{air}, S_p, T$
Liquid/Gas/Precipitate	$P_g, S_g, S_p, T$
Precipitate	$P_g, T, -, -$

**Table 2.2-16 Phase states and corresponding primary variables for a soluble rock matrix.**

State	Primary variables
Liquid	$P_l, x_{air}, \phi, T$
Gas	$P_g, P_{air}, \phi, T$
Liquid/Gas	$P_g, P_{air}, \phi, T$

To facilitate simulation of a wider variety of problems, mixed (Neumann + Dirichlet) boundary conditions have been implemented. The density-driven flow (Elder) problem in Section 2.2.9.1 requires a Neumann condition for mass and energy flux, coupled with Dirichlet solute concentration. The soluble rock matrix (Olivella) problem in Section 2.2.9.2 requires constant temperature boundary conditions applied to a closed system (Neumann mass flux).

### 2.2.9.1 Density-Driven Flow

Density-driven flow occurs when a denser fluid overlies a less dense fluid. This type of convection occurs frequently in geologic systems, such as in mantle flows, CO<sub>2</sub> sequestration, and saltwater intrusion. Saltwater intrusion initiates density-driven convection when a dense brine overlies a less dense region of fresh water. The Elder problem is a classic benchmarking problem (Voss & Souza, 1987) that simulates saltwater intruding a freshwater aquifer, initiating density-driven convection and solute transport into the freshwater aquifer.

The system and boundary conditions are displayed in Figure 2.2-28. The dimensions of the system are 600 m length, and 150 m height (4:1 L:H ratio). A constant concentration (Dirichlet) boundary of  $x_{\text{salt}} = 0.28$  is set at the center 100 m of the top boundary, and a constant concentration of  $x_{\text{salt}} = 0$  is set along the entire bottom boundary. Constant (Dirichlet) pressure ( $p = 101325$  Pa) boundary conditions are set at the top-most corner cells. No-flux (Neumann) conditions are prescribed along all boundaries. The grid is discretized with 280 grid cells in the x direction, and 70 grid cells in the z direction, with  $dx = dz = 2.14$  m.

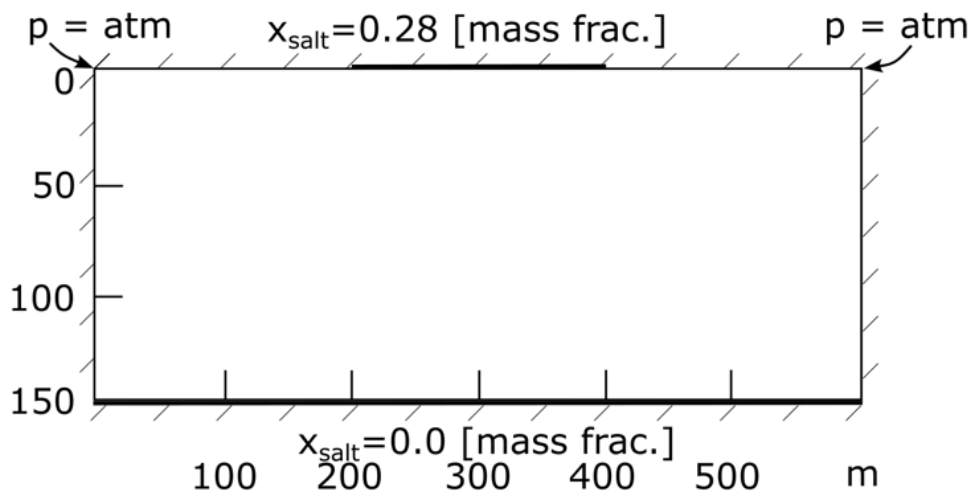


**Figure 2.2-29 Schematic of the Elder problem. The system has a length to height ratio of 4:1, constant concentration boundaries on the bottom and top, constant pressure boundaries at the top corners, and no-flux boundaries on all sides.**

Here, we compare the fully implicit implementation of solute transport with flow and sequentially coupled solute transport (Figure 2.2-29). The salt concentration is displayed in the figure, with 20% and 60% concentration contours overlaid. The 20% and 60% concentration contours of the Elder problem described by Voss and Souza (1987) are displayed in black. The Elder problem finds its origins in an experiment of a Hele-Shaw cell heated from below (Elder, 1967), where density-driven flow occurs by the temperature differences in the system. This was implemented as a numerical test problem with by inverting the system, and by having concentration, rather than temperature, driving density changes.

The initial difference between the fully implicit and sequentially coupled solutions are minimal. Density-driven instabilities are first observed at the edge of the system, consistent with the Elder problem. As the fingers grow, however, the solutions diverge as new unstable fingers develop at 4 y. The fully implicit solution more closely matches the Elder problem solution, with a single column of highly-concentrated brine developing by the end of 20 y.

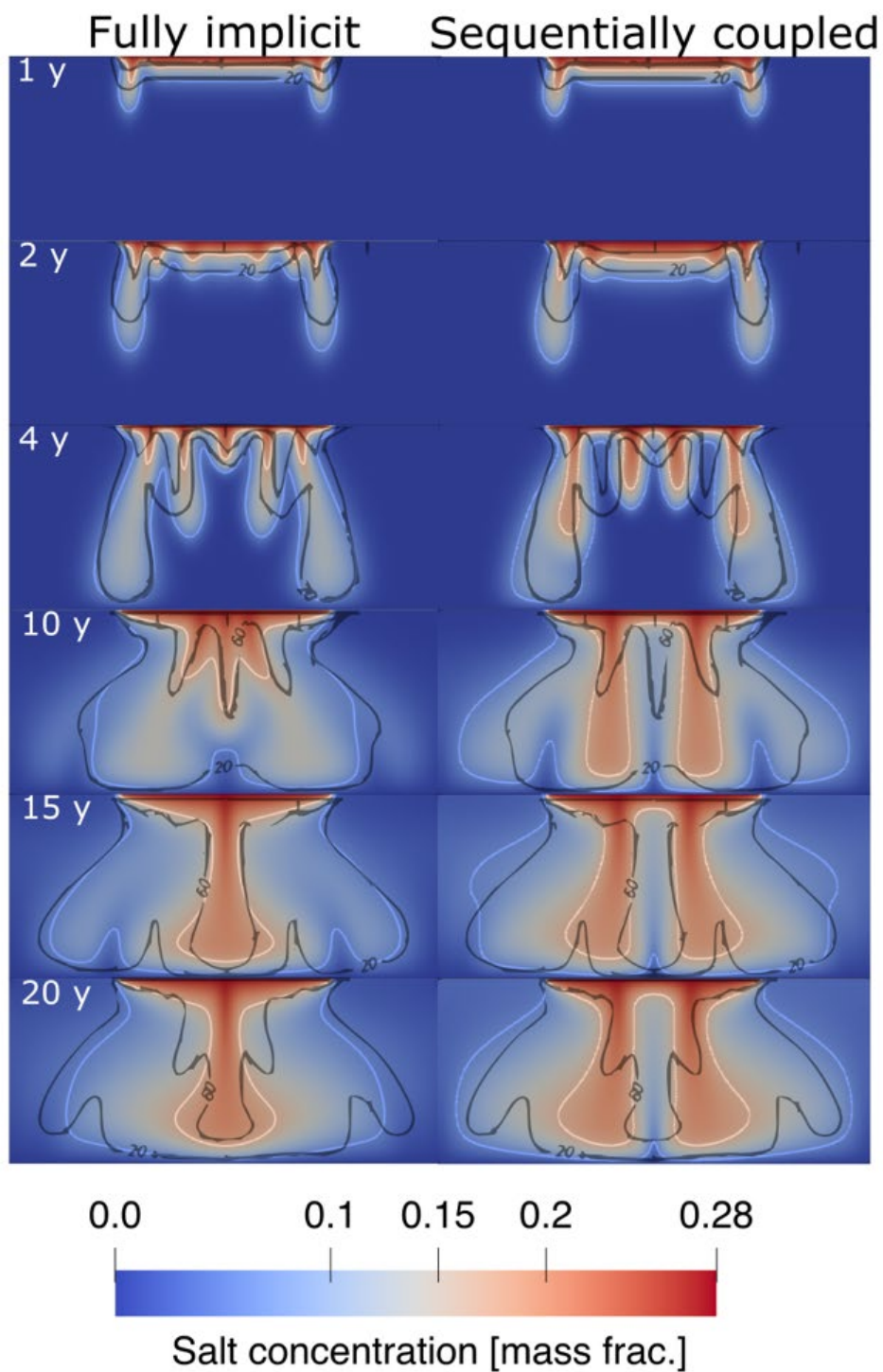


Figure 2.2-30 Comparison of density-driven flow between a fully implicit solute implementation and a sequentially coupled flow and transport implementation. Concentration contours of 60% (yellow) and 20% (blue) of the maximum concentration (0.28 mass frac.) are displayed, along with a comparison to the concentration contours from the Voss and Souza (Voss & Souza, 1987) implementation (black).

Density-driven convection problems are highly sensitive to differences in density calculation, grid discretization, time-stepping, among other issues. The closer match observed between the fully implicit and the solution in the Elder problem is not an indictment of the sequentially coupled implementation, but rather shows qualitatively that they arrive at a similar solution to the Elder problem. A closer match between either implementation and the Elder solution could be achieved by closely matching the density function, timesteps used, and the grid discretization.

### 2.2.9.2 *Soluble Rock Matrix*

Multi-phase fluid flow coupled with a temperature gradient in a system with a soluble rock matrix is a complex problem involving evaporation and condensation of water vapor, liquid, gas, and heat flux, along with dissolution and precipitation of the rock matrix. This modeling capability is germane to nuclear waste disposal in domal and bedded salt, where heat generated by the waste package induces heat and mass transfer.

A common benchmark problem testing mass and heat transfer, coupled with porosity changes in a granular salt system was introduced by Olivella et al., (1994). The system is discretized as a 0.5 m, 1D cartesian system, initialized at a constant temperature of 20 °C, porosity of 30%, water saturation of 30%, and gas saturation of 70%. Constant (Dirichlet) temperature boundary conditions of 85 °C and 5 °C are applied to the left and right boundaries, respectively. As the original experiment was a closed system, a zero mass flux (Neumann) boundary condition is applied to both the left and right boundaries. The simulation is performed over a period of 60 days, with 1-day timesteps.

The increased temperature at the left boundary causes evaporation of the water, driving salt precipitation and porosity decrease towards the left side of the system. The water vapor advects towards the right side of the system, where it condenses, partially dissolving the halite and increasing the porosity (Olivella et al., 2011).

We present here the preliminary results of porosity evolution (Figure 2.2-31) of the Olivella benchmark problem. We note that the results here do not identically match those found in the original benchmark problem but do follow the general trend observed in the study. Proper simulation of this problem, however, should not match the results found in Olivella et al., (2011), as mass was not conserved in the experiments. The experimental setup was not truly a closed system, likely due to a poor seal, with an additional 147% brine content added by the end of the experiment (Johnson et al., 2018).

The temperature gradient within the system reaches steady state within the first timestep (1 day). The porosity of the hot end of the system (left side) decreases to nearly 0% by the end of 60 days. This porosity change propagates through the system, with a slightly elevated porosity between 0.0 and 0.1 m due to evaporation and condensation in lower-temperature regions.

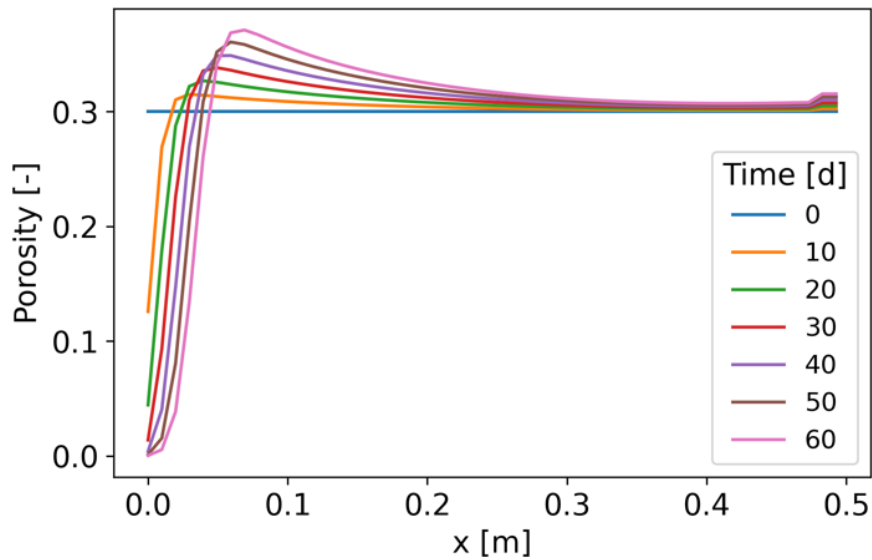


**Figure 2.2-31 Porosity evolution in the Olivella et al. (2011) benchmark problem.**

The porosity change is largely driven by the fluid flux, displayed in Figure 2.2-32. The evaporation and flux of water vapor occurs from the hot (left) side to the cold (right) side of the domain. Brine flows in the opposite direction, from the cold (right) side to the hot (left) side. The relative magnitudes of the fluxes provide insight to the main driving force of porosity decrease in this system. As the gas velocity is nearly three orders of magnitude higher than the liquid velocity, the evaporation and advection of water vapor removes water from the hot side of the system faster than the water flux in the opposite direction can re-saturate and dissolve the rock.

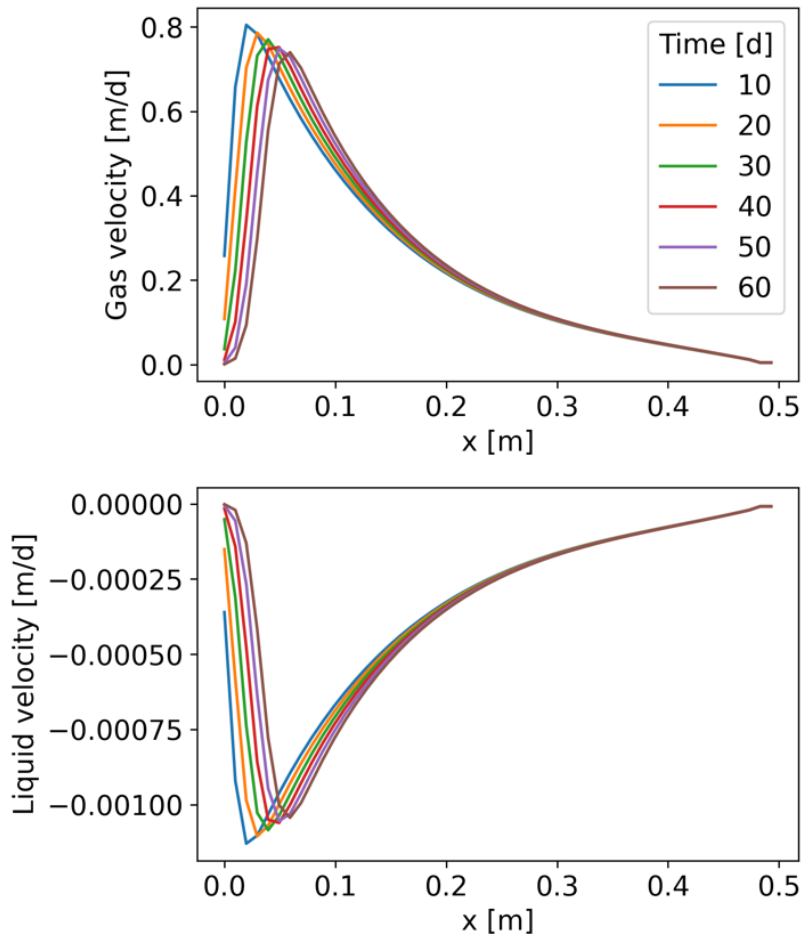


**Figure 2.2-32** Liquid and gas flow opposite to each other. Gas flows in the positive x direction (hot to cold), and liquid flows in the negative x direction (cold to hot).

## 2.3 Performance Improvements

### 2.3.1 Applications of New NTRDC Solver

Simulating coupled thermal-hydrologic-chemical processes in subsurface engineered radioactive waste repository systems can often involve solving discrete systems with extreme variation in grid length scales (high resolution in the nearfield of a repository, low resolution in the far field host rock environment), heterogeneity in physical properties (rock properties vs engineered barrier properties vs open tunnel properties), and phase transitions. Coupling all these processes together can be extremely computationally burdensome due to poor matrix conditioning as well as extreme transient nonlinearities that can be introduced.

PFLOTRAN's default nonlinear solver uses a traditional Jacobian-based Newton-Raphson method to solve nonlinear systems of partial differential equations. This method has been shown to be very effective for a broad range of subsurface flow and transport modeling applications, but requirements for modeling systems at higher resolution and with more nonlinear coupled processes have led the PFLOTRAN development team to develop more efficient solvers for multiphase and high temperature applications.

PFLOTRAN and PETSc, the solver library upon which PFLOTRAN is built, were recently updated to have the option of using a new trust region-based nonlinear solver, called the Newton Trust Region Dogleg Cauchy solver (NTRDC). Development of this solver and promising preliminary performance achievements were detailed in Nole et al. (2021). The NTRDC solver code was merged on January 20<sup>th</sup>, 2022 and was officially released in PETSc version 3.17.0 on March 30<sup>th</sup>, 2022. The code needed to link NTRDC with PFLOTRAN was merged to the master branch of PFLOTRAN on May 26<sup>th</sup>, 2022, and the next major release version of PFLOTRAN will include the NTRDC solver capability.

Here, we show a more thorough exploration of NTRDC performance on a repository-scale performance assessment model in unsaturated alluvium considering heat sources from 12 PWR, 24 PWR, and 37 PWR waste packages. Using PFLOTRAN's GENERAL mode, each waste package type is respectively associated with increasing thermal loading, which adds progressively stronger nonlinearity to the overall system through an increased prevalence of phase changes. It should be noted here that this particular simulation failed to complete using the default Newton Raphson nonlinear solver for all waste package types.

#### 2.3.1.1 *Computational Performance Analysis of UZ Simulations*

This simulation domain was introduced in Nole et al. (2021) but it is introduced again here as the solver behavior was studied in-depth. Here, the UZ alluvium reference case assumes a hypothetical mined repository in unsaturated alluvium located approximately 255 m below the land surface and containing 70,000 metric tons heavy metal of commercial spent nuclear fuel (Sevougian et al., 2019). It also assumes a small amount of precipitation, and a variably saturated model domain to a depth of around 500 m with water saturated media below. The initial condition of the simulation domain starts with an unsaturated two-phase condition above 500 m and a fully saturated liquid state below 500 m. The heat from the spent nuclear fuel waste packages can generate peak temperatures ranging from 150 °C to 350 °C to potentially boil off water to vapor even at elevated pressures. Figure 2.3-1 and Figure 2.3-2 illustrate the concept of the full-scale repository.



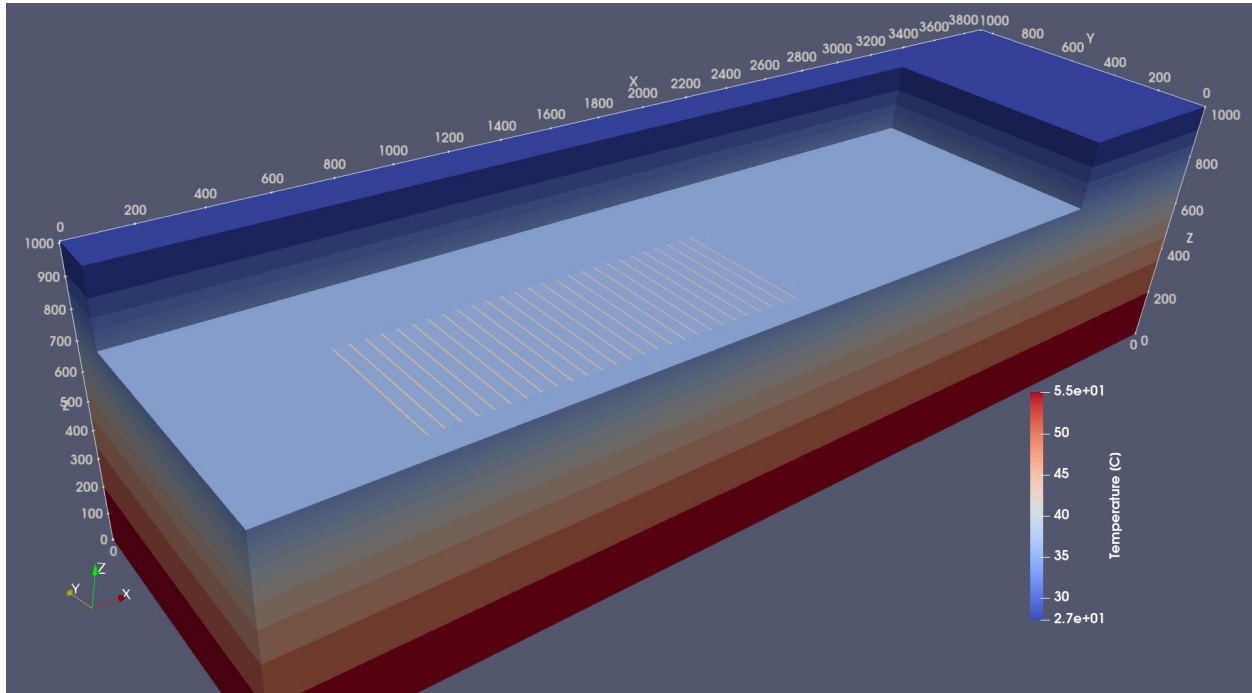
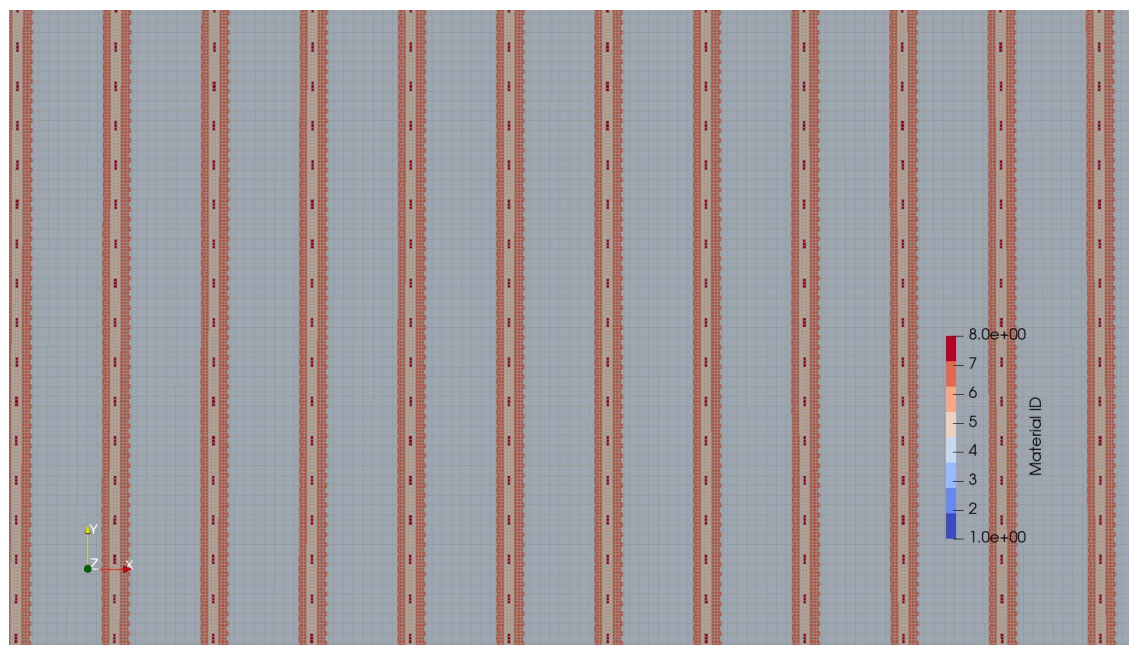


Figure 2.3-1 Cropped view of the symmetrical half of the unsaturated zone nuclear waste repository simulation domain where higher temperatures are seen in the waste disposal drifts (pink lines)

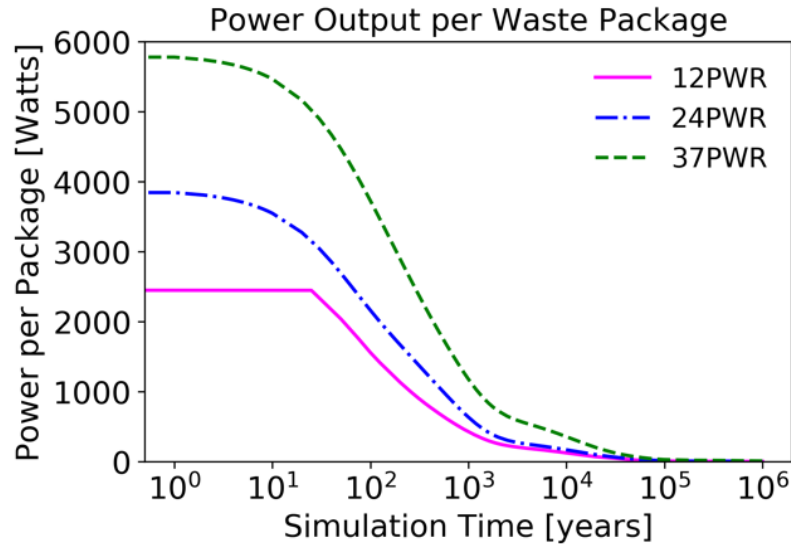




**Figure 2.3-2** Top view of the field-scale generic waste repository zoomed into the waste area. In lighter orange are the excavated drifts backfilled with engineered barrier after the closure. In darker orange is the damaged rock zone around the excavation. The heat source grid cells are the 5 m long waste packages in dark red. The light blue is the host rock, and the full-scale domain is shown in Figure 2.3-4.

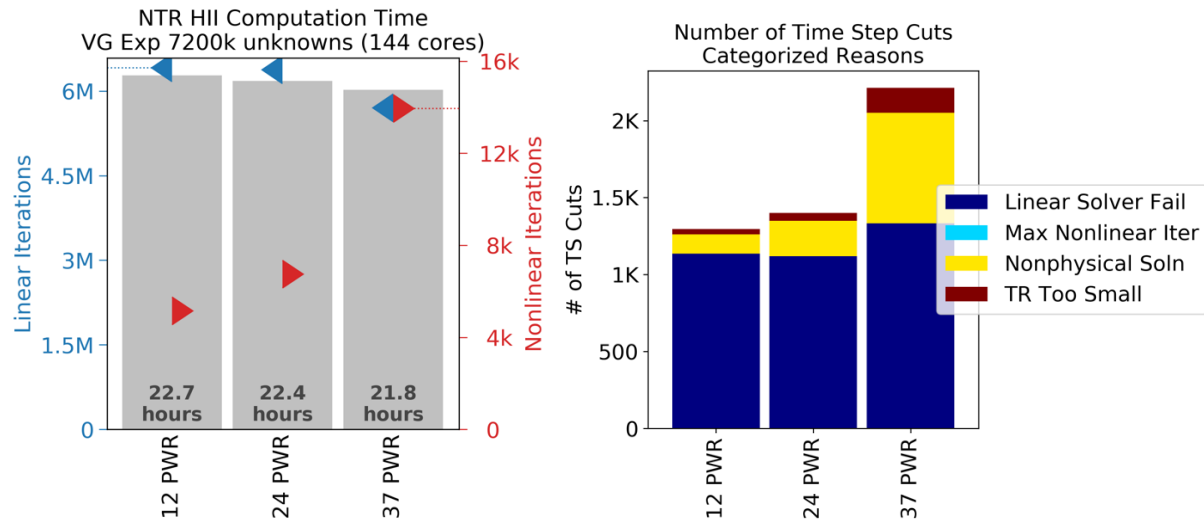
### *Numerical method behavior on different heat sources*

Figure 2.3-3 shows the power output per waste package depending on the number of assemblies that are in each waste package. The 37-PWR waste package outputs the most power (heat) over time and the 12-PWR waste package outputs the least. All types of packages generate the most heat at the time of emplacement and the power produced decays over time. They virtually have no decay heat after 100,000 years.



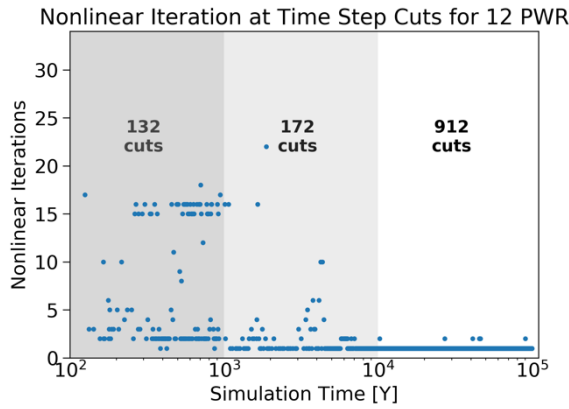
**Figure 2.3-3 Different power source profile by different waste package. Each waste package contains the indicated number of pressurized water reactor (PWR) fuel assemblies. They are characterized by simple time-varying heat source term in the simulation.**

Figure 2.3-4 demonstrates Newton Trust Region (NTR) for the three power levels. NTR is a variant of NTRDC where it does not apply the Cauchy solution but applies Trust Region only. The 12, 24, and 37 PWR cases all performed around the same in terms of computation time. However, there were some differences in linear iterations, nonlinear iterations, and time step cuts. The 12, 24, and 37 PWR cases experienced 2.7M, 4.3M, and 9.4M phase state changes (liquid to two-phase, two-phase to gas, vice versa) in the domain throughout the simulation, respectively. The 37 PWR produced three times as many state changes, increasing the number of Newton iterations and restricting time step size (i.e., through more time step cuts). The 12 PWR and 24 PWR cases had substantially fewer nonlinear iterations and time step cuts, yet the computation time was slightly greater than the 37 PWR case. The slightly lower number of linear solver iterations for 37 PWR may be explained by the larger number of time steps and conversely, the smaller average time step size, which produced linear systems that were more diagonally dominant and easier to solve. The NTR solver was able to resolve the extreme nonlinearities of the 37 PWR case and was able to complete the simulation with a run time similar to the 12 PWR case. Also, the early detection of non-convergence behavior (within a time step), indicated by the trust-region becoming too small, may have reduced the number of linear iterations for the 37 PWR case, thus reducing the overall computation time.

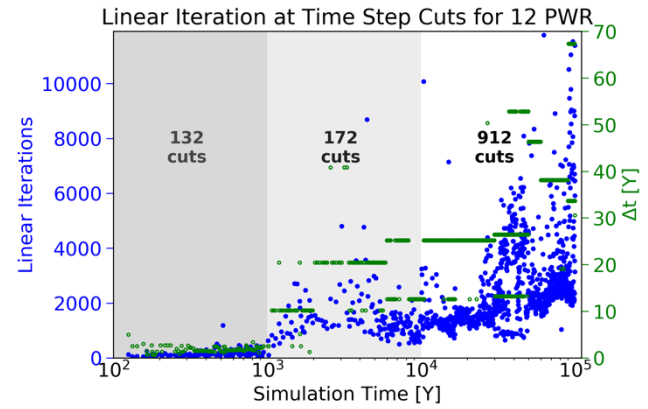


**Figure 2.3-4** Wall clock time, Newton and linear solver iteration counts, and time step cut counts for the fully refined model run with the three (12, 24, 37) power levels on 144 cores using NTR-HII

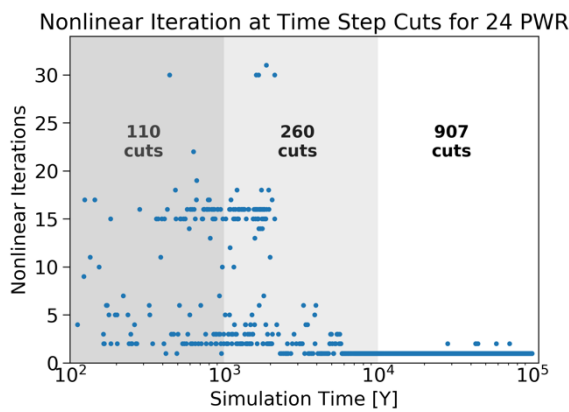
Figure 2.3-5 shows the time history of when the time step cuts occurred in the simulation and the number of nonlinear and linear iterations required to resolve the non-convergence to complete the time step. The 12 PWR case simulation had higher nonlinear iteration counts in between 200 years and 1000 years and small time step sizes which required fewer linear iterations to complete time steps. During this period, the heat generating waste packages cooled down from peak temperatures (see Figure 2.3-3), and hence, the system experienced aggressive re-saturation of the waste repository area. Many cells in all parts of the domain changed state due to re-saturation (e.g., gas  $\leftrightarrow$  two-phase  $\leftrightarrow$  liquid state). The 37 PWR cases had more nonlinear iterations after 1000 years, as those waste packages cooled down later in the simulation. The 37 PWR case had about 500 more time step cuts between 1000 and 10,000 years compared to the other two cases. Figure 2.3-5 clearly illustrates that the time step size remained small for the 37 PWR case during this period. Although the nonlinear iteration counts were higher, each iteration was fast due to the diagonally dominant linear system being solved (evidenced by the lower linear iteration counts between 1,000-10,000 years in Figure 2.3-5). Results for all three cases are similar after 10,000 years into the simulation. The 37 PWR case rarely exceeded 5000 linear iterations when there were time step cuts. The other two cases had larger time step sizes overall but solving these larger time steps often required more than 5000 linear iterations when the time step was cut. Essentially, all three cases went through the same process of dry-out and re-saturation, but at different times in the simulations. It is possible that the computation time for the other two cases could be reduced by specifying a maximum time step size of, e.g., 40 years, and such tuning will be studied in future work. These results demonstrate the robustness of the trust-region methods and their ability to improve nonlinear solver convergence.



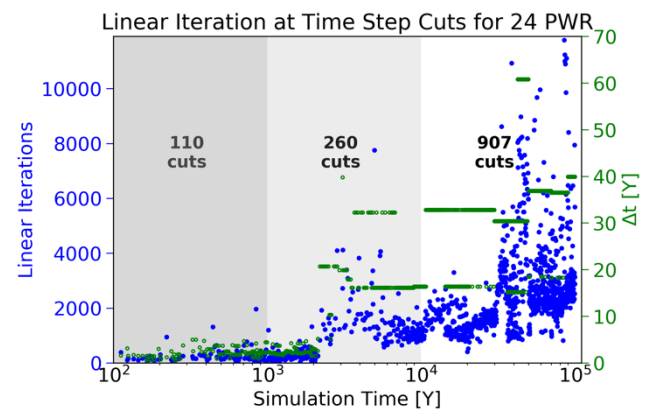
(a)



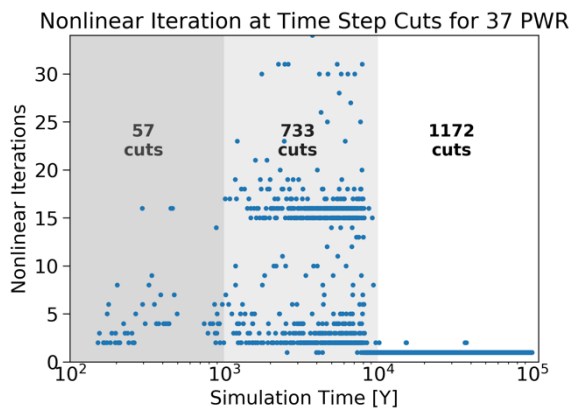
(b)



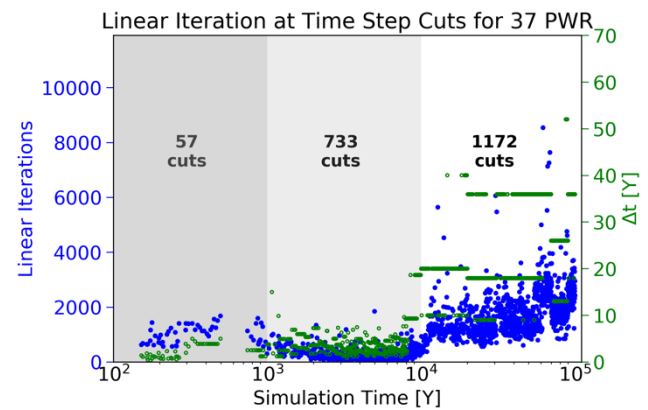
(c)



(d)



(e)



(f)

**Figure 2.3-5 Time history of nonlinear iterations after time step cuts, linear iterations and time step size for the fully refined model run with NTR. The left figures show the time history of time step cuts and the number of nonlinear iterations needed to complete the time step. The right figures show the number of linear iterations and the time step size.**

### 2.3.1.2 Grid Convergence and Weak Scaling Study

This grid convergence and weak scaling study was done to understand any improvements to be made in a large-scale nuclear waste repository simulation especially with waste packages with high decay heat. The weak scaling and grid convergence study is most properly done on structured grids. The biggest issue to do such studies with the unstructured grids is that the power source density can change depending on different discretization which completely altered the physics involved because of the different discretization. Here we introduce a much smaller domain with a 4x4 array of 37-PWR hot commercial spent nuclear fuel as power sources. Like the full alluvial unsaturated zone simulation domain (Mariner et al., 2020), the model assumes a mined repository in unsaturated alluvium located approximately 255 m below the land surface containing the waste packages.

The conceptual model considers 1 mm/year infiltration at the land surface and a water table at 500 m depth. Heat from the spent nuclear fuel waste packages can generate peak temperatures ranging from 150 °C to 350 °C that boil water and produce steam, even at elevated pressures. Figure 2.3-6 illustrates the different discretizations, and Figure 2.3-7 shows the initial conditions in temperature, liquid saturation, and liquid pressure.

The simulation domains have different levels of refinement: Refinement Level-0 has 41K grid cells, Level-1 has 285K grid cells, and Level-2 has 2.11M grid cells. For each level of refinement, the number of grid cells in each direction was multiplied by two. Therefore, each level should have approximately 8 times more grid cells than the previous level. In this study, the discretization of the waste package grid cells is not changed among different refinement levels to avoid a change in power density in the power sources and to avoid interactions between waste cells for thermal conduction and flow; hence, the refinement levels do not increase the number of grid cells by exactly 8 times.

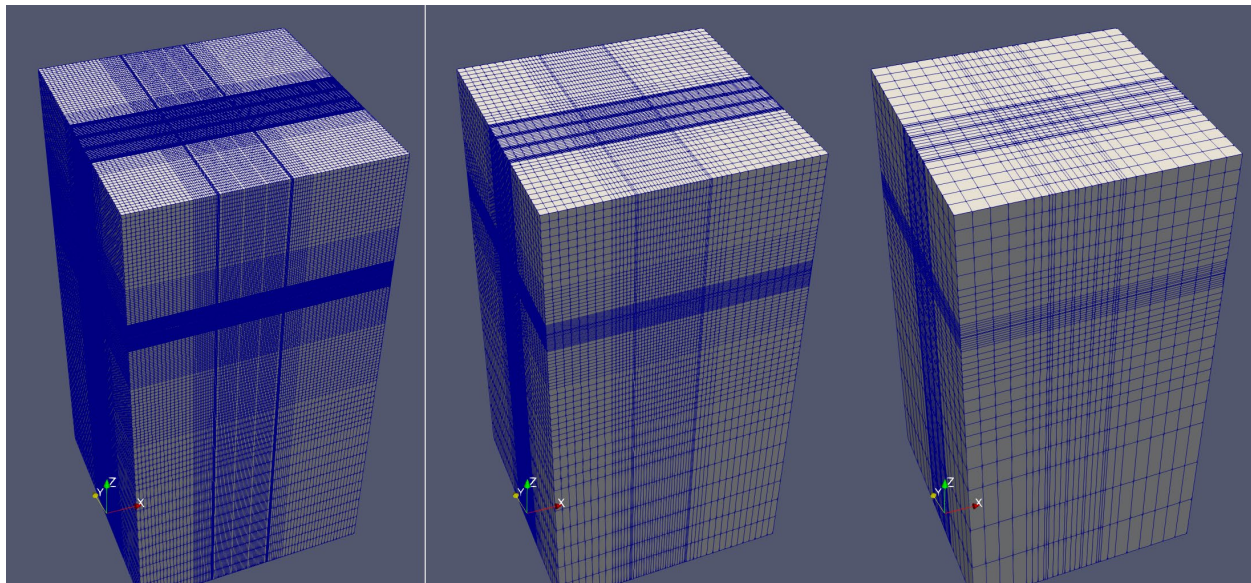


**Figure 2.3-6 Different discretization: refinement Level-2 (2.11M grid cells, left), Level-1 (285K grid cells, middle), and Level-0 (41K grid cells, right).**



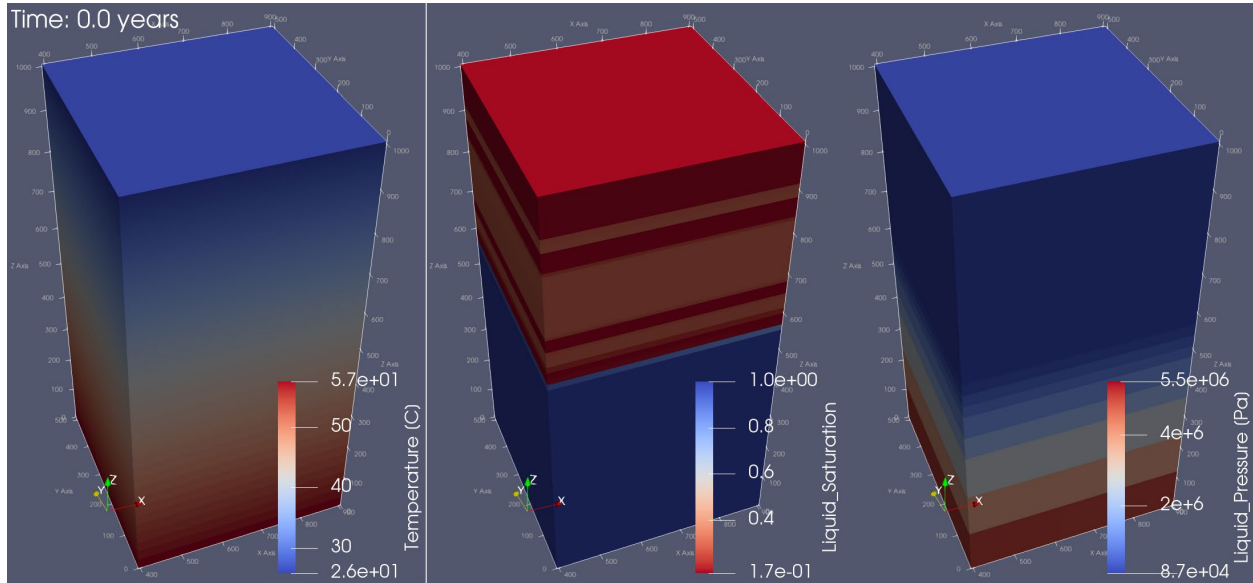


Figure 2.3-7 Initial condition of the simulation in temperature (left), liquid saturation (middle), and liquid pressure (right).

We ran the simulation for 10,000 years using 512 cores for refinement Level-2, 64 cores for Level-1, and 8 for Level-0 on Sandia National Laboratories' (SNL's) Boca HPC cluster that hosts compute nodes composed of 36 cores with Intel Xeon Gold 6240 Processor 2.60 GHz, 24.75 MB cache in two sockets with 6 memory channels.

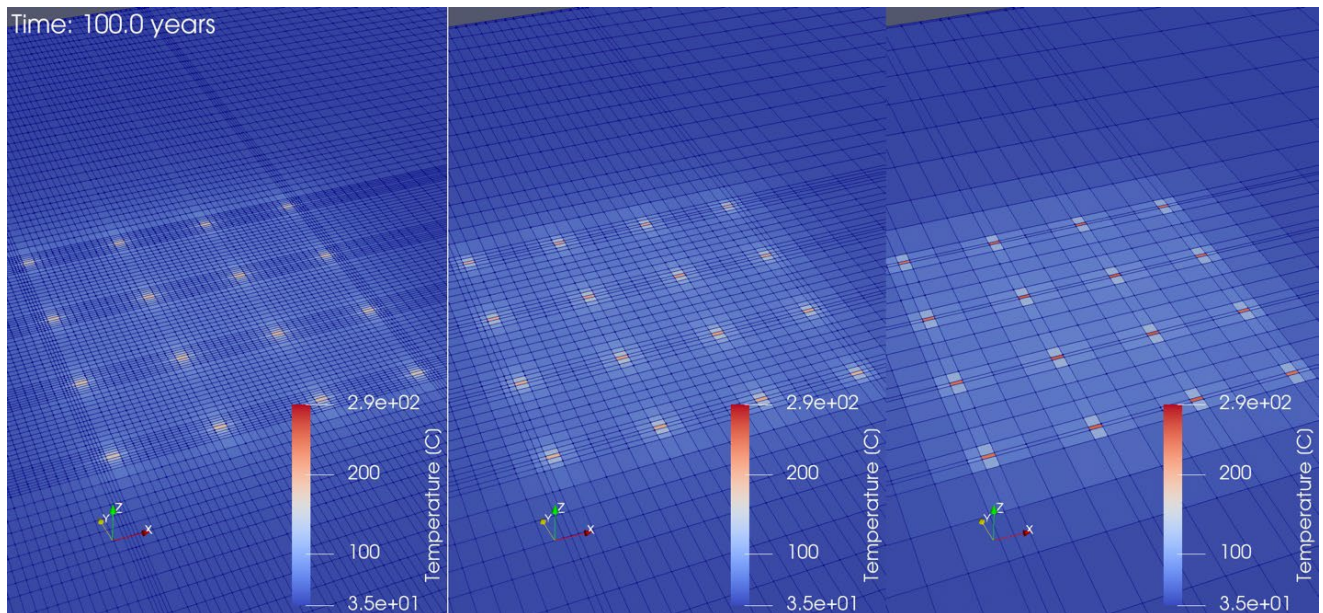
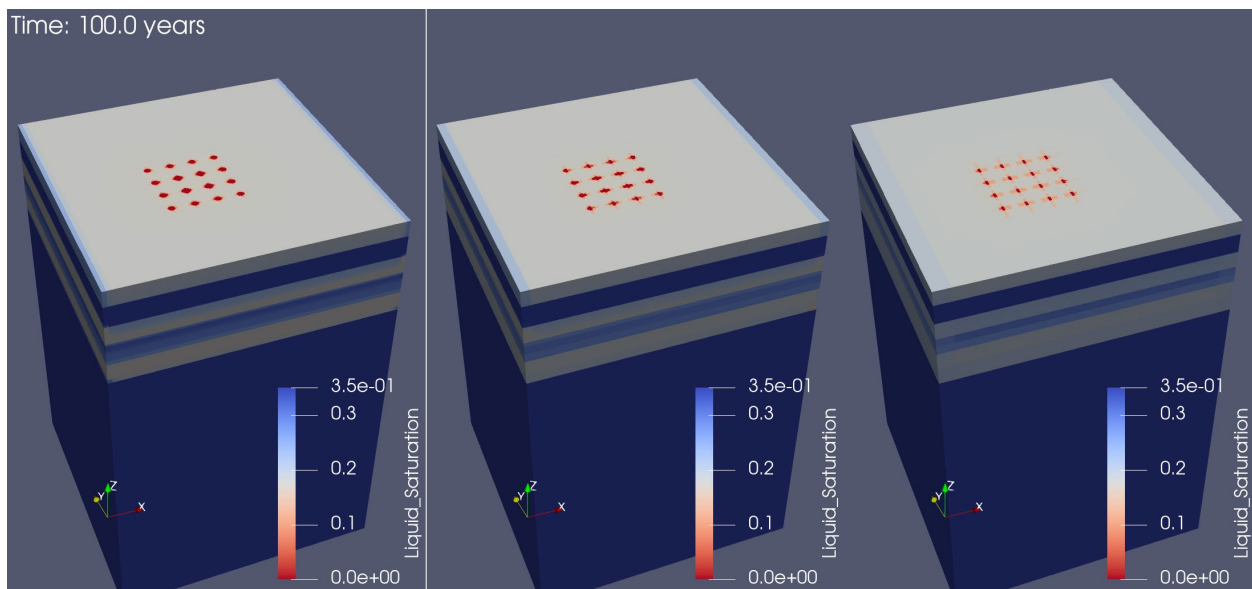


Figure 2.3-8 Temperature distribution at the waste package depth of 255 m below the surface at 100 years after the simulation began at level-2 refinement, level-1, and level-0 from left to right

Although we did not alter waste package discretization, we still observe differences between Level-0 and Level-1 in the peak temperature. However, the difference is much smaller between Level-2 and

Level-1. The peak temperatures at year 10 are 190.6 °C for Level-2, 201.8 °C for Level-1, and 287.7 °C for Level-0. At year 100, the peak temperatures were 183.0 °C for Level-2, 203.0 °C for Level-1, 252.7 °C for Level-0. The same pattern is shown at year 100. The physics of the simulation is slowly converging as we discretize to finer resolution, and the phenomena we observe are described in the liquid saturation plots. Figure 2.3-9 shows the liquid saturation distribution around the waste packages, and the red regions in the liquid saturation plot indicate dry-out caused by boiling near the waste packages. As water boils to vapor, energy is consumed causing lower peak temperatures in the Level-2 and level-1 domains. In the Level-0 domain, the peak temperatures are higher because less water boils surrounding the waste packages. Also note that the buffer material around the waste packages has a thermal conductivity that is more than an order of magnitude lower than the waste packages. Thus, the buffer ends up insulating the waste packages resulting in higher temperatures as energy is released from the waste packages.



**Figure 2.3-9 Liquid saturation for different discretization at 100-year simulation time**

The grid convergence test demonstrates that a certain level of refinement around wasted packages, which are most transient in the simulation domain, is necessary to capture the correct physics as we saw the peak temperatures converge towards a certain value with increasing refinement in the domain.

***Weak Scaling Test***

As shown in Figure 2.3-8 and Figure 2.3-9, the models' response to the underlying physics are very sensitive to the level of discretization in the simulation domain. Therefore, we do not expect consistent computing performance for all the tests. Table 2.3-1 shows the parameters for the weak scaling test. The number of grid cells per core are 4131 for Level-2, 4447 for Level-1, and 5118 for Level-0. The results are shown in Table 2.3-2 and are reported at year 100 of the simulation time and year 10,000. The computation time is very different for a 10,000-year simulation ranging from 1.6 minutes to 408 minutes, and even the shorter simulation of 100 years ranged from 41 seconds to 268 seconds. The differences in the number of nonlinear iterations emphasizes the fact that the simulations are encountering different physics, with Level-2 being the most difficult.

**Table 2.3-1 Weak scaling test parameters**

Discretization	Grid cells	Number of cores	Grid cells per core
Level-2	2115071	512	4131
Level-1	284591	64	4447.7
Level-0	40949	8	5118.6

**Table 2.3-2 Weak scaling test results**

Discretization	Run time at 100y	Run Time at 10,000y	Nonlinear Iterations at 10,000y
Level-2	268 sec	22.8 min	2565
Level-1	96 sec	408 min	95520
Level-0	41 sec	1.6 min	394



### 2.3.2 Characteristic Curves from Datasets

In the generalized Darcy model, capillary pressure and relative permeability functions, collectively known as soil-water characteristic curves, are typically non-linear functions of saturation that represent the interactions between wetting and nonwetting phases in porous media with respect to fluid flow and pressure propagation. Because both functions are non-linear functions of water saturation, this causes solution of the two-phase flow equations in porous media to be a distinctly non-linear problem.

While non-linear, the exact capillary pressure relationship for a porous material is scarcely known. Capillary pressure versus saturation can be measured using imbibition and drainage experiments (e.g., mercury injection capillary pressure, or MICP experiments). Empirical models, such as van Genuchten and Brooks-Corey, have been created that approximate the capillary pressure with saturation using only a handful of parameters. In turn, Burdine and Mualem models can be utilized to estimate the relative permeability from these capillary pressure and saturation relations, and these analytical formulations can be derived in manners that are consistent with a given capillary pressure function. However, existing capillary pressure or relative permeability models may not adequately represent experimental data, especially in geologic media with multimodal pore size distributions. Furthermore, having the ability to read in characteristic curves directly from datasets not only facilitates desirable flexibility but it also can potentially provide performance gains if such a method eliminates the need for frequently evaluating a complicated analytical function. This is especially pertinent to characteristic curve computations since these are some of the most often-repeated state variable computations in the code.

#### 2.3.2.1 *Linear Interpolation*

The capability to read in capillary pressure, liquid relative permeability, and gas relative permeability as functions of liquid saturation and time has been added into PFLOTRAN. When reading characteristic curve information from datasets, evaluation of capillary pressure and relative permeability at an arbitrary saturation is achieved through linear interpolation between capillary pressure values at known saturations. Capillary pressure also can evolve with time, but dataset values are updated in a stepwise fashion and held constant between time levels of the dataset.

When using a particular capillary pressure dataset, the single most important benefit of this approach is clearly that the capillary pressure function can more adequately be approximated over the range of relevant liquid saturations (Figure 2.3-10). In this example from a dataset included in Heath et al. (2021), a Van Genuchten capillary pressure function fit to the data does a good job near the liquid saturation extremes but can fall close to an order of magnitude short at intermediate saturations. This isn't to say that no analytical function could match the curve, but issues like this are typical when attempting to approximate data by a set of standard functional forms like those implemented in PFLOTRAN.

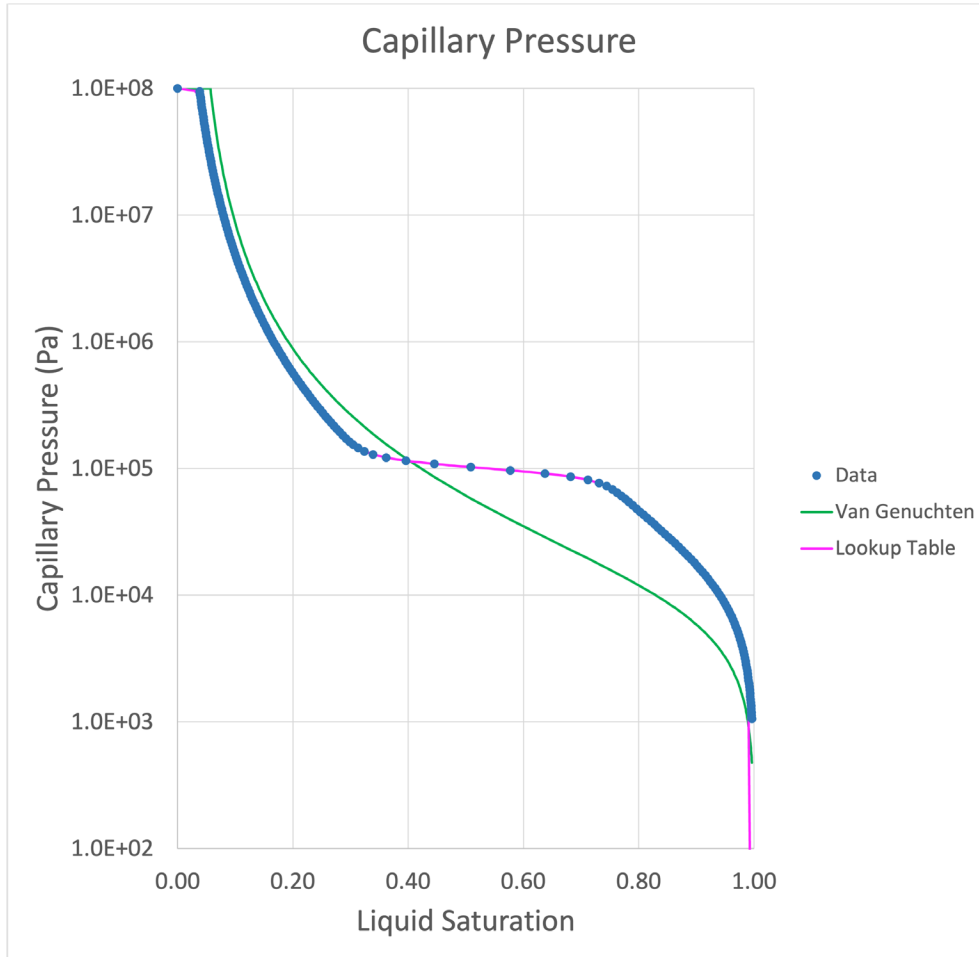


**Figure 2.3-10** Capillary pressure data from Heath et al. (2021) along with a Van Genuchten analytical curve fit and a lookup table (output using the TEST option) using linear interpolation between data points.

Similarly, lookup table interpolation does a better job of matching the relative permeability data from this dataset than a Van Genuchten-derived Mualem liquid relative permeability function (Figure 2.3-11). In this example, Van Genuchten parameters had to be re-fit (see Table 2.3-3) to do a better job matching the data; while not uncommon, this can lead to difficulties in correlating pore system characteristics with generalized flow behavior.

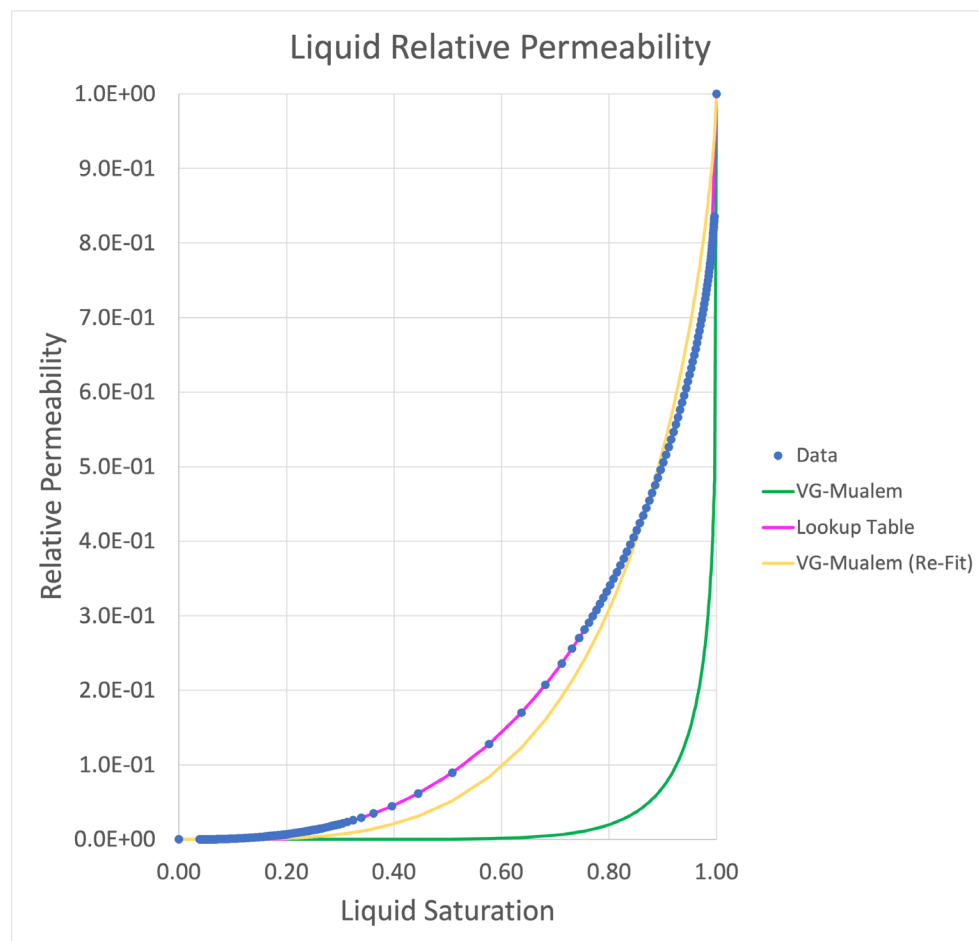


**Figure 2.3-11** Relative permeability data from Heath et al. (2021) along with a Van Genuchten-Mualem analytical curve fit with parameters from the capillary pressure fit, re-fit parameters, and a lookup table (output using the TEST option) using linear interpolation between data points.

**Table 2.3-3** Van Genuchten parameters for the a) capillary pressure function and b) re-fit for the relative permeability function

a)	Alpha [Pa <sup>-1</sup> ]	m	n	S <sub>ri</sub>	Max P <sub>C</sub> [Pa]
	1.00E-04	0.28	1.38888889	3.00E-02	100000000
b)	Alpha [Pa <sup>-1</sup> ]	m	n	S <sub>ri</sub>	Max P <sub>C</sub> [Pa]
	1.00E-04	0.7	3.33333333	3.00E-02	100000000

The biggest drawback of using linear interpolation to predict capillary pressure and relative permeability from datasets is that although the function may be continuous, it is not smooth (Figure 2.3-12). This can lead to discontinuous or non-smooth derivatives in these functions, which when used in numerical solution of a system of partial differential equations can make it very challenging to converge to an adequate solution. Minimizing this issue requires very high-resolution capillary pressure and relative permeability datasets, especially in regions of high curvature.

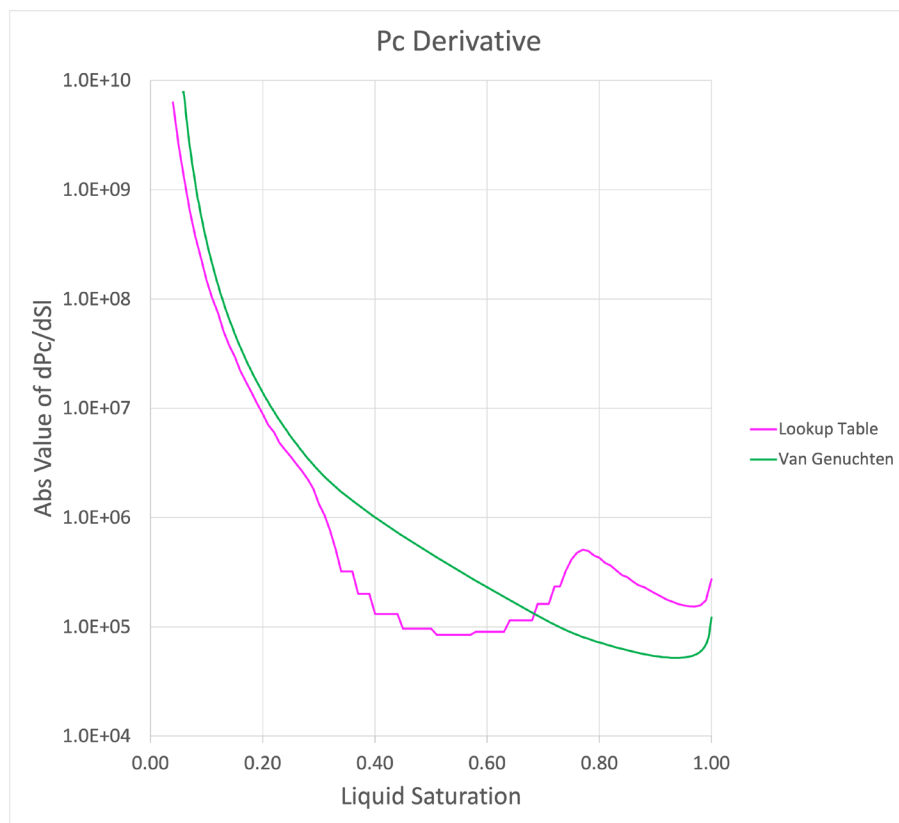


**Figure 2.3-12 Absolute value of the derivative of capillary pressure with respect to liquid saturation for the analytical Van Genuchten curve fit and the lookup table using linear interpolation between data points.**

### 2.3.2.2 Splines

Alternatively, cubic splines are a method that can provide C1 continuity using only arithmetic expressions. While there are numerous classes of splines, including the natural C2 splines and B-splines, for the purposes of modeling capillary pressure and relative permeability, monotonicity of the function is important to avoid introducing degenerate roots for the Newton-Raphson solver. For this reason, Fritsch (1982) proposed a piecewise cubic Hermite interpolation polynomial (PCHIP) for scientific computing. This method was improved upon by Fritsch and Butland (1984) and implemented as a library in the public domain SLATEC library. Using this method, the capability to model any monotonic set of capillary pressure or relative permeability data is currently being developed in PFLOTTRAN.

In terms of computational performance, this method has its advantages. Although closed-form, empirical models are rarely simple algebraic expressions a computer can calculate. While modern CPU's are more and more efficient at estimating fundamental but transcendental functions, such as  $exp()$  and  $log()$ , these operations remain more complex than arithmetic floating point operations. In some cases, an existing closed form but non-algebraic capillary pressure function may be accurately and more expediently calculating using a set of cubic splines.

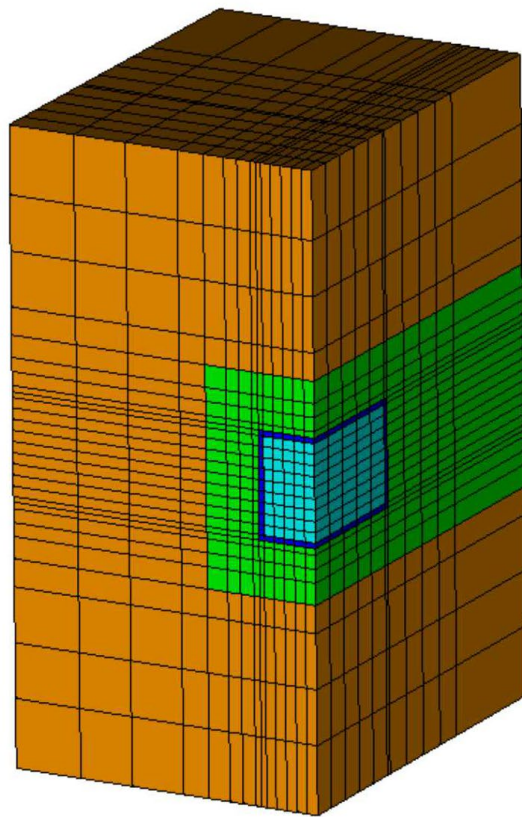
Finally, in addition to the advantages of directly utilizing experimental data and reducing the computation time during each non-linear function evaluation, use of cubic splines also enables

optimization using vectorization or array programming. That is, modern Fortran can evaluate the capillary pressure or relative permeability for an array of saturations in parallel using the Single Instruction Multiple Data on modern CPU's and GPU's. While piecewise, cubic splines differ from conditional branching in that only the values of the polynomial coefficients vary, not the instructions. While modern CPU's with 256- or 512-bit Advanced Vector Extensions (AVX) can conduct 4 or 8 double precision operations simultaneously, GPU units can evaluate far wider arrays simultaneously. The ability to leverage these next-gen computational developments is currently an area of active inquiry for the PFLOTRAN development team.

## 2.4 Integration and Outreach

### 2.4.1 ORNL Collaboration

The PFLOTRAN developers have been collaborating with modelers at Oak Ridge National Laboratory to overcome numerical performance issues associated with a fine-scale single waste-package model of a potential criticality event in a disposed dual-purpose canister in an unsaturated alluvium host rock (Price et al., 2020). In this model (Figure 2.4-1), a regular grid is set up to contain waste package internals (heat source), a waste package shell (physical liquid migration barrier), backfill in a repository drift, and host rock. The system is initially unsaturated and sits above the water table, yet infiltration from the top acts as a source of water to the domain. Water migrates downward toward the water table but as it does so it encounters a decay heat source from the waste package with the addition of a heat of criticality. Given a known decay heat, the goal of this study is to determine the potential sustainable source of heat that can maintain liquid water in the waste package.



NOTE: This 3D perspective is cut through the drift centerline and waste package midpoint and thus shows only one-quarter of the waste package. Green = backfilled drift, brown = host rock formation, light blue = waste package internals, and dark blue = waste package shell.

**Figure 2.4-1 Cut-out of the computational domain described in Price et al., 2020**

This problem is extremely numerically challenging because it involves coupled interaction of several highly nonlinear phenomena. Capillary suction and gravity forces draw liquid water into the dry host rock, but when liquid water encounters the waste package heat source it will tend to evaporate. Gas phase pressure increases, moving humid air away from the heat source and causing water to recondense

elsewhere. All these processes happen at the dry limit of the host rock, meaning that much of the domain can be characterized as single-phase gas adjacent to two-phase liquid and gas. On top of that, material properties are intentionally designed with high contrast so that water will not infiltrate the waste package until the top portion of the waste package shell is “breached” and permeability is increased. The presence of this coupled combination of nonlinear phenomena meant a parameter study using these simulations was unachievable in Price et al. (2020); however, by updating the models to use extended characteristic curve functions that smooth out the dry end of the capillary pressure curves, we were able to finish a set of bounding simulations (see iteration counts and wall clock times in Table 2.4-1). These results are a promising step forward to completing a parameter sensitivity study on possible criticality limits in unsaturated zone geologic repositories.

**Table 2.4-1 Linear and nonlinear solver iterations and wall clock time for bounding power and infiltration rate simulations for a criticality consequence analysis study that previously was unachievable without characteristic curve extensions.**

<b>WF Criticality Power (W)</b>	<b>Infiltration Rate (mm/yr)</b>	<b>Linear Iterations</b>	<b>Nonlinear Iterations</b>	<b>Wall Clock Time (hr)</b>	<b>Time Step Cuts</b>
0	2	$1.2533 \times 10^7$	$1.6247 \times 10^5$	4.661	2739
0	5	$7.4062 \times 10^6$	$8.5101 \times 10^4$	6.702	4475
100	2	$1.2843 \times 10^7$	$1.6433 \times 10^5$	5.207	2816
100	5	$1.1228 \times 10^7$	$1.0174 \times 10^5$	12.96	4615

### 2.4.2 LBNL Collaboration

The PFLOTRAN development team continued to work with Lawrence Berkeley National Laboratory this year on reduced order process model design for implementation in PFLOTRAN. Several meetings occurred to push forward the reduced order geomechanics modeling that began in FY20 (Chang et al., 2021), including brainstorming a salt creep and drift backfill convergence model that could be implemented in a similar manner to PFLOTRAN's WIPP porosity surface reduced order model with additional feedback from the thermal state of the host rock. In addition, reduced order equilibrium sorption coefficient ( $k_d$ ) models are being pursued in order to overcome the computational challenges associated with high fidelity modeling of the chemistry of an engineered bentonite buffer barrier system in PA-scale simulations. These reduced order models would ideally be formulated as functions of known state variables in the system, such as in the temperature-dependent  $k_d$  model described in Section 2.2.1.4 of this report. In fact, the material transform module outlined in this report serves as the basis upon which the PFLOTRAN development team plans to implement new reduced order  $k_d$  models as part of this collaboration. The starting point will be to implement the capability to read in material and isotope-specific  $k_d$  values as functions of time from outputs of higher fidelity, smaller scale models produced by LBNL. With this as a baseline, we will investigate how to generalize the method to allow flexibility while maintaining numerical efficiency.



### 2.4.3 ANL Integration

The PFLOTRAN and PETSc development teams collaborated over the course of 4 months in FY22 to incorporate the Newton trust-region dogleg Cauchy (NTRDC) solver code that was developed by the Sandia PFLOTRAN development team. This capability was shown to be highly effective at overcoming challenges faced by a significant number of PFLOTRAN users, and so it was necessary for our team to ensure that this new solver became a part of an official PETSc release. The PETSc team also acknowledged that NTRDC is a capability that was anticipated by their users for other purposes as well.

#### 2.4.4 International User Base

Estimating the size and extent of the PFLOTRAN user community is relatively difficult due to the inability to track downloads on Bitbucket. However, through Google Analytics, the hits on the PFLOTRAN website are tracked which provides a qualitative estimate (Figure 2.4-2) and demonstrates that the PFLOTRAN user base is multi-national. The top ten countries with the most users are as follows (from most to fewest users): United States, China, Germany, United Kingdom, Canada, Spain, Japan, South Korea, Norway, and Taiwan.

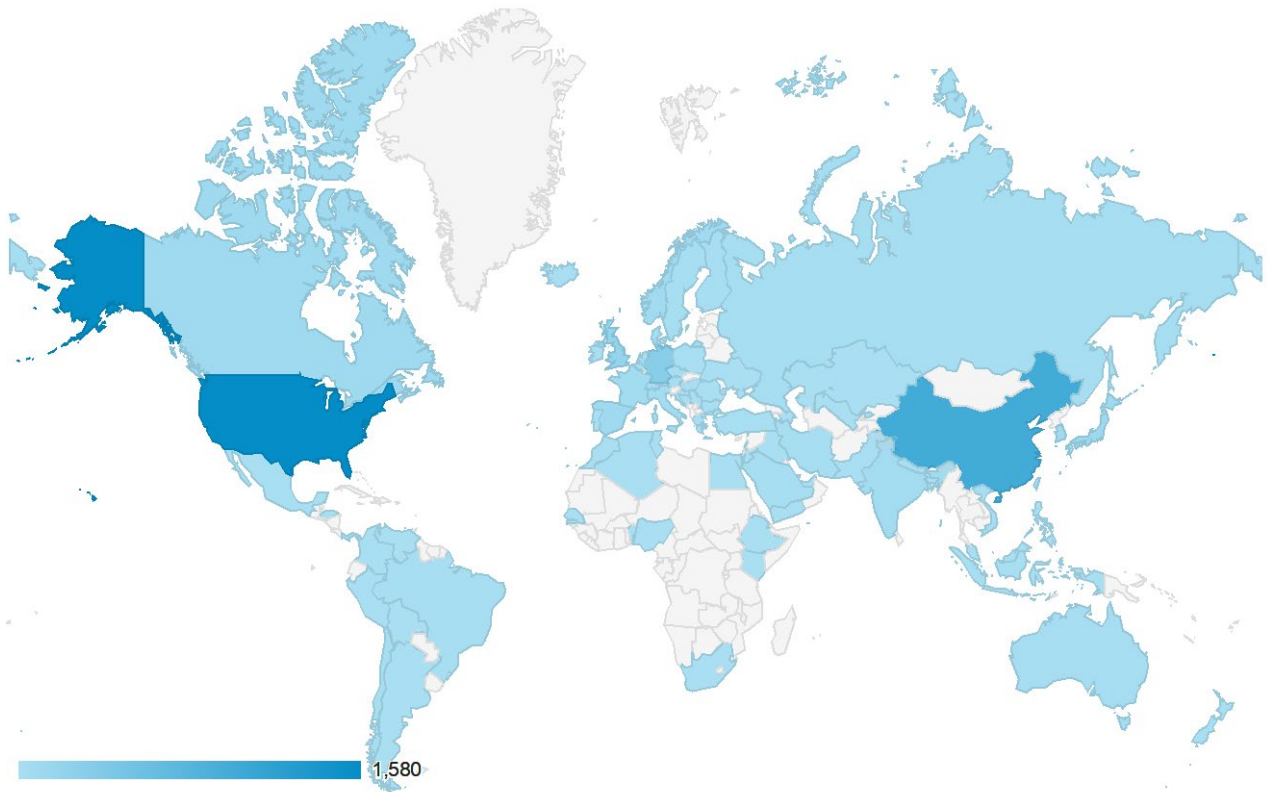


Figure 2.4-2 Total global hits from individual users to the PFLOTRAN website, from May 01, 2021 to April 30, 2022.

### 2.4.5 Short Course

This year, in coordination with the Nuclear Threat Initiative's Pacific Rim Spent Fuel Management Partnership Working Group, PFLOTRAN developers at Sandia and Pacific Northwest National Laboratories held a 5-week virtual PFLOTRAN short course from June 14<sup>th</sup> through July 12<sup>th</sup>. This beginner short course was developed based off feedback from the first virtual short course held in July 2021 with a focus on greater time in small "breakout" group, instructor-led sessions with a minimized instructor-to-student ratio. This year, 38 students registered from across the U.S. and around the world. Within the United States, attendees included researchers from Sandia National Laboratories, Oak Ridge National Laboratory, Lawrence Berkeley National Laboratory, the Environmental Protection Agency, and the University of Texas at El Paso. Internationally, students represented 6 countries: Japan, India, Australia, Taiwan, Canada, and South Korea. This year, the short course had 9 experienced PFLOTRAN users and developers serving as instructors who led the individual breakout rooms. The short course included an introduction to fluid flow and chemical transport modeling, multiphase flow and heat transport, radionuclide transport, visualization. Concepts were tied together with a final practice problem modeling a subsurface radioactive waste repository system.

### 2.4.6 Publications

The PFLOTRAN development team was involved in several journal publications in FY 2022, including:

Chang, K. W., Nole, M., & Stein, E. R. (2021). Reduced-order modeling of near-field THMC coupled processes for nuclear waste repositories in shale. *Computers and Geotechnics*, 138, 104326.

Park, Heeho Daniel. "Linear and nonlinear solvers for simulating high-temperature multiphase flow within large-scale engineered subsurface systems." PhD diss., University of Illinois at Urbana-Champaign, 2021.

Park, H. D., Hammond, G. E., Valocchi, A. J., & LaForce, T. (2021). Linear and nonlinear solvers for simulating multiphase flow within large-scale engineered subsurface systems. *Advances in Water Resources*, 156, 104029.

Park, Heeho D., Matthew Paul, Glenn E. Hammond, and Albert J. Valocchi. (2022, under review) "Newton trust-region methods with primary variable switching for simulating high temperature multiphase porous media flow" *Advances in Water Resources*.

Swinney, M. W., Bhatt, S., Davidson, G. G., Nole, M., & Banerjee, K. (2022). Multiphysics modeling of a critical dual-purpose canister in a saturated geological repository. *Annals of Nuclear Energy*, 175, 109204.

### 3. REFERENCES

- Aakesson, M., Kristensson, O., Boergesson, L., Dueck, A., & Hernelind, J. (2010). *THM modelling of buffer, backfill and other system components. Critical processes and scenarios*(No. SKB-TR--10-11). Swedish Nuclear Fuel and Waste Management Co. 2010.
- Alt-Epping, P., Diamond, L. W., Wanner, C., & Hammond, G. E. (2021). Effect of glacial/interglacial recharge conditions on flow of meteoric water through deep orogenic faults: insights into the geothermal system at Grimsel Pass, Switzerland. *Journal of Geophysical Research: Solid Earth*, 126(7), e2020JB021271.
- Cuadros, J., & Linares, J. (1996). Experimental kinetic study of the smectite-to-illite transformation. *Geochimica et Cosmochimica Acta*, 60(3), 439-453.
- Balay, S., S. Abhyankar, M.F. Adams, S. Benson, J. Brown, P. Brune, K. Buschelman, E. Constantinescu, L. Dalcin, A. Dener, V. Eijkhout, W.D. Gropp, V. Hapla, T. Isaac, P. Jolivet, D. Karpeev, D. Kaushik, M.G. Knepley, F. Kong, S. Kruger, D.A. May, L. Curfman McInnes, R.T. Mills, L. Mitchell, T. Munson, J.E. Roman, K. Rupp, P. Sanan, J. Sarich, B.F. Smith, S. Zampini, H. Zhang, H. Zhang and J. Zhang. 2022. *PETSc/TAO Users Manual*. Argonne National Laboratory, ANL-21/39 – Revision 3.17.
- Balay, S., J. Brown, K. Buschelman, V. Eijkhout, W. D. Gropp, D. Kaushik, M. G. Knepley, L. Curfman McInnes, B. F. Smith and H. Zhang (2013). *PETSc Users Manual*. Argonne, Illinois, Argonne National Laboratory.
- Batzle, M., & Wang, Z. (1992). Seismic properties of pore fluids. *Geophysics*, 57(11), 1396–1408. <https://doi.org/10.1190/1.1443207>.
- Beskardes, G.D., Weiss, C.J., Kuhlman, K.L. and Chang, K.W., (2022). Finite Element Modeling of Diffusion in Fractured Porous Media by Using Hierarchical Material Properties. *Water Resources Research*, 58(2), p. e2020WR029510.
- Blacker, T., Bohnhoff, W., & Edwards, T., (1994), CUBIT mesh generation environment. Volume 1: User's manual, May 1994.
- Chang, K. W., Nole, M., & Stein, E. R. (2021). Reduced-order modeling of near-field THMC coupled processes for nuclear waste repositories in shale. *Computers and Geotechnics*, 138, 104326.
- Chen, X., G. Hammond, C. Murray, M. Rockhold, V. Vermeul and J. Zachara (2013). "Applications of ensemble-based data assimilation techniques for aquifer characterization using tracer data at Hanford 300 area." *Water Resources Research* 49: 7064-7076.
- Chen, Z., Huan, G. and Ma, Y. (2006) *Computational Methods for Multiphase Flows in Porous media*, SIAM, pp. 531.
- DOE (2012). *Used Fuel Disposition Campaign Disposal Research and Development Roadmap*. Washington, D.C., U.S. DOE Office of Nuclear Energy, Used Fuel Disposition.
- Elder, J. W. (1967). Steady free convection in a porous medium heated from below. *Journal of Fluid Mechanics*, 27(1), 29-48.
- Fritsch, F. N. (1982). *Piecewise Cubic Hermite Interpolation Package. Final specifications* (No. UCID-30194). Lawrence Livermore National Lab., CA (USA).
- Fritsch, F. N., & Butland, J. (1984). A method for constructing local monotone piecewise cubic interpolants. *SIAM journal on scientific and statistical computing*, 5(2), 300-304.
- Haas, J. L. (1971). The effect of salinity on the maximum thermal gradient of a hydrothermal system at hydrostatic pressure. *Economic Geology*, 66(6), 940–946.
- Haas, J. L. (1976). Physical properties of the coexisting phases and thermochemical properties of the H<sub>2</sub>O component in boiling NaCl solutions. *US Geol. Surv. Bull.*, 1421, 1–73.
- Hammond, G., P. Lichtner and C. Lu (2007). "Subsurface multiphase flow and multicomponent reactive transport modeling using high performance computing." *Journal of Physics: Conference Series* 78: 1-10.

- Hammond, G. E., P. C. Lichtner, C. Lu and R. T. Mills (2011). PFLOTRAN: Reactive Flow and Transport Code for Use on Laptops to Leadership-Class Supercomputers. Groundwater Reactive Transport Models. F. Zhang, G. T. Yeh and J. Parker, Bentham Science Publishers.
- Heath, J. E., Kuhlman, K. L., Broome, S. T., Wilson, J. E., & Malama, B. (2021). Heterogeneous multiphase flow properties of volcanic rocks and implications for noble gas transport from underground nuclear explosions. *Vadose Zone Journal*, 20(3), e20123.
- Huang, W. L., Longo, J. M., & Pevear, D. R. (1993). An experimentally derived kinetic model for smectite-to-illite conversion and its use as a geothermometer. *Clays and Clay Minerals*, 41(2), 162-177.
- Johnson, P. J., Stauffer, P. H., Zyvoloski, G. A., & Bourret, S. M. (2018). *Experiments and modeling to support field test design*. Los Alamos National Lab.(LANL), Los Alamos, NM (United States).
- Karnland, O., & Birgersson, M. (2006). Montmorillonite stability. With special respect to KBS-3 conditions.
- Lichtner, P.C. (1985) Continuum Model for Simultaneous Chemical Reactions and Mass Transport in Hydrothermal Systems, *Geochimica et Cosmochimica Acta*, 49, 779–800.
- Lichtner, P.C. (2016) Kinetic Rate Laws Invariant to Scaling the Mineral Formula Unit, *American Journal of Science*, 316, 437–469.
- Lichtner, P. C. and G. E. Hammond (2012). Quick Reference Guide: PFLOTRAN 2.0 (LA-CC-09-047) Multiphase-Multicomponent-Multiscale Massively Parallel Reactive Transport Code. Los Alamos, New Mexico, Los Alamos National Laboratory.
- Lichtner, P.C. and Karra, S. (2014) Chapter 3. Modeling multiscale-multiphase-multicomponent reactive flows in porous media: Application to CO<sub>2</sub> sequestration and enhanced geothermal energy using PFLOTRAN, *Computational Models for CO<sub>2</sub> Geo-sequestration & Compressed Air Energy Storage*, Edited by Rafid Al-Khoury and Jochen Bundschuh, CRC Press 2014, Pages 81–136, Print ISBN: 978-1-138-01520-3, eBook ISBN: 978-1-315-77872-3.
- Lu, C. and P. C. Lichtner (2007). "High resolution numerical investigation on the effect of convective instability on long term CO<sub>2</sub> storage in saline aquifers." *Journal of Physics Conference Series* 78: U320-U325.
- Mariner, P., Berg, T., Debusschere, B., Eckert, A., Harvey, J., LaForce, T., ... & Chang, K. W. (2021). *GDSA Framework Development and Process Model Integration FY2021* (No. SAND2021-12626R). Sandia National Lab.(SNL-NM), Albuquerque, NM (United States).
- Mills, R., C. Lu, P. C. Lichtner and G. Hammond (2007). Simulating subsurface flow and transport on ultrascale computers using PFLOTRAN. 3rd Annual Scientific Discovery through Advanced Computing Conference (SciDAC 2007), Boston, *Journal of Physics Conference Series*.
- Moreno, L., Liu, L., & Neretnieks, I. (2011). Erosion of sodium bentonite by flow and colloid diffusion. *Physics and Chemistry of the Earth, Parts A/B/C*, 36(17-18), 1600-1606.
- Navarre-Sitchler, A., R. M. Maxwell, E. R. Siirila, G. E. Hammond and P. C. Lichtner (2013). "Elucidating geochemical response of shallow heterogeneous aquifers to CO<sub>2</sub> leakage using high-performance computing: implications for monitoring CO<sub>2</sub> sequestration." *Advances in Water Resources* 53: 44-55.
- Neretnieks, I., L. Moreno, and L. Liu (2017). Clay erosion – impact of flocculation and gravitation. Technical report TR-16-11. Svensk Kärnbränslehantering AB, Swedish Nuclear Fuel and Waste Management Co, Stockholm, Sweden.
- Nole, M., Leone, R., Park, H., Paul, M., Salazar, A., Hammond, G., & Lichtner, P. (2021). *PFLOTRAN Development FY2021* (No. SAND2021-8709R). Sandia National Lab. (SNL-NM), Albuquerque, NM (United States).
- Olivella, S., Carrera, J., Gens, A., & Alonso, E. (1994). Nonisothermal multiphase flow of brine and gas through saline media. *Transport in Porous Media*, 15(3), 271–293.
- Olivella, S., Castagna, S., Alonso, E., & Lloret, A. (2011). Porosity variations in saline media induced by temperature gradients: Experimental evidences and modelling. *Transport in Porous Media*, 90(3), 763–777.

- Park, H. D., Hammond, G. E., Valocchi, A. J., & LaForce, T. (2021). Linear and nonlinear solvers for simulating multiphase flow within large-scale engineered subsurface systems. *Advances in Water Resources*, 156, 104029.
- Park, H.D., M. Paul, G.E. Hammond and A.J. Valocchi. 2022. Newton trust-region methods with primary variable switching for simulating high temperature multiphase porous media flow. *Advances in Water Resources*, under review.
- Posiva (2013). Safety Case for the Disposal of Spent Nuclear Fuel at Olkiluoto - Models and Data for the Repository System 2012. POSIVA 2013-01. Posiva Oy, Olkiluoto, Eurajoki, Finland.
- Price, L. L. et al. (2021). *Repository-Scale Performance Assessment Incorporating Postclosure Criticality*, SAND2022-7932 R, Sandia National Laboratories, Albuquerque, NM.
- Price, L. L., Alsaed, A., Barela, A. C., Brady, P. V., Gelbard, F., Gross, M., ... & Gonzalez, E. (2020). *Preliminary Analysis of Postclosure DPC Criticality Consequences* (No. SAND-2020-4106). Sandia National Lab.(SNL-NM), Albuquerque, NM (United States); Oak Ridge Gaseous Diffusion Plant (K-25), Oak Ridge, TN (United States); Oak Ridge National Lab.(ORNL), Oak Ridge, TN (United States); Univ. of Michigan, Ann Arbor, MI (United States).
- Sassani, D., Birkholzer, J., Camphouse, R., Freeze, G., & Stein, E. (2021). *SFWST Disposal Research R&D 5-Year Plan-FY2021 Update* (No. SAND2021-12491R). Sandia National Lab. (SNL-NM), Albuquerque, NM (United States).
- Sevougian, S. D., P. E. Mariner, L. A. Connolly, R. J. MacKinnon, R. D. Rogers, D. C. Dobson and J. L. Prouty (2019). DOE SFWST Campaign R&D Roadmap Update, Rev. 1. Albuquerque, New Mexico, Sandia National Laboratories.
- Sparrow, B. S. (2003). Empirical equations for the thermodynamic properties of aqueous sodium chloride. *Desalination*, 159(2), 161–170.
- Voss, C. I., & Souza, W. R. (1987). Variable density flow and solute transport simulation of regional aquifers containing a narrow freshwater-saltwater transition zone. *Water Resources Research*, 23(10), 1851–1866.
- Weiss, C.J. (2017). Finite-element analysis for model parameters distributed on a hierarchy of geometric simplices. *Geophysics*, 82(4), E155-E167.
- White, M. D., Kneafsey, T. J., Seol, Y., Waite, W. F., Uchida, S., Lin, J. S., ... & Zyrianova, M. (2020). An international code comparison study on coupled thermal, hydrologic and geomechanical processes of natural gas hydrate-bearing sediments. *Marine and Petroleum Geology*, 120, 104566.
- Wu, R., Chen, X., Hammond, G., Bisht, G., Song, X., Huang, M., ... & Ferre, T. (2021). Coupling surface flow with high-performance subsurface reactive flow and transport code PFLOTTRAN. *Environmental Modelling & Software*, 137, 104959.

## 4. APPENDIX A: PNNL PFLOTRAN DEVELOPMENT SUPPORT

### 4.1 Introduction

This report details the FY22 contributions to PFLOTRAN development by PNNL code developers (i.e., Dr. Glenn Hammond) under the Spent Fuel Waste Science and Technology Campaign within the US Department of Energy Office of Nuclear Energy. It details software releases, enhancements to simulation process models, updates to software infrastructure, bug fixes, and code reviews in support of the Geologic Disposal Safety Assessment (GDSA) Framework. In addition to the contributions listed below, Dr. Hammond met weekly with Dr. Michael Nole [SNL] to strategize software design and the implementation of GDSA process models, and to discuss the acceptance of updates submitted by PFLOTRAN code developers from around the world.

This report fulfills the GDSA PFLOTRAN Development Work Package Level 5 Milestone – *PFLOTRAN Development Support - M5SF-22PN010304073*.



## 4.2 Software Releases

On January 6, 2022, PFLOTRAN Version 4.0 was released. Steps completed by Dr. Hammond in the release (and coordinated with Michael Nole) included:

- Ensuring that all code modifications for capability to be included in 4.0 had been merged to the master branch of PFLOTRAN (approval of Bitbucket pull requests).
- Ensuring that all regression and unit tests passed.
- Adding a *v4.0* tag to the PFLOTRAN Git repository stored on the open access Bitbucket site ([bitbucket.org/pflotran/pflotran](https://bitbucket.org/pflotran/pflotran)).
- Updating the online documentation ([documentation.pflotran.org](https://documentation.pflotran.org)), including the Developer, Theory, and User's Guides, to be consistent with code capability as of January 6, 2022. The landing page for the website documented major changes to Version 4.0 (e.g., changes to input file specifications, updates to PETSc, installation instructions, etc.).
- Announcing the release through the PFLOTRAN developer and user mailing lists.

### 4.3 Enhancements to GDSA Process Models

Dr. Hammond made the following contributions to GDSA process models within PFLOTRAN:

- Dr. Hammond worked closely with Rosie Leone and Peter Lichtner to refactor the implementation of the Multi-continuum Reactive Transport capability. The three met weekly to discuss (1) multi-continuum theory, (2) refactoring of material property data structures to increase flexibility, (3) bug fixes, and (4) verification against analytical solutions available in the literature. Rosie completed most of the code development and verification study.
- Dr. Hammond advised Alex Salazar regarding the implementation of the Material Transform Process Model within PFLOTRAN. This included strategizing the coupling with other process models, debugging memory errors and leaks, and code review.
- Dr. Hammond advised Alex Salazar on the implementation of the 3D Lookup Table. His contribution focused on implementation strategy only.
- Dr. Hammond (along with Professor Albert J. Valocchi) advised Heeho Park on his enhancements to PFLOTRAN multi-level solver capability to improve convergence of both the linear and nonlinear solvers for complex non-isothermal, multiphase flow problems (Park et al., 2021; Park et al., 2022). Dr. Hammond's main contributions were edits/revisions to the two peer-reviewed manuscripts submitted to the journal *Advances in Water Resources* and addressing reviewer comments. Heeho was the first author and primary contributor on this task.

## 4.4 PFLOTRAN Bug Fixes

Dr. Hammond fixed numerous bugs/issues reported by GDSA users, developers, and collaborators from around the world. The below are major issues/bugs that directly impacted GDSA users/developers:

- Fixed memory leak within the multi-continuum transport capability (reported by Amphos21 – GDSA collaborator in Barcelona, Spain).
- Fixed density dependent flow as a function of salinity. The contribution of salinity to the salt mass fraction variable was being compounded at each time step.
- Fixed incorrect scaling of sorption isotherm coefficients.
- Fixed HDF5 error messaging. Error messages are no longer printed when “attributes” already exist; the attributes are simply opened instead of being created again. Reported by Alex Salazar.
- Added error messaging when mass-based specific surface areas are employed for mineral precipitation-dissolution when the mineral has a volume fraction of zero.
- Added error messaging when two or more characteristic curves have the same name.
- Reverted the `material_auxvar_type` from a class back to a derived type to resolve an ongoing GNU compiler issue that does not support certain dynamically allocated arrays within arrays of dynamic classes.
- Added an error message when a region coupled to a flow condition within a source/sink term contains inactive cells.
- Fixed an I/O bug for the GDSA “total mass regions” calculation. I/O was being written from processes other than the I/O process and `fort.86` files were appearing.
- Added error messaging when internal cell faces are included in boundary sidesets.
- Added error messaging when output is requested for variables that are not supported by the requested process models in the simulation (e.g., `PERMEABILITY` for reactive transport).

## 4.5 Updates to PFLOTRAN Software Infrastructure

Dr. Hammond made the following enhancements to PFLOTRAN software infrastructure in support of GDSA applications:

- Dr. Hammond conducted weekly code reviews for pull requests (PR) submitted throughout the year. A PR is a formal request that a (Git) development branch be merged to the master branch of PFLOTRAN on Bitbucket. As outlined in the PFLOTRAN Configuration Management Plan, PRs are only accepted once all continuous integration (CI) tests have successfully passed, and a lead developer has reviewed the code modifications to ensure compatibility with existing code and compliance with the PFLOTRAN Fortran coding standard.
- Dr. Hammond oversaw the upgrade to PETSc 3.17 at the end of April (2022). PFLOTRAN is founded upon the PETSc library (Balay et al., 2022) that provides parallel solvers and data structures. Among several minor updates, this upgrade required a major rewrite of error checking infrastructure within the PFLOTRAN source code. The upgrade to PETSc 3.17 enables long-term support for the linear solver capability developed by Heeho Park as part of his dissertation research at the University of Illinois.
- Dr. Hammond upgraded and maintained the CI infrastructure provided by GitLab ([gitlab.com/pflotran/pflotran/-/pipelines](https://gitlab.com/pflotran/pflotran/-/pipelines)). He negotiated a Gitlab “Open Source Program” Ultimate license which allows for PFLOTRAN developers to use GitLab repository and testing capability free of charge. CI verifies the integrity of the PFLOTRAN repository by cloning the Git repository, building third-party libraries and PFLOTRAN executables, running unit and regression tests, and comparing results against a gold standard to ensure that answers have not changed. Such testing is vital for ensuring the longevity and integrity of the code.
- Dr. Hammond worked with Rosie Leone in revising the functional requirements for a draft of the PFLOTRAN Quality Assurance (QA) Requirements Document.
- Dr. Hammond refactored the PFLOTRAN solver object (`solver_type` derived type) to better accommodate the new multi-level solver capability implemented by Heeho Park.